



University
of Glasgow



CVE 3371 – Capstone Project

Final Report

Feasibility analysis framework on the implementation of a Bioretention cell in an existing
precinct

Brien Cheow Joon Siang

1901565

Civil Engineering Programme (CVE)
Engineering Cluster
Singapore Institute of Technology

AY 2021/2022

Abstract

There has been a long-standing issue of anthropogenic pollution of Singapore's surface runoff and increased flood risk as a consequence of rapid urbanization and climate change. With the frequency of high-intensity and short-duration rainfall events likely to trend upwards in the coming decades, this project will explore the feasibility of implementing bio-retention basins as part of a proposed runoff detention system named the Urbanwater Harvesting System (UWHS) to reduce environmental impacts of the retrofit development and overall cost of its treatment system. Currently, four configurations of the system varied by the treatment area of the bio-retention basin have been identified, where the configurations will be hydraulically modelled in Storm Water Management Model (SWMM) 5.1 and subsequently analysed to determine the economic feasibility of the implementation.

To accomplish this, a framework was first developed for the acquisition of eight hydrologic parameters in a data-scarce environment to facilitate the hydraulic design of the UWHS configurations. QGIS played a vital role in the acquisition of hydrologic parameters by providing various functionalities ranging from simplistic spatial computations (most parameters) to more advanced dataset processing tools such as hydrological processing algorithms and interpolation techniques, commonly used in combination to hydrologically condition a digital elevation map (DEM).

Since there exist two hydrological processing algorithms (Fill Sinks and Breach depression algorithms) and three interpolation techniques (Nearest Neighbour, Bilinear Interpolation, and Cubic Convolution) in QGIS, a study was developed to generate test data and compare different permutations of the algorithms and techniques employed for conditioning a DEM. The study concluded that the Fill Sinks Algorithm combined with Bilinear Interpolation produced the most realistic DEM results when compared to all other permutations purposed for the hydrological conditioning procedure, and as a result, was identified as the method of choice for conditioning DEMS for this project.

Subsequently, the system configurations had to be encoded into SWMM as a rainfall-runoff, hydraulic model to ensure its conformity to the stipulated guidelines in the PUB's Code of Practice (PUB, 2018).

To accomplish this, the hydrological parameters acquired were first used to estimate the sizes of the UWHS components (Bioretention Basin & Detention tanks) through design spreadsheets. In the absence of rainfall data, a study was performed to compare two methods of synthetic rainfall hyetograph generation (Alternating Block Method (ABM) and Huff's Method) for the development of a rainfall-runoff model in SWMM. It was concluded that the ABM yielded more consistent, conservative, and accurate results across varying storm durations, while Huff's Method yielded less consistent results due to its high sensitivity to design storm duration. As a result, the ABM was selected as the method of choice for this project.

Additionally, as the drain dimensions (width and height) were largely unavailable during the modelling process, a study was performed to investigate the effects of omitting the hypothetical drainage network from the SWMM model. The study found that omitting the drainage network led to results with less intrinsic uncertainty, in addition to being the more conservative and accurate approach when validated with the rational method. As a result, the modelling of drainage networks was omitted for this project.

Simulations of the SWMM model were subsequently carried out using the ABM synthetic rainfall hyetograph, and the estimated sizes of the UWHS components were validated/ adjusted to ensure compliance with the PUB's Code of Practice. Fifty-seven simulations were also conducted to investigate the sensitivity and impact of the eight hydrologic parameters on the model output results to improve understanding of the model behaviour and guide future attempts at model calibration and data collection.

The validated sizes of the UWHS components were subsequently used to compute the economic cost associated with the various configuration of the UWHS in addition to the Hydrologic and Treatment performance of the 4 different systems. To perform the economic analysis, a probabilistic cost estimating system was first developed in python with the added functionality to interact with any number of cells within a defined excel document.

At the core of the probabilistic cost estimating system, a triangular probability density function (PDF) was selected to model the distribution of historical construction costs of similar projects. A least-squares curve fitting function was developed using a combination of the Levenberg Marquardt and the Trust Region Reflective optimization algorithm to provide parameter estimations for the PDF. When tested against 44 predefined triangular distributions (100 samples) covering a comprehensive range of forms (systematically varying from an exceedingly left-skewed form to an exceedingly right-skewed form), the developed curve fitting function yielded an average absolute error of 1.32, 1.67 and 1.04 respectively for the minimum (a), mode (m), and maximum (b) parameters of the triangular PDF. Consequently, the curve fitting function was deemed to be adequate for modelling historical construction costs.

Finally, an Application Programming Interface (API) subroutine was developed with the xlwings python package to facilitate the interaction of the cost estimating system with a predefined excel spreadsheet. Together with a developed Monte Carlo simulation subroutine, the excel which houses the financial model (LCC, NPV, IRR) was used to perform the economic analysis of the system.

Table of Contents

Abstract.....	1
1.0 Introduction	8
1.1 Background.....	8
1.2 Project Description and Objectives.....	11
2.0 Literature review.....	14
2.1 Terminology and Concepts	14
2.2 Bioretention Basins.....	16
2.3 Detention Tanks.....	18
2.4 Stormwater Reuse	19
3.0 Study Area (Landscape & Hydrology)	22
3.1 General	22
3.2 Jurong East Precinct.....	25
3.3 Landscape & Hydrology Analysis (Step One).....	27
4.0 Data Acquisition for Urban Catchments.....	30
4.1 Geo-referencing.....	30
4.2 Digital Elevation Model (DEM).....	31
4.3 Catchment digitization.....	34
5.0 SWMM Modelling.....	36
5.1 SWMM.....	36
5.2 Computational Methodology in SWMM	39
5.3 Extraction of Sub-Catchment Parameters for SWMM	45
5.4 Conduit and Junction Parameters in SWMM	53
5.5 Bioretention Basin and Detention Tank Parameters.....	54
5.6 Rainfall Hyetographs and Discharge	60
5.7 Detail level/Resolution of SWMM Model	66
5.8 Validated sizes of the UWHS System & Performance	67
5.9 Sensitivity analysis of input parameters	70
6.0 Probabilistic Life Cycle Cost Assessment (LCCA) Model	82
6.1 Introduction.....	82
6.2 Probability Density Functions (PDF).....	83

6.3	Methods to Model Distribution of Cost Data.....	85
6.4	Non-Linear Least Squares Minimization Algorithms	87
6.5	Trial Methodology	89
6.6	Analysis of Results	90
7.0	Performance Evaluation	104
7.1	Environmental/ Economical Benefit	104
7.2	Life Cycle Cost Assessment	105
8.0	Conclusions & Recommendations for future work	108
8.1	Conclusion	108
8.2	Uncertainties and Recommendations for future work	110
9.0	References	113
10.0	Appendix.....	126
10.1	Elevation Profiles for Hydrologically Conditioned DEMs.....	126
10.2	Borehole Data for Site	126
10.3	Subcatchment Parameters	127
10.4	Drainage Plan for Study Area.....	128
10.5	Width Computations for Study Area.....	129
10.6	SCS Curve Numbers ¹	130
10.7	Probability Distribution of LCC, NPV, IRR	131
10.8	Hydrological and Treatment Performance of UWHS Configurations (2, 3, 5, 10 yr ARI storm events)	135

List of Tables

Table 1: Landscape & Hydrological assessment model	29
Table 2: Mean, standard deviation and spread of cell elevation within site boundaries	33
Table 3: Coefficient of Imperviousness for land use category.....	48
Table 4: Manning's n for Overland Flow (Rossman & Huber, 2016).....	51
Table 5: Runoff water quality of urban precincts and comparison with literature studies	53
Table 6: Storage Unit Parameters	59
Table 7: Orifice Parameters.....	59
Table 8: Singapore IDF Curves.....	60
Table 9: Singapore's Runoff Coefficient	65
Table 10: Selection of Storm Return Period (PUB, 2018)	65
Table 11: Time of Concentration (PUB, 2021)	65
Table 12: Validated Storage Unit Parameters	67
Table 13: Hydrological & Treatment Performance of UWHS	69
Table 14: SWMM model parameters	71
Table 15: Sensitivity of input parameters	73
Table 16: Comparison of Probability Density Functions (Back et al, 2000).....	84
Table 17: Triangular Distribution Data (Back et al, 2000).....	90
Table 18: Triangular Distribution Data based on Skewness (a,m,b)	92
Table 19: Skewness Coefficient Range	98
Table 20: Modelled Cost Distribution.....	105
Table 21: Life Cycle Cost (LCC), Net Present Value (NPV) and Internal Rate of Return (IRR) results	106

List of Figures

Figure 1: Flash Floods along Jurong (Source: Public Utilities Board, 2021).....	9
Figure 2: UWHS Configurations (Source: HDB).....	10
Figure 3: Stormwater Management Feasibility Framework	11
Figure 5: Step Two of the feasibility analysis framework in this study	12
Figure 6: Step Three of the feasibility analysis framework in this study	12
Figure 7: The four conceptualized modules in a catchment model (Adapted from Choi and Ball, 2002).....	15
Figure 7: Steps to undertake for hydrological modelling (Adapted from Choi and Ball, 2002) ...	16
Figure 9: Bioretention Basin.....	16
Figure 9: Singapore's Location and Topography	22
Figure 10: Climatograph of Changi Climate Station (data from Department of Statistics, Singapore (2022). Climate Normal (30 years average). Total Monthly Rainfall Data: 1992 – 2021, Average Monthly Temperature Data: 1992-2021, Average Monthly Humidity Data: 1992-2021)	23
Figure 11: Geological map of Singapore (Rahardjo et al. 2004)	24
Figure 12: Location and Land use of Jurong East Precinct.....	25
Figure 13: Topography and location of the study site	26
Figure 14: Monthly Precipitation, Maximum 24-hours Precipitation & Monthly Raindays (data from Meteorological Service Singapore, n.d. Historical Daily Records of Ulu Pandan rain gauge (2010.01 – 2021.12))	28
Figure 15: Averaged Precipitation Data (12-yr) of Ulu Pandan Station (data from Meteorological Service Singapore, n.d. Historical Daily Records of Ulu Pandan rain gauge (2010.01 – 2021.12))	28
Figure 16: Elevation profiles of original and processed DEMs.....	32
Figure 17: Box and whisker plot of cell elevation data within site boundaries	34
Figure 18: Digitisation of the study area, left: drainage plan; middle: google earth image; right: digitized catchment.....	34
Figure 19: Subjectivity in catchment delineation: uncertain extent of apron drain coverage.....	35
Figure 20: Struggle in defining exact boundaries	35
Figure 21: Idealized representation of a subcatchment (Rossman & Huber, 2016)	37
Figure 22: Illustration of SWMM model for the Study Area	38
Figure 23: Conceptualization of Surface Runoff in SWMM (Smith, 2022)	39
Figure 24: Illustration of irregularly shaped subcatchment (DiGiano et al., 1977)	47
Figure 25: Slopes of subcatchment for the Jurong site	48
Figure 26: Subcatchment imperviousness.....	49
Figure 27: Hydrological Soil Group of Jurong East Precinct.....	50
Figure 28: Proposed Stormwater Systems	55
Figure 29: Huff's Curves (Smith, 2022)	61

Figure 30: Comparison between the Alternating Block Method & Huff Rainfall Distribution	62
Figure 31: Synthetic Hyetograph Comparison: (a) ABM; (b) Huff's Method; (c) Cumulative Rainfall Depth	63
Figure 32: Estimated Hydrograph Comparison: (a) ABM; (b) Huff Method; (c) ABM & Huff Method Comparison	64
Figure 33: Simulated hydrographs for catchment models subjected to a 10-year design storm	67
Figure 34: Hydrological & Treatment Performance of UWHS	69
Figure 35: Local parameter sensitivity slope (Adapted: Kleidorfer, 2010).	70
Figure 36: Mean sensitivity of model parameters.....	72
Figure 37: Model Hydrographs (Width)	74
Figure 38: Change in Model Discharge Hydrographs (Width)	75
Figure 39: Model Hydrographs (Area).....	75
Figure 40: Change in Model Discharge Hydrographs (Area).....	76
Figure 41: Model Hydrographs (%Slope).....	77
Figure 42: Change in Model Discharge Hydrographs (%Slope).....	77
Figure 43: Model Hydrographs (ManningsN)	78
Figure 44: Change in Model Discharge Hydrographs (ManningsN)	79
Figure 45: Model Hydrographs (%Impervious).....	79
Figure 46: Change in Model Discharge Hydrographs (%Impervious).....	80
Figure 47: Model Hydrographs (CN).....	81
Figure 48: Change in Model Discharge Hydrographs (CN).....	81
Figure 49: Triangular Density Function (Abraham & Punniyamoorthy, 2021).....	86
Figure 50: CDF for a Triangular distribution, expressed by L(x) and R(x) unified at mode "m" ...	87
Figure 51: Convergence of Average Absolute Error between Levenberg - Marquardt and Trust Region Reflective	91
Figure 52: Overall Average Absolute Error	91
Figure 53: Average Absolute Error, Extremely Skewed (Right).....	93
Figure 54: Average Absolute Error, Moderately Skewed (Right).....	94
Figure 55: Average Absolute Error, Extremely Skewed (Left).....	94
Figure 56: Average Absolute Error, Moderately Skewed (Left)	95
Figure 57: Average Absolute Error, Symmetrical.....	96
Figure 58: Comparative Analysis of Skewness Coefficient (a, m, b)	98
Figure 59: Trends in Performance of New Computational Structure	99
Figure 60: Trends in Performance of New Computational Structure (Total Average Error)	100
Figure 61: Overall Average Absolute Error	100
Figure 62: Average absolute error of computational structure relative to sample size	102
Figure 63: Total average error of computational structure relative to sample size	102

1.0 Introduction

1.1 Background

With a total land area of 728.3 km² (Singapore Land Authority, 2020) and a population of 5.45 million (Department of Statistics, Singapore, 2021), Singapore is urbanizing at an increasing rate to meet the growing demands of the city. The rapid urbanization of the landscape in Singapore to meet these growing demands has transformed the once pervious land cover into impervious surfaces, leading to increased stormwater runoff and consequently our susceptibility to flash floods. According to Min et al. (2011), the frequency of high-intensity and short-duration rainfall events will likely trend upwards in the coming decades as a consequence of climate change. This uptrend could add further strain on Singapore's existing drainage infrastructure (Chan et al., 2012), and diminish the flood resiliency of our nation.

Previously, the focus of stormwater management was on flood prevention through works to increase the conveyance capacity of the stormwater network. However, with continued urbanization, these activities become restricted due to the diminishing usable space in our nation (Goh et al., 2017). In response to these factors, PUB adopted a multi-pronged source-pathway-receptor approach as a stormwater management strategy and tightened discharge requirements through the Code of Practice in 2014 (Public Utilities Board, n.d.).

The revised requirements enforced that "industrial, commercial, institutional, and residential developments greater than or equal to 0.2 hectares in size are required to control peak runoff discharged from the development sites. The maximum allowable peak runoff to be discharged to the public drains will be calculated based on a rational rainfall-runoff method with a coefficient of 0.55, and for design storms with a return period of 10 years and for various storm durations of up to 4 h (inclusive)" (Public Utilities Board, 2018).

All existing developments constructed before 2014 however continue to discharge stormwater above the new benchmark. [REDACTED], the effects of having older developments discharge at rates above the new regulation in the face of increasing precipitation and surface runoff conversion has contributed to the growing frequency of flash floods occurring at 4 identified sites causing disruption to traffic and potential damage to surrounding properties.



Figure 1: Flash Floods along Jurong (Source: Public Utilities Board, 2021)

Urbanization not only influences the quantity of stormwater runoff but also affects the quality of water. According to Walsh et al. (2005), urbanization exacerbates the conveyance of nutrients and pollutants and leads to a decrease in water quality while accelerating the ecological degradation of urban streams. As a result, strategies for stormwater management in Singapore have placed significant emphasis on improving the quality of water over the past decade. In 2006, PUB launched the Active, Beautiful, Clean (ABC) Waters programme (PUB, 2014), offering solutions similar to water-sensitive urban drainage systems (WSUD), Best management practices (BMPs), sponge cities, sustainable drainage systems (SuDS) and low impact developments (LID) designed to improve the aesthetics of the environment and control the stormwater runoff (Fletcher et al., 2015). These solutions synonymously view stormwater as a resource that can be treated, stored, and reused at the site of installation.

In response to the identified flood-prone areas, HDB has proposed to construct stormwater control measures such as detention tanks to combat the occurrence of flooding in existing estates. The implementation of these detention tanks addresses downstream flooding by reducing the peak discharge rate and the time to peak of the catchment hydrograph (Burns et al., 2015; Park et al., 2012). With the detention tank acting as a storage reservoir, a portion of the detained stormwater is then routed to a treatment system to produce water for non-potable reuse at the site. The combination of the entire system consisting of the detention and treatment of stormwater has been termed the Urbanwater Harvesting System (UWHS) and will be referred to as such for the remainder of this document. A representation of the UWHS with explanations is presented in *Figure 2* (a. Base Configuration).

As the UWHS has not yet been implemented, HDB is also exploring options to incorporate innovative technologies/infrastructure into the existing system to improve the cost-effectiveness of the treatment process and maximize the benefits of the retrofit. Since the overall system aims to achieve both quantity and quality control of stormwater runoff, Bioretention Basins were identified as an infrastructure with the potential to improve the cost-effectiveness of the system and provide additional environmental and social benefits.

The Bioretention Basins, classified as a type of low impact development (LID) practice for stormwater management, is a lowered area where soil and engineered media are layered to remove source pollutants in stormwater through the process of infiltration, adsorption, and absorption. The infrastructure allows the reduction of stormwater runoff and pollutant loading by providing localized hydrological controls with pollutant treatment capabilities (Coffman, 2000). A representation depicting the operation of a Bioretention Basin is presented in *Figure 2* (b. SuDS Configuration).

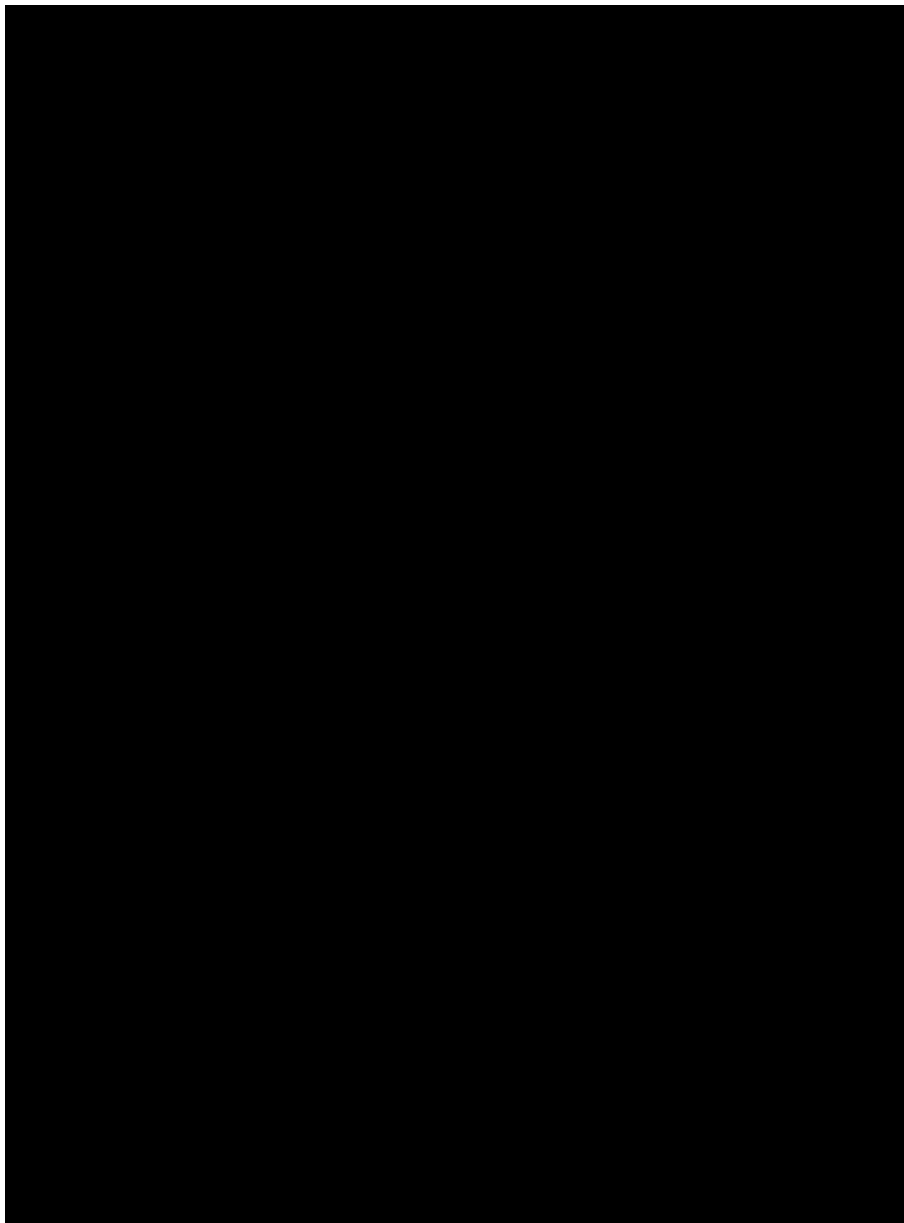


Figure 2: UWHS Configurations (Source: HDB)

1.2 Project Description and Objectives

Sustainable stormwater management must take into account hydrologic performance, environmental benefits, and economic costs. As a result, a comprehensive and operational storm water management framework is needed. However, there exists little to no studies focused on such a framework in a high-rise residential context. As a result, this capstone project will focus on the development of a four-step stormwater management feasibility framework to guide the implementation of the UWHS in existing residential precincts. The feasibility framework (*Figure 3*) will also attempt to incorporate the comprehensive evaluation methodologies of water sensitive landscape design from Romnée et al. (2015) and Wang et al. (2017).

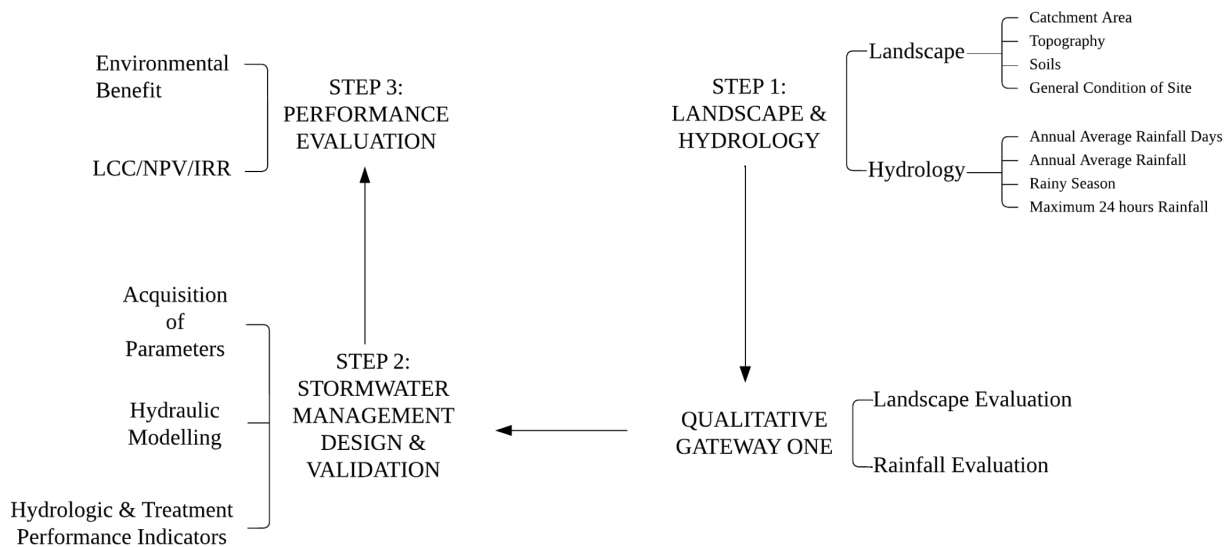


Figure 3: Stormwater Management Feasibility Framework

In the first step of the framework, an investigation of the landscape hydrology amongst other indicators surrounding the study area such as rainfall events, landscape condition, etc is performed to formulate a holistic understanding of the study area. These indicators serve as the basis for evaluating the suitability of the site in implementing the UWHS.

The second step of the framework then consists in the acquisition of site specific hydrological parameters and the design/ modelling of the UWHS. The model results from this step then serves as the basis for evaluating the hydrological and treatment performance of the UWHS.

Finally, step three utilizes the validated sizes of the UWHS infrastructure obtained in step two to evaluate the environmental benefits of the UWHS and compute the Life Cycle Cost (LCC), Net Present Value (NPV), and Internal Rate of Return (IRR) of the system.

Due to the complexity of step two and step three, separate figures were created to further detail and illustrate the sub sections contributing to the two steps in this framework.

*Figure 5 illustrates an overview of **step two** for the feasibility framework.*

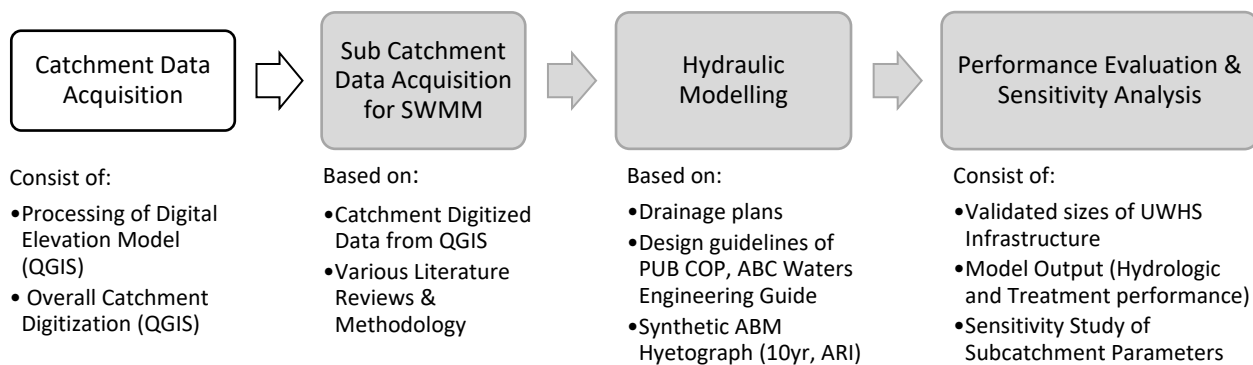


Figure 4: Step Two of the feasibility analysis framework in this study

*While Figure 6 illustrates an overview of **step three** of the feasibility framework.*

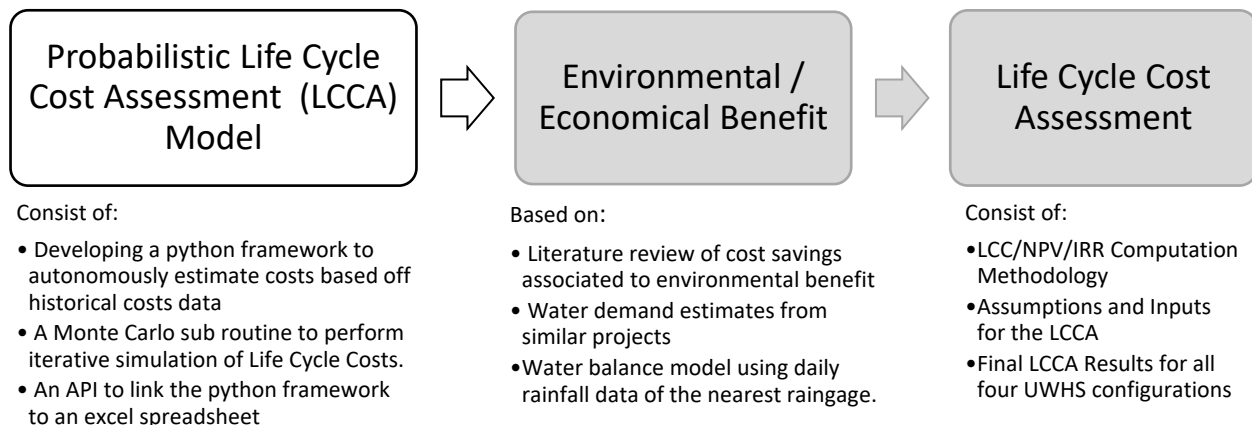


Figure 5: Step Three of the feasibility analysis framework in this study

To identify the best UWHS configuration, the framework also includes a comparative feasibility study of four different UWHS configurations, varied by the size of an upstream Bioretention Basin:

1. UWHS with Bioretention Basin (Treatment Area: 3% of Impervious Catchment Area)
2. UWHS with Bioretention Basin (Treatment Area: 4% of Impervious Catchment Area)
3. UWHS with Bioretention Basin (Treatment Area: 5% of Impervious Catchment Area)
4. UWHS only (10yrs ARI)

In summary, this project aims to:

- Produce a repeatable framework in which to conduct a feasibility study for the implementation of the UWHS configurations mentioned above. The framework will consist of 2 aspects of evaluation; namely the hydrological and treatment performance of the UWHS configurations when subjected to a 10 yr return period storm event, in addition to a probabilistic Life Cycle Cost Assessment (LCC, NPV, IRR) of the above mentioned configurations.

- Implement the framework developed for a site identified in Jurong to assess the feasibility of constructing the UWHS in its four configurations (Case Study).

In this document, Chapter 2.0 consists of a literature review for relevant topics and visits key concepts and the theoretical background of the works to be carried out. Chapter 3.0 covers Singapore's physical environment, the selected study area in Jurong (climate, physiography, and location topography) and **step one** of the feasibility analysis framework. Chapter 4.0 describes the steps taken to procure site specific data, such as the type of land use and topography for site characterization and corresponds to **step two** (Acquisition of Parameters) of the framework. Chapter 5.0 presents the SWMM software, its computational methodology, and how to acquire the necessary parameters for the construction of the model, **step two** (Acquisition of Parameters). The chapter then presents the validated infrastructure sizes for the four UWHS configurations and its associated hydrological and treatment performance, **step two** (Hydraulic Modelling & Performance indicators), before concluding with a sensitivity analysis of the SWMM hydrological input parameters to facilitate future calibration. Chapter 6.0 describes the investigation and methodology adopted to perform the Life Cycle Cost Assessment (LCCA) and Chapter 7.0 presents the Environmental/ Economical benefits of the UWHS, in addition to the LCC, NPV & IRR computational model with the final results of the feasibility analysis, **step three** (performance evaluation) of the framework. The paper concludes by identifying key issues and providing direction for future research.

2.0 Literature review

The stormwater management system being studied incorporates a bioretention basin into an existing system comprising a detention tank and a water treatment system designed for non-potable reuse. The following chapter first provides an overview of different terms and concepts that are required to successfully model an urban catchment. A literature review of the bioretention basins, detention tanks and stormwater reuse systems are then presented.

2.1 Terminology and Concepts

The term hydrology was defined by the (USGS, 2011) to be the “Science that encompasses the occurrence, distribution, movement and properties of the waters of the earth and their relationship with the environment within each phase of the hydrologic cycle”. However, the hydrological response of a catchment can be challenging to ascertain due to the heterogeneous nature of land use, land surface, vegetation, soil type, etc. combined with the temporal and spatial variability in input parameters (Cantone, 2010).

In the context of an urbanized catchment, hydrology can often be referred to as Urban Hydrology. According to Cantone (2010), the term can be defined as “a branch of hydrology that deals with the integration of hydrological and hydraulic processes at the urban scale to determine catchment response”. Hydrological processes and their time-space variability can typically be described by the local climate, land use, topography, vegetation, soils, and extent of the catchment (Singh and Woolhiser, 2002), while hydraulic processes refer to the fluid dynamics that take place in infrastructure that conveys liquids such as open channel drains, pumps, pipes etc. and which can be substantially quantified by fluid mechanics.

Cantone (2010) also reports that the land surface characteristic of urbanized catchments is highly impermeable, and generally characterized by the following land-use types (residential, industrial, and commercial districts). Additionally, the area encompassed by urban catchments is relatively small and in the order of hectares. Due to these characteristics, the modelling of urban catchments and analysis of their response is often presented in time scale resolutions ranging between minutes and hours.

The term *model* was defined by the US Environmental Protection Agency (EPA) to be a representation of natural systems through the synthetic manifestation of a similar physical system or a series of mathematical equations. In an urban catchment system, processes contributing to the catchment response are often complex and composed of several ongoing co-dependent systems. However, it is not possible or feasible to include all of these processes in a model due to the complexity of mathematically representing the entire generation and transmission process of stormwater runoff and the impractically high data requirements to

construct such a model (Choi and Ball, 2002). Due to these limitations, the original catchment system is often simplified and idealized to construct a practical model. Commonly, a catchment model consists of four contributing modules as depicted in *Figure 7*.

Firstly, the generation module involves the introduction of rainfall events and the availability of pollutant constituents in the constructed model. The subsequent collection module then focuses on the estimation of stormwater quantity and quality from the generated rainfall events collected by the catchment. This module is often considered to be the hydrological component in the model since surface runoff results are generated at this stage. The transport module of the model simulates the movement of surface runoff through the links in the drainage system and is generally considered to be the hydraulic component of the model. Lastly, the disposal module is focused on the final discharge of storm water into receiving drains or waterbodies.

The steps to undertake hydrological modelling summarized in *Figure 7* were reviewed by Choi and Ball (2002) and will constitute a large portion of the framework for modelling used in this study. Generally, the framework consists of:

- Collection and treatment of catchment specific data.
- Analysing hydrological traits of the catchment such as the topography, slope, soils, catchment imperviousness, etc. and presenting these characteristics in the form of input parameters for the model.
- Constructing and running a mathematical model using these data.
- Calibrating the model to fit field data.
- Applying the constructed model.

Because the feasibility framework is intended to be used as a top-level exploratory planning tool, it is important to acknowledge that field data such as rainfall hyetographs and discharge hydrographs is often unavailable during its application. As a result, detailed calibration of the model to reproduce field results is not in the scope of this framework and is instead replaced with a validation step using the Rational Method.

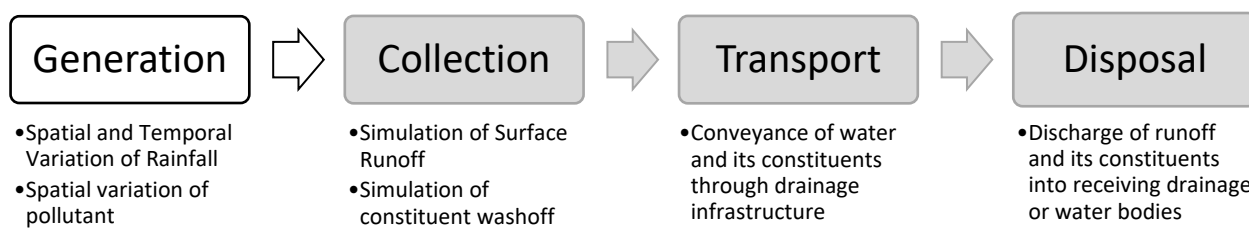


Figure 6: The four conceptualized modules in a catchment model (Adapted from Choi and Ball, 2002)

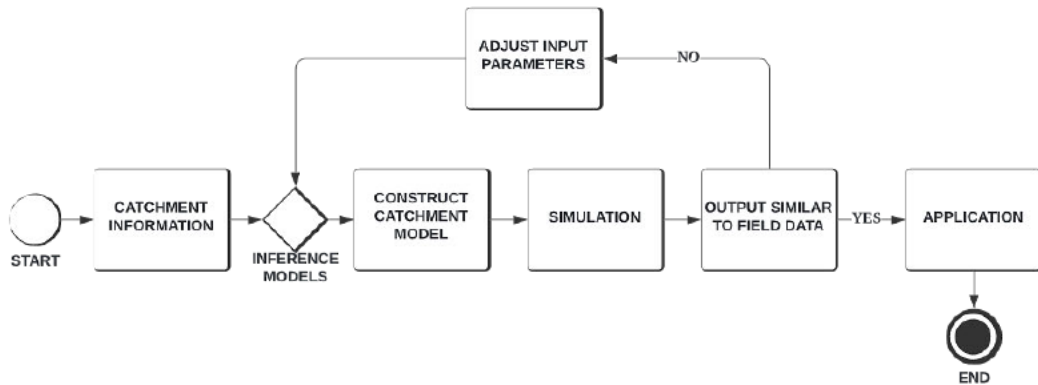


Figure 7: Steps to undertake for hydrological modelling (Adapted from Choi and Ball, 2002)

2.2 Bioretention Basins

Bioretention basins, commonly referred to as rain gardens, are defined as a vegetated ground depression, designed to collect, and treat surface flow through sedimentation, filtering, and biological absorption (PUB, 2014). Cross-sectionally, a bioretention basin comprises a ponded detention layer, surface vegetation, a filter media layer, a transition layer, a gravel storage layer, and an overflow structure to handle high flow rates during large storm events. The basin can be designed with or without an underdrain depending on the site conditions and its intended purpose (Liu et al., 2014) but is almost always paired with a pre-treatment forebay or a vegetated swale to remove coarse sediments. Generally, a basin designed with the intention to harvest surface runoff will include an impermeable geotextile sheet to prevent cross-contamination of treated water from surrounding groundwater (PUB, 2014). Figure 9 depicts a typical cross-sectional view of a bioretention basin. The filter media consist of sandy loam and/or amended soil, conducive to plant growth and microbial activity with moderate infiltration rates (PUB, 2018). The treatment surface is usually densely planted with pollution/water-tolerant vegetation to provide scour protection of the treatment surface, maintain the infiltration rate of filter media, and enhance pollutant adsorption. Collectively, the bioretention basin aims to control the catchment's peak discharge while improving the quality of surface runoff (Liu et al., 2014).

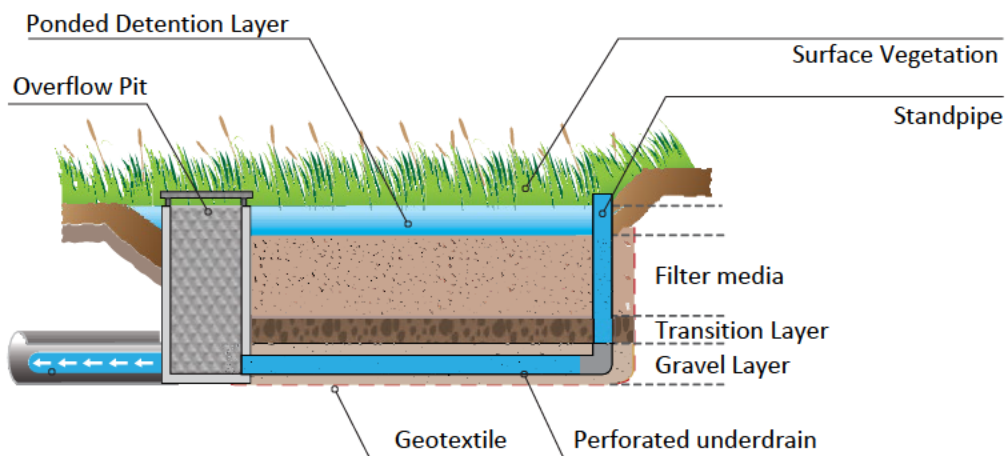


Figure 8: Bioretention Basin

2.2.1 Hydraulic performance

The Bioretention basin aims to reduce the peak discharge rate of a catchment by delaying surface runoff through detention and infiltration processes. Incoming stormwater ponds atop the treatment surface of the basin and infiltrates through the filter media before being discharged or harvested through perforated underdrain pipes (PUB, 2014). Generally, the saturated hydraulic conductivity (K_{sat}) of the filter media is used as a measure of the basin's hydraulic capacity. The parameter impacts the basin's ability to remove ponded water during and after storm events before the onset of the next storm and controls the time delay of surface runoff (Paus & Braskerud, 2014). Basins are usually constructed with a maximum ponding height of 300mm to maximize detention capabilities, but overflow may still occur during intense storm events when incoming stormwater quantity exceeds the infiltration and detention capacity of the basin.

The main challenge impacting the long-term hydraulic performance of a bioretention basin is the gradual reduction in hydraulic conductivity of the filter media due to compaction and clogging. Consequently, due to the propagation of roots, vegetation has been identified as the key to maintaining the existing soil structure and hydraulic performance of the filter media (PUB, 2018).

For this study, the Bioretention Basin is assumed to have a maximum ponding height of 300mm to maximize its detention capabilities and peak flow reduction. Hydraulic calculations for the design of the Bioretention basin will be in accordance with the national guidelines stipulated by PUB (2018) and will be validated by hydraulic modelling. Although the effects of compaction and clogging may affect the long-term performance of the Bioretention Basin, the complexity and lack of data in quantifying these effects at the time of the study resulted in the omission of these effects.

2.2.2 Treatment Performance

Bioretention Basins are complex systems (Liu et al., 2014) and the design of one is still largely empirical. Since the basins are more than just a detention system, their dimensions are also influenced by the desired capacity of pollutant retention (Davis et al., 2012). Stormwater runoff usually consists of a wide range of pollutants such as metals, nutrients and organic compounds which frequently experiences large quantity and quality variations (Le Fevre et al., 2015).

In Singapore, bioretention basins are predominantly designed to reduce three main constituent pollutants in surface runoff focusing on Total Suspended Solids (TSS), Total Nitrogen (TN) and Total Phosphorus (TP). According to PUB (2018), the pollutant reduction capabilities of the bioretention basin can be empirically determined through the relationship between the saturated hydraulic conductivity of the filter media and the percentage value of the treatment area relative to the total impervious area.

Despite the focus on the three main pollutants, bioretention basins have been shown to effectively filter many other pollutants including heavy metals such as lead, copper, and zinc (Kim et al., 2003); polychlorinated biphenyls (Gilbreath et al., 2019); and micro plastics (Gilbreath et al., 2019; Smyth et al., 2021) among others. Due to the omission of these pollutants in the national design guidelines, and the implicitly complex processes contributing to their removal, these pollutants and their resulting environmental effects are not explored in this paper.

In general, bioretention basins have been found to efficiently reduce total suspended solids (TSS) by filtering and sedimentation processes. However, due to the efficient removal of TSS through these processes, the retained solids have been found to significantly reduce hydraulic conductivity of the basin through the obstruction of finer pores (Kratky et al., 2017; Liu et al., 2014). Removal rates of nutrients such as nitrogen and phosphorus have been found to be variable with some cases experiencing good removal rates, while others low. Past studies have also shown that the removal rate of nutrients significantly depends on the filter media composition and design (Davis et al., 2009; Kratky et al., 2017). In the context of this paper, pollutant removal rates of the Bioretention Basin for total suspended solids, total nitrogen and total phosphorus will be established using supplementary empirical charts provided by PUB (2018).

2.3 Detention Tanks

Detention tanks are typically underground storage infrastructures that collect incoming stormwater runoff. The collected stormwater is subsequently released to the downstream drainage system at controlled rates to decrease the magnitude of peak flows. As a result, the widespread implementation of such infrastructures helps the national drainage system to accommodate higher intensity storms brought about by climate change (PUB, 2021). Detention tanks have also been identified by various literature for its potential and applicability for stormwater storage in reuse applications (Campisano et al., 2017; PUB, 2018).

However, peak flow control and stormwater reuse are naturally conflicting goals. While fully filled tanks are the ideal scenario when storing stormwater for reuse, it fails to provide the detention volume required during a storm event. As a result of this, detention tanks can only be used in conjunction with stormwater harvesting or reuse systems in Singapore given that the storage volume is provisioned separately from the required detention volume of the tank (PUB, 2021).

In this paper, detention tank volumes are determined using the modified rational method as stipulated by the national design guidelines published by PUB (2018). Since the harvesting volume for the site is provisioned separately from the detention volume of the tank and does not contribute to the system as a stormwater management infrastructure, no parametric change is expected for the volume parameter. As a result, an arbitrary volume of 100m^3 was selected for the harvesting volume across all 4 scenarios.

2.4 Stormwater Reuse

2.4.1 Scale and description of the implementation

Stormwater reuse is an ancient practice that has been traditionally employed to meet the needs of water supply in areas with limited water access. In the past decade, widespread urbanization and worsening climate change have continued to affect the availability of sustainable water supply across the globe (Campisano et al., 2017). As a result, great emphasis has been placed on exploring the implementation of stormwater harvesting systems in conjunction with urbanwater management strategies to lessen the consumption of potable water for non-potable applications.

Existing literature distinguishes between the terms Stormwater Harvesting (SWH) and Rainwater Harvesting (RWH) for the reuse of stormwater. SWH describes the storage of stormwater runoff from drains and waterways for reuse applications at the community or industrial level (Philp et al., 2008). RWH typically involve collecting rainwater from roofs for domestic/small scale water usage. However, these terms are frequently used interchangeably, with RWH regularly defining both practices (Akram et al., 2014).

Reuse systems that utilize tank storage often have high water savings potential, as the collected stormwater can alleviate water demand for indoor or outdoor uses that do not require potable water. Some of these uses were identified by Campisano et al. (2017) as flushing of toilets, laundry, irrigation, outdoor cleaning, and car washing. Examples of innovative systems for the use of rainwater also exist in industrial cooling towers (Thomé et al., 2019) and thermal energy recovery (Kollo & Laanearu, 2017). Despite its wide range of uses, the main aim of RWH is to reduce the depletion of centrally supplied potable water sources to non-potable uses (Campisano et al., 2017; Jones & Hunt, 2010). Depending on the region, variations in the use of collected stormwater will most likely occur. In water-scarce regions, reuse may consist of toilet flushing and laundry while more tropical regions may limit the use of collected water to irrigation and outdoor applications (DeBusk et al., 2013).

Over the recent years, multiple countries such as Australia, Japan, USA, and Brazil have gained experience implementing RWH, with Australia positioned as the leading country within the space. In Australia, RWH systems play a supplementary role to the national water supply and are encouraged through regulations such as the building code requirements for alternative water sources, water preservation measures, and monetary incentives. As a result, RWH systems now play a vital role in Australia's long-term strategies to secure water supply. Singapore has also employed RWH systems in recent years. There are projects such as the SDE4 building at the National University of Singapore (BCA, 2018) for innovative RWH solutions, the School of Art, Design and Media at National Technological University (BCA, 2011) for rainwater reuse practices and centralized stormwater harvesting/ control systems in multiple HDB developments.

Singapore in its past decades of nation-building has managed to establish a robust and diversified supply of water for the nation through the four national taps consisting of water from local catchments areas, imported water (from Malaysia), purified reclaimed water (known as NEWater) and desalinated water (Irvine et al., 2014). Consequently, this abundant access to high-quality potable water may be the reason why RWH systems have a comparatively low adoption rate relative to Australia. However, climate change may continue to exacerbate, causing higher water temperatures, greater storm events, and increased flood propensity in our surface water sources, thereby promoting increased levels of micro-organisms, nutrients, organic material, and pollutants in our water source. These effects coupled with the increasingly prolonged wet/ dry climatic variations, and the uncertainty of water imports after the expiry of the water agreement with Malaysia may influence the availability of water in Singapore. Currently, there are few incentives to reuse stormwater in Singapore. The Green Mark Certification Scheme launched by BCA encourages the use of rainwater for landscape irrigation and provides a green mark point within its certification scheme for the implementation of such systems.

2.4.2 Source water quality

The ease of reuse for collected stormwater will depend on the quantity of its constituent pollutants. In the reuse process, these pollutants may be introduced when stormwater runoff is generated and conveyed into the tank. In studies conducted by Despins et al. (2009), the water quality of runoff conveyed into the tank was found to be affected by the surface material of the catchment, the pollution characteristics of the site, seasonal variations, and weather conditions. Additionally, the microbial quality of collected stormwater was found to vary depending on the site. Excrement from mammals like birds, cats and other life forms has been found to be the leading source of pathogenic contamination. In particular, the “first flush” of collected stormwater has often been found to contain the largest concentration of pathogens. Nevertheless, this was identified to be inconsequential if the collected stormwater was purposed for non-potable uses (Campisano et al., 2017).

During the collection of stormwater, the storage tank also offers slight improvements in water quality through sedimentation and precipitation processes (Despins et al., 2009). Past studies have shown the potential for outfitting pre-collection (sumps, screens, and first flush diversions) and post collection (ultraviolet sterilization, chlorination, filtration) treatment strategies centered around the storage tank. Of these treatment strategies, first flush diversion has been identified by studies to cost-effectively improve water quality (Campisano et al., 2017; Despins et al., 2009). To conclude, the scope of the filtration/treatment strategy employed should heavily rely upon the raw water quality of the stormwater collected, in addition to the intended scope of reuse.

2.4.3 Economic Feasibility

The economic feasibility of RWH is difficult to ascertain because numerous factors play an important role in its consideration. Costs traditionally included construction, operation, and maintenance of the system. In past studies, water savings have been frequently used as the primary benefit of such systems and payback periods were calculated based on existing water prices or future projections. However, many of the other indirect benefits attained from RWH may not have been assessed monetarily due to data limitations and/or complexity in associating a quantifiable value (Amos et al., 2016). In a study conducted by Campisano et al. (2017) a large variety of RWH systems were economically evaluated with widely varying results. The study found that many of the systems were economically unviable due to long payback periods but concludes by acknowledging that the assessment model only accounted for advantages directly associated with water savings.

In another study, DeBusk et al. (2013) discuss the reuse of stormwater in humid regions. The paper suggests that stormwater reuse in humid regions with seasonal rainfall may be restricted to irrigation and outdoor applications only. As a result, a secondary objective such as stormwater management may be required for the RWH system to be economically viable. The paper also suggests a disparity in usage and intent for RWH systems in regions with seasonal rainfall. This disparity is illustrated by how large volumes of stormwater collected during rainy seasons coincide with periods of low water demand for irrigation and outdoor applications and conversely, how water demand is high during periods of limited rainfall.

To assess the economic feasibility of the system in this study, a life cycle approach for the UWHS configurations is adopted, where the capital costs incurred during construction as well as the recurring costs of the system's operation and maintenance are considered using a Net Present Value (NPV) methodology.

It should be noted that due to the lack of relevant data at the time of this study, costs estimates were either obtained from estimations from [REDACTED] or subjectively based on the author's judgement. Despite the high likelihood of inaccurate final results, the author believes that this approach is reasonable and can demonstrate the capabilities of the economic feasibility assessment framework developed for this project. By demonstrating the economic assessment framework using an example, the author hopes to promote a greater understanding of the framework and thus facilitate further customization by the user to fit future business objectives.

3.0 Study Area (Landscape & Hydrology)

A summary of Singapore's general geography is detailed in this chapter. Additionally, the location, topography, climate, soil, and land use for the identified study area are also described in this chapter. The first step of the framework (Landscape & Hydrology analysis) will then be covered at the end of this chapter.

3.1 General

3.1.1 Location

Singapore is an island state of Southeast Asia, sited at the equator with the coordinates 1.3521° N, 103.8198° E, when referenced to the global datum WGS 84. Situated near the southern tip of the Malay Peninsula, Singapore is delineated from Malaysia by the Straits of Johor to its north and separated from Indonesia by the Singapore Strait to its south.

The island state is composed of approximately 63 islands with a total land area of 728.3 km^2 (Singapore Land Authority, 2020). According to (Check, 1997), the main island of Singapore spans approximately 42km from east to west and 23km from north to south.

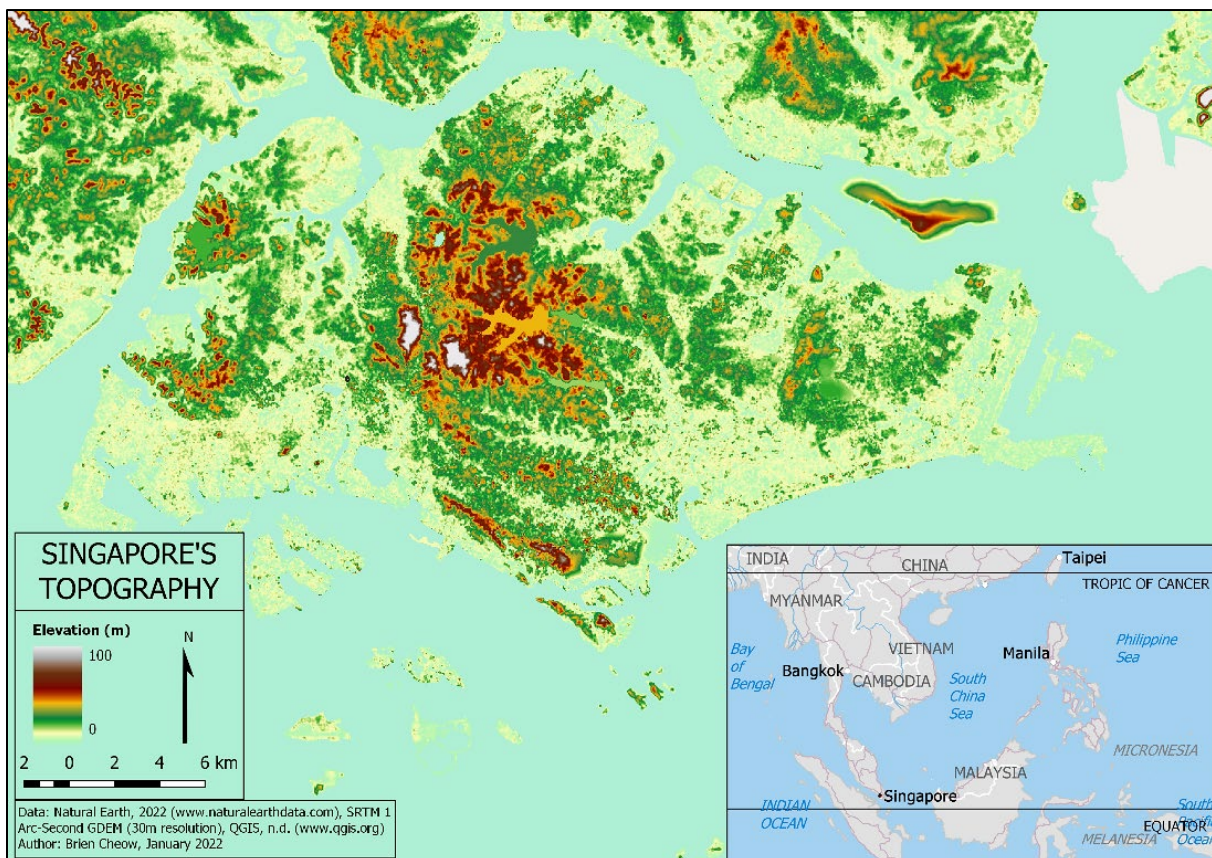


Figure 9: Singapore's Location and Topography

3.1.2 Weather

Situated near the equator, Singapore experiences a conventional tropical climate characterized by abundant rainfall, high humidity, and uniformly high temperatures throughout the year (Sien & Fook, 1991). The climatic characteristic of Singapore is shown by a climatograph of the Changi Climate Station depicted in *Figure 10*. Within Singapore, annual precipitation ranges between 1650mm to 2550mm depending on the gauge location, and on average, Singapore experiences 167 days¹ of rain annually, with many heavy rainfall events, accompanied by thunder (Meteorological Service Singapore, 2020).

[¹ A “rain day” is considered whenever the total rainfall for the day is equal to or greater than 0.2mm depth]

Two prominent monsoon seasons separated by inter monsoon periods distinguish the climate in Singapore, introducing variations to wind speed and direction (Meteorological Service Singapore, 2020). This creates wetter and dryer seasons within the year, with the north-east monsoon season lasting between December to early March and the south-west monsoon season lasting between June to September (Check, 1997). Generally, the northeast monsoon season is represented by widespread continuous moderate to heavy rain, as strong wind episodes or monsoon surges bring about major rainfall events which often persist across several days. Comparatively, the south-east monsoon season comprises occasional strong winds which bring about brief but intense rainfall (Meteorological Service Singapore, 2020). The rainfall characteristics in Singapore are thus conducive to frequent flash floods.

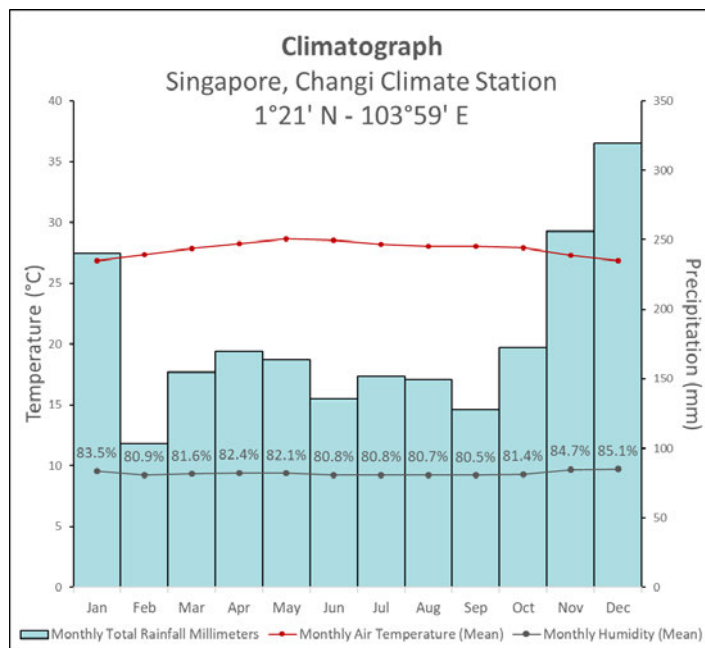


Figure 10: Climatograph of Changi Climate Station (data from Department of Statistics, Singapore (2022). Climate Normal (30 years average). Total Monthly Rainfall Data: 1992 – 2021, Average Monthly Temperature Data: 1992-2021, Average Monthly Humidity Data: 1992-2021)

3.1.3 Geology

The geology of Singapore is composed of ten geological formations of which four are regarded as major formations due to the size of their natural deposits. Due to this, Singapore's geology can be approximately represented by the; Jurong Formation (Late Triassic to Jurassic) containing sedimentary rocks with six distinct sedimentary facies; the Bukit Timah formation (Early to Middle Triassic) made up of igneous rocks consisting of granite and granodiorite; Old Alluvium (Late Tertiary to Pleistocene) consisting of dense to cemented muddy sand/gravel; and the Kallang formation (Late Pleistocene to present) characterized by soft marine clay, loose alluvial muddy sand and inshore marine deposits (Public Works Department Singapore, 1976).

As illustrated in *Figure 11*, the Jurong formation consisting of sedimentary rocks occupies the west and southwest region of Singapore, with granitic rocks of the Bukit Timah formation occupying the northern central region, Old Alluvium consisting of quaternary deposits underlying the east region and the Kallang formation consisting of sedimentary deposits dispersed throughout Singapore. Weathering plays a significant role in altering the fabric of rocks in Singapore. Generally, residual soils produced by the weathering process tend to vary between clayey sands and sandy clays (Pitts, 1984).

The accumulation of these residual soils atop the soil/rock formations then forms weathering or soil profiles of varying thickness, composition, and characteristics. In general, the average thickness of weathering profiles underlain by the Bukit Timah formation is 20m (Pitts, 1994), with the upper sections and lower sections of the profile composed of clayey silts and eroded granitic rocks respectively (Rahardjo et al., 2004). The thickness of weathering profiles atop the sedimentary Jurong formation varies significantly depending on the parent rock type, but generally consists of silty clay (Jin, 2020). The profiles of the Old Alluvium rarely exceed a depth of 7m and are mainly composed of clayey silty sand (Pitt, 1994). Lastly, the weathering profile of the Kallang formation is characterized by highly impermeable clay separated by fluvial deposits (Jin, 2020).

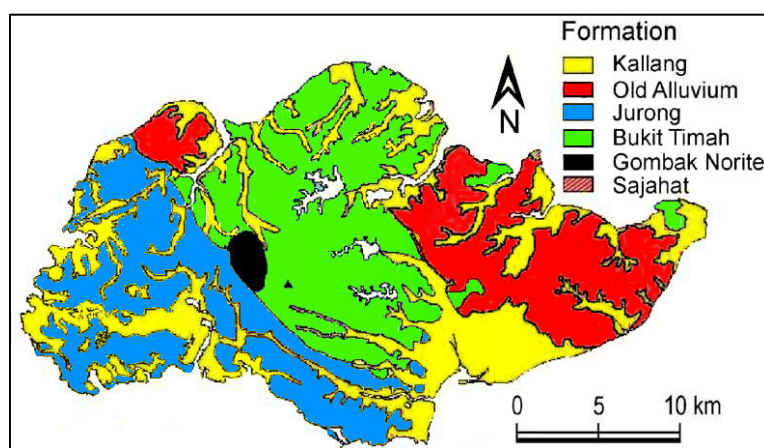


Figure 11: Geological map of Singapore (Rahardjo et al. 2004)

3.2 Jurong East Precinct

3.2.1 Location and Site

The Jurong East subcatchment¹ selected for this study is in the south-western region of Singapore (*Figure 12*) with the coordinates 1.347044°N, 103.7322°E, referenced to the WGS 84 datum. The study site occupies an area of approximately 1.978 ha² and was chosen for this study due to its suitability and potential for application. The climatic characteristics of Singapore described above persist, with the study site receiving an approximated annual precipitation of 2487.8mm and 183 rain days (Meteorological Service Singapore, 2020)³. In 2020, the wettest and driest months recorded in the area were September (341.6 mm) and February (76.4 mm) respectively.

The surrounding area of the study site is highly urbanized and consists of mainly residential buildings and impervious land cover. Within the study site, vegetated areas are dispersed throughout the catchment and consist of grass, trees and uncovered open spaces. These infiltration promoting areas constitute approximately 13% of the study site, while the remaining 87% of the study site is composed of highly impervious land (namely concrete and asphalt surfaces that disallow infiltration of stormwater). Figure 12 depicts the location of the site and its present land use.

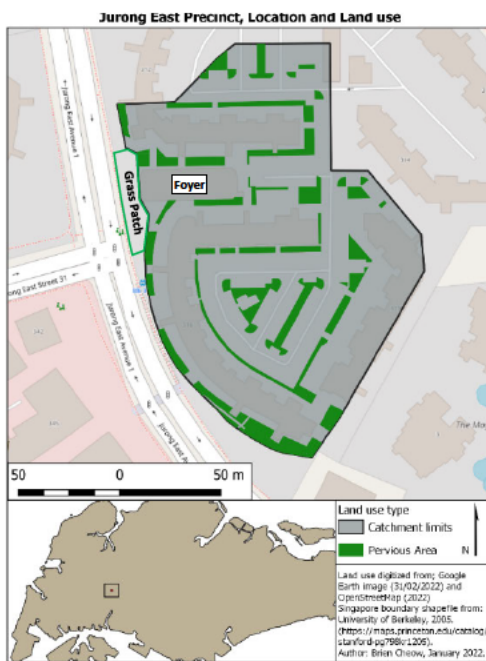


Figure 12: Location and Land use of Jurong East Precinct

¹ Although the study area is generally regarded to be subcatchment of the larger Jurong East Catchment, it is appropriate to term the area independently from the entire watershed due to the scope of study. Thus, the term "catchment" will be used in place of "subcatchment" for the remaining pages.

² Data manually extracted from QGIS 3.16 using OpenStreetMap, 2022.

³ Data extracted from Historical Daily Records of Ulu Pandan rain gauge for the year of 2020.

3.2.2 Topography

By evaluating the data from the Digital Elevation Map (DEM), the catchment's relief was found to be non-uniform (*Figure 13*).

The north, north eastern and western edges of the catchment is generally elevated relative to the rest of the site and is thus evidently characterized by steeper slopes. The remaining sections of the catchment relief remain largely uniform. The highest point of the catchment reaches an altitude of 24m according to the DEM dataset while the lowest point of the catchment was documented to be at an altitude of 16m. Approximately 73% of the area has an altitude between 16m and 20m with the remaining 27% having an altitude greater than 20m.

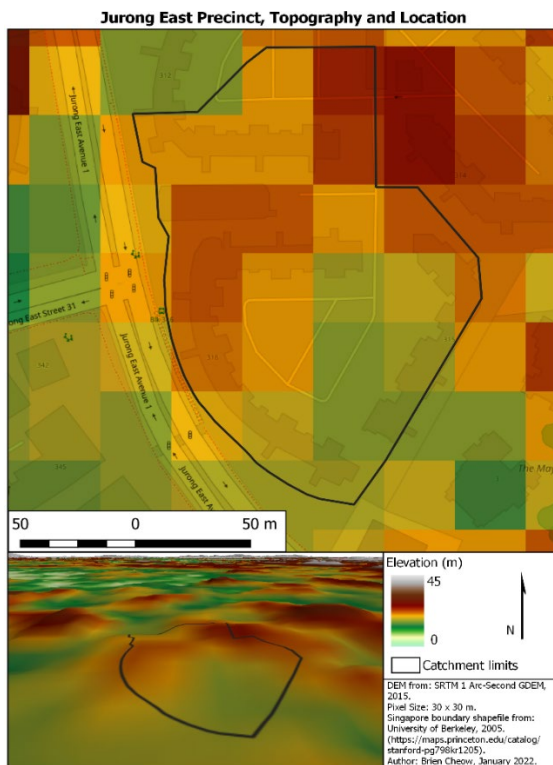


Figure 13: Topography and location of the study site

3.2.3 Soils

Soils units that develop over the Jurong Formation generally consist of silty clay but can vary rapidly depending on the location (Jin, 2020). For the study site, topsoil predominantly consists of silty clay and clayey silt with thin stratifications of fine sand (INLIS, 2022). Due to the high proportion of fines in the soil, infiltration capacity is expected to be low. Therefore, in-situ soils are generally expected to tend towards the National Resource Conservation Service (NRCS) hydrological soil group Category D, typically used to categorize soil with low permeability.

Appendix 10.2 depicts the geological information of the site through digitized borehole logs obtained from the soil report of the study area.

3.3 Landscape & Hydrology Analysis (Step One)

To conduct the first step of the framework (Landscape & Hydrology analysis), a series of indicators regarding the landscape and rainfall events are explored. Landscape indicators include the catchment area, terrain, physical substrate and geomorphology in the catchment, land use, etc, while indicators for the rainfall events mainly consist of the annual average rainfall, rainfall days, 24hrs rainfall, etc. (Wang et al, 2017). This section will attempt to summarize the previously mentioned characteristics and express them in the context of the feasibility framework.

3.3.1 Landscape indicators

As mentioned previously, the study site occupies an area of approximately 1.978 ha and has a terrain characterized by generally elevated topography in the north, north eastern and western edges of the catchment relative to the rest of the site. Underlying the catchment, insitu soils predominantly consist of low permeability soil types such as silty clays and clayey silts, classified within the hydrological soil group, Category D. High rise residential buildings and gray infrastructure (e.g, carpark areas) densely populate the site, and a large atrium/foyer for communal activities occupy the middle-left portion of the catchment. Despite the presence of an atrium for communal activities, the availability of “green” space for recreational activities was deemed to be lacking for the study area. Since there exist a large unused grass patch beside the foyer, the study area has the potential to integrate a recreationally focused sustainable stormwater infrastructure with the existing living space. In summary, the highly urbanized study site has a high rainfall to runoff conversion rate due to insitu conditions, but has the space and potential to benefit from the implementation of sustainable stormwater management infrastructure both recreationally and to control excessive stormwater runoff.

3.3.2 Rainfall indicators

Referring to the statistics of rainfall events between January 2010 to December 2021 (*Figure 14*), the study site received an estimated average annual precipitation of 2562.82 mm and 171 rain days annually. Similarly, as depicted in *Figure 15*, the overall wettest and driest months recorded in the area were November (300.01 mm) and February (107.45 mm) respectively, with the monsoon season between November and January contributes to approximately 29.16% of the annual precipitation. Precipitation data from the latest 12 years suggests that rainy seasons for the site ranges between, April - Jun and November - December, deviating from the averaged 30 years results depicted in *Figure 10*. This observed disparity may be due to the temporal and spatial unevenness of rainfall distribution within Singapore in addition to the effects of rapid climate change. As a result, the design of stormwater management systems may become increasingly challenging in the coming decades due to the unpredictable & varied nature of rainfall, along with its extremities during the wet and dry seasons. *Figure 14* (Maximum 24-hours Precipitation) portrays the unpredictable and varied nature of rainfall in Singapore by illustrating the existence of both high and low intensity storm events relative to the climatic season.

Due to these reasons, it is believed that stormwater management systems should be designed with multiple functions (detention, filtration, retention, etc.) to cater for the highly varied wet and dry seasons. In the context of the study site, a bioretention basin can be implemented for the treatment of runoff from frequent storm events with an appropriately sized by-pass/overflow system in the event of heavy rainfall. Additionally, downstream to the basin, a detention tank can be implemented to provide sufficient hydraulic capacity to withhold high flow rates resulting from a 10-yr return period storm event.

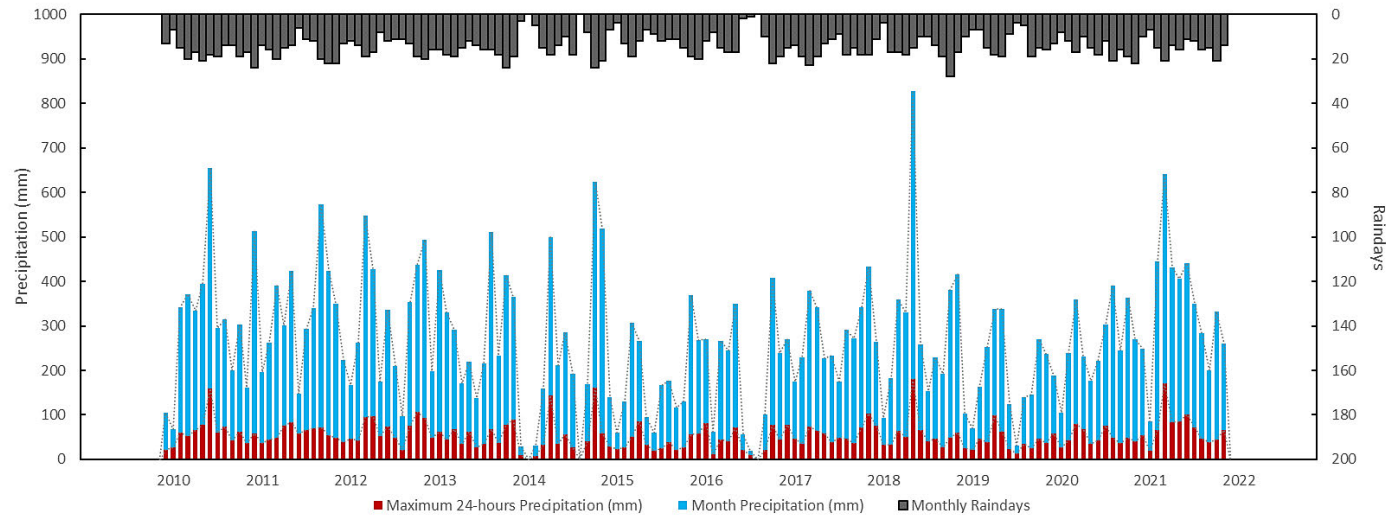


Figure 14: Monthly Precipitation, Maximum 24-hours Precipitation & Monthly Raindays (data from Meteorological Service Singapore, n.d. Historical Daily Records of Ulu Pandan rain gauge (2010.01 – 2021.12))

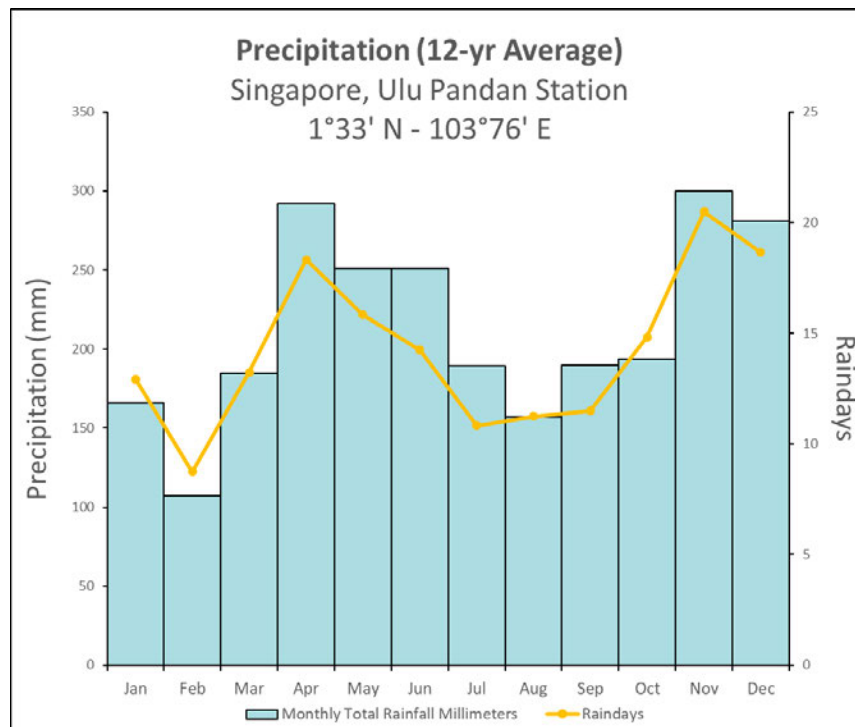


Figure 15: Averaged Precipitation Data (12-yr) of Ulu Pandan Station (data from Meteorological Service Singapore, n.d. Historical Daily Records of Ulu Pandan rain gauge (2010.01 – 2021.12))

3.3.3 Conclusion (Gateway One)

As mentioned above, the first step of the framework (Landscape & Hydrology analysis) explores a series of indicators regarding the landscape and rainfall events associated to the selected study area. To evaluate these indicators within the context of the feasibility framework, a qualitative checklist (Table 1) was developed to serve as a preliminary approval gate in ascertaining the suitability of the location and its hydrological characteristics.

Table 1: Landscape & Hydrological assessment model

Quality Attribute	Aspect of Quality Attribute	Assessment Index		
		High	Medium	Low
Landscape	• Degree of Urbanization (Lack of greenery)	x	-	-
	• Runoff Conversion Rate	x	-	-
	• Availability of Space	x	-	-
Rainfall	• Annual Average Raindays	x	-	-
	• Annual Average Rainfall (Precipitation)	x	-	-
	• Variability of Seasonal Rainfall Intensity	x	-	-

UWHS + Bioretention Basin	UWHS Only	Not Feasible
5	1	0

In Table 1, color coded cells were used to denote the suitability of the site for the implementation of the UWHS or any of its derivatives with a bioretention basin. Points are accrued based on the number of checkmarks in the respective color coded areas and is used as the basis of selecting the most appropriate UWHS configuration. If a single checkmark lands in the orange area (Not Feasible), the site is deemed to be wholly unsuitable for UWHS implementation.

Since the checklist model allocated the most number of points to the UWHS + Bioretention Basin category when applied to the study area, all four configurations of the UWHS were identified to be feasible, and must consequently be hydrologically modelled as a part of the feasibility assessment framework.

In the next chapter, step two of the feasibility framework, the acquisition of hydrological parameters is performed with QGIS to extract necessary hydrological parameters (Catchment - Topography and Area) to support the creation of the hydrological model.

4.0 Data Acquisition for Urban Catchments

The construction of any watershed model requires a substantial amount of data to correctly describe the complicated relationship between precipitation, runoff generation, and the characteristics of the catchment. For this study, data was challenging to obtain due to the lack of availability or limitations in the existing dataset. This chapter describes the second step of the framework (Acquisition of Parameters), which includes the steps taken in QGIS to procure site-specific data for the determination of necessary parameters encoded into the SWMM model. Firstly, any available site plans were geo-referenced. Next, a Digital Elevation Model (DEM) was projected over geo-referenced plans and catchment boundaries were digitized from the Google Earth satellite image. The boundaries were then validated using the site plans. As mentioned above, these steps were realized in the QGIS desktop software developed by the Open-Source Geo Spatial Foundation (OSGeo). QGIS is a geographic information system (GIS) used to study geographical information and perform work with maps. It is used to collect geographical data, analyse maps, and manage geographical information in databases (Kurt et al., 2016).

4.1 Geo-referencing

4.1.1 As-Built Drainage Plans/ Sheets

The drainage plan is fundamental to the characterization of any catchment. Unfortunately, the drainage plans of old precincts were typically hand-drawn, and only available in paper scanned copies from the Housing Development Board (HDB). Since there was no digitized version of the plan or any raster maps available, the first step was therefore to geo-reference the available plans. The drainage plan was then primarily used to define the catchment boundaries.

4.1.1.1 Singapore Transverse Mercator Projection (SVY21)

A 1:500 as-built drainage plan of the study site archived in 2005 by the HDB was used for this study. The plan was selected mainly due to its availability and recency. Within Singapore, all survey plans after 31st March 2005 were conducted in the SVY 21 datum. The Singapore Transverse Mercator Projection is based on the World Geodetic System 1984 (WGS84) ellipsoid. At the projection's centre lies a reference point known as BASE7 situated within Lower Peirce Reservoir with a latitude and longitude of 1°22'N and 103°49'E respectively. The Singapore Transverse Mercator Projection is described as a cylindrical projection of the WGS84 ellipsoid running along the central meridian. In the projection, angles and shapes are preserved to an infinitesimal scale and distances are accurate along the central meridian, however, distortion is expected if the projection extends further than 15 to 20° from the central meridian (ESRI, 2009). As a result, the use of this projection is limited to Singapore. The coordinate origin of the WGS84 ellipsoid reference frame is located at the Earth's centre of mass (Kumar, 1988). To geo-reference

the plans to the SVY21 projection, ground control points (GCPs) were added for every projection reference point portrayed in the plan. For the study, a total of 4 GCPs were used for the drainage plan. When the residual error of the transformed image is acceptable, the study area can be delineated.

4.1.2 Satellite Image

The latest satellite image of the study site from Google Earth dates back to January 26th, 2020. The image was imported into QGIS through the *XYZ Tile* protocol and automatically georeferenced using the default WGS84 Pseudo Mercator Projection. The image was then used in conjunction with drainage plans to characterize the site and to a lesser extent to validate the drainage network.

4.2 Digital Elevation Model (DEM)

4.2.1 Space Radar Topography Mission (SRTM)

The SRTM V3 1 Arc-Second Global Digital Elevation Model (GDEM) published for free in 2015 supplies a DEM raster of the world in 1-degree tiles, covering all land surfaces within the latitude zone of 50°N and 50°S with a spatial resolution of 30m (EROS, 2018). Through validation studies, the GDEM was determined to have an accuracy better than 9 m at 90% confidence (Rodrigues et al., 2006). The dataset was also identified to have positive biased error due to limitations in the remote sensing technology (5.6cm wavelength) and interference from the vegetation canopy (Farr et al., 2007). This phenomenon was particularly prominent in sites characterized by a dense canopy or in forested areas. Despite these shortcomings, the dataset is still one of the most used GDEM for hydrologic and hydraulic applications and has been proven to be a great asset for modelling studies, especially in cases where detailed topographic data is not available (Courty et al., 2019). Singapore is represented by the N001E104 and N001E103 tiles. When applied to the area of study, irregularities in elevation data were noticed (*Figure 13*). Analysis of the site's GDEM depicted elevation values ranging between 16m to 24m with approximately 73% of the site having an elevation below 20m. These values however do not accurately reflect the expected elevation of the precinct and may cause inaccuracies in characterizing the site (slope determination, etc.). Nevertheless, acknowledging that this is the best available open-access data for the site, the GDEM dataset was further processed to create a more hydrologically correct DEM for the site.

4.2.2 DEM Conditioning

DEM used for hydrological applications must be processed to eliminate sinks or spurious surface depressions. In practice, there are two distinct approaches for the removal of closed surface depressions, namely filling and breaching algorithms (Rieger, 1998). Filling algorithms consist of raising elevation levels of the cells within the sink while breaching algorithms involve dropping cell elevation levels around the sink to create a topographically viable flow path. In this study, both approaches will be explored and evaluated based on their ability to reduce the variance of cell elevation values and fill imperfections in the data set within the site. The SRTM V3 DEM tiles N001E104 and N001E103 were imported into QGIS and automatically projected onto the WGS84 coordinate reference system. The alignment of the 2 DEM tiles was visually validated before the *GDAL-Merge* tool was used to combine the 2 tiles into a single raster.

The *SAGA-Fill sinks* function in QGIS was tested on the combined raster of the dataset. The function is based on an algorithm proposed by Wang & Liu (2006) to identify and fill surface depressions in DEMs to create hydrologically sound elevation models. At the beginning of the algorithm, a priority queue model is built using the elevation of the boundary cells in the DEM raster. The cell with the lowest elevation is identified as the optimal (least) output spill elevation of the dataset and prioritized by the algorithm. The problem is then solved as the algorithm expands the optimal flow path from the cell with the lowest spill elevation to neighbouring cells in its immediate vicinity and determines their corresponding spill elevation values (Wang & Liu, 2006). A minimum slope gradient of 0.1 degrees was also preserved between cells to prevent unrealistically flat spots in the final elevation model.

The *SAGA-Breach depression* function in QGIS was also tested on the dataset. The function uses a cost-distance model specifically designed to pre-process DEMs before their usage for hydrological analysis (Conrad, 2020). In its operation, the breach function adopts a similar priority queue model as the fill function but aims to reduce cell elevations along the flow paths. The selection of viable flow paths is determined by cost-distance criteria, where the cost is determined by the extent of change made to the original DEM (Lindsay, 2012). *Figure 16* illustrates the results of the two algorithms relative to the original DEM.

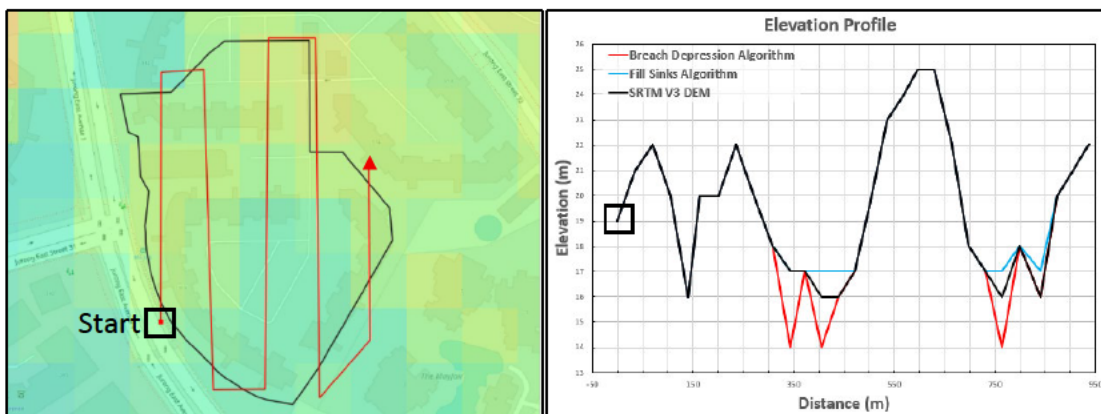


Figure 16: Elevation profiles of original and processed DEMs

4.2.2.1 Resampling processed DEMs

To comply with the development size of 0.2 ha indicated in the PUB's regulation, the higher resolution (30m x 30m) processed DEMs were resampled to 50m x 50m resolution and reprojected onto the SVY21 datum using the *GDAL-Warp (reproject)* function. Three of the most common resampling techniques; nearest neighbour interpolation, bilinear interpolation, and cubic convolution (Keys, 1981; Mitchell & Netravali, 1988; Wu & Huang, 2008) were employed to aggregate and smooth the hydrologically processed DEMs. In application, the nearest neighbour interpolation simply assigns the value of the closest neighbouring cell in the input DEM to the new output cell, while bilinear interpolation and cubic convolution methods involve taking a weighted average of four or sixteen of the nearest input cells respectively to determine the new output cell value.

The resampled raster outputs were plotted to form elevation profiles for visualization (Appendix 10.1). Through statistical analysis, the variance in cell elevation values was found to decrease with the resampling of DEM resolution across all methods (*Table 2*). This can be substantiated by the distribution of cell elevation values for each of the DEM variants as presented in *Figure 17*. Elevation values observed in bilinearly interpolated DEMs have, in general, a statistically smaller variance than those observed from the nearest neighbour resampling algorithm. Additionally, the spread in elevation values from the cubic convolution algorithm was observed to be greater than those of the bilinear interpolation algorithm. This observation can be substantiated by the differing characteristics of the re-sampling algorithms. Bilinear interpolation uses the weighted average of the four nearest input cells to determine the output cell elevation, resulting in a smoother elevation map when compared to the nearest neighbour algorithm. Cubic convolution shares the same computational characteristics as bilinear interpolation but computes the weighted average from 16 of the nearest input cells. Due to the disparity in the number of cells sampled and the number of cells within the site, cubic convolution may have excessively altered the cells within the area of interest and introduced noise originating from cells distant from the site.

As a result, the hydrological DEM produced by the fill sinks algorithm and resampled by the bilinear interpolation method was used for slope determination due to its smaller variance in elevation levels, and its realistic representation of typical site characteristics.

Table 2: Mean, standard deviation and spread of cell elevation within site boundaries

No. of Cells	Resampled DEM, 50m x 50m Resolution											
	Original			Nearest Neighbour			Bilinear Interpolation			Cubic Convolution		
	31	20	20	20	20	20	20	20	20	20	20	20
	Spread	Mean	S.D.	Spread	Mean	S.D.	Spread	Mean	S.D.	Spread	Mean	S.D.
SRTM V3 DEM	9	19.74	2.712	9	19.87	2.549	9	20	2.35	6.54	19.78	1.87
Fill Sinks	9	19.87	2.549	9	20	2.35	6.54	19.78	1.87	7.67	19.77	2.17
Breach Depression	11	19.52	3.057	11	19.8	2.68	8	19.7	2.26	10	19.6	2.54

Note: Elevation values extracted from cells within the site boundaries. Spread refers to the absolute difference between the minimum elevation and maximum elevation of the cell within the site.

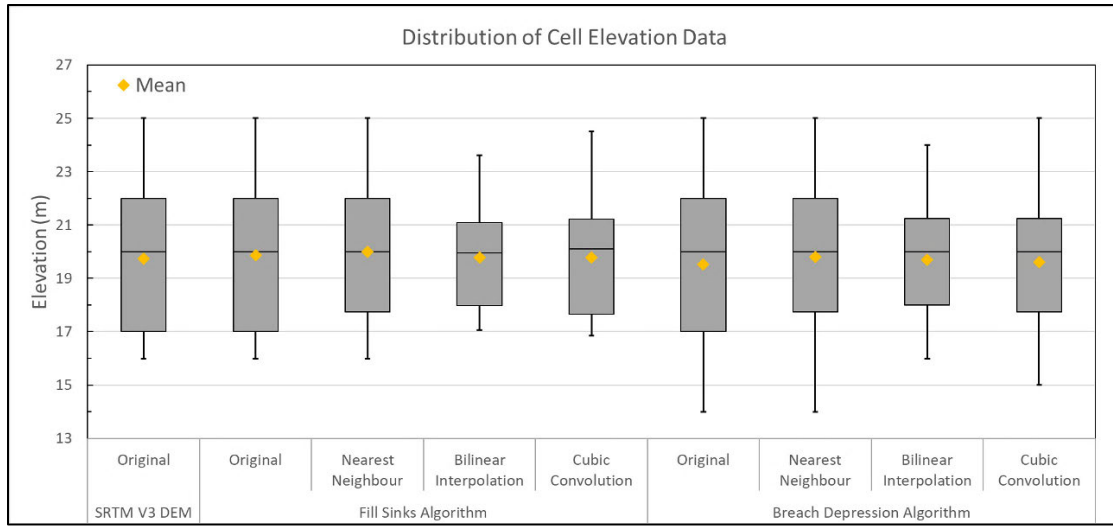


Figure 17: Box and whisker plot of cell elevation data within site boundaries

4.3 Catchment digitization

It is essential to obtain an accurate map with land use information to characterize the surface imperviousness of a catchment. At the time of the study, no detailed map for the catchment was available. Therefore, the geo-referenced drainage plans and google earth imagery were manually digitized using QGIS. The digitization steps performed in this section then produces the area parameters necessary to commence hydrological modelling of the site covered in Chapter 5.0.

4.3.1 Digitization

The percent imperviousness of a catchment is an important parameter used to construct a hydrological model. Conventionally, the urban catchment is first delineated from its surroundings using a drainage plan. Then, the catchment's impervious and pervious area is discretized based on the land cover type. Figure 12 illustrates the land cover of the study site.

Figure 18 below depicts the digitization process, through a picture of the drainage plan, a google earth satellite image and the final digitized catchment.



Figure 18: Digitisation of the study area, left: drainage plan; middle: google earth image; right: digitized catchment

4.3.2 Digitization uncertainties

The overall quality and uncertainty when digitizing a catchment is difficult to evaluate for several reasons. First of all, while the drainage plan provides information for the primary drainage infrastructure at the site, errors originating from the subjectivity in site delineation will cause uncertainty in the precision of the digitized catchment area (Figure 19). Secondly, the quality of digitization will be affected by errors that stem from the impossibility of drawing the exact boundaries of the site features (Figure 20). Lastly, the geo-referenced image on which the digitization is based can reduce the quality of the final digitization. In this study, the drainage plan and the google earth image have been georeferenced with increasing GCPs until an acceptable Root Mean Square (RMS) error is obtained. However, it is inevitable for regions delimited by digitization to be associated with uncertainty originating from the georeferenced image. To a smaller extent, the poor image resolution in images can also affect digitization quality.

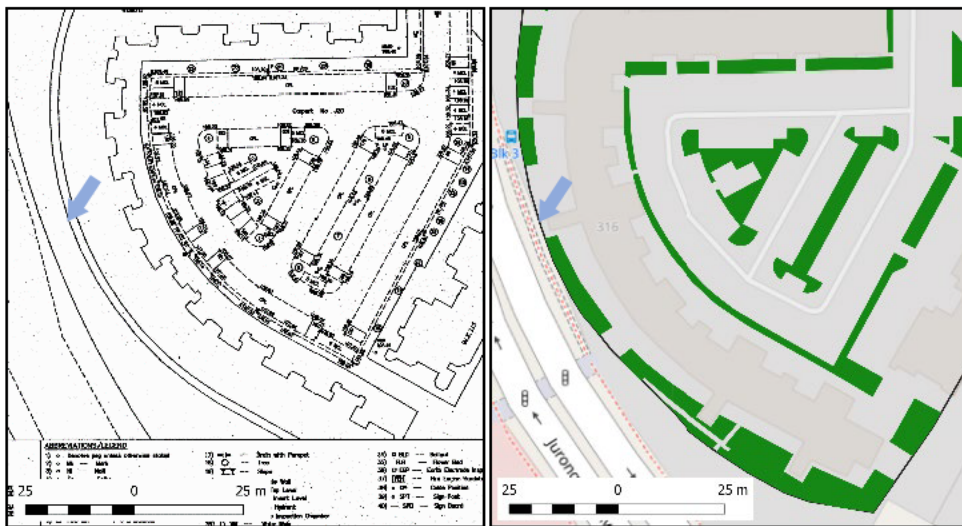


Figure 19: Subjectivity in catchment delineation: uncertain extent of apron drain coverage



Figure 20: Struggle in defining exact boundaries

5.0 SWMM Modelling

This chapter offers an overview of the SWMM hydrologic/ hydraulic model along with its computational methodology for modelling the catchment's runoff (hydrology) and channel/ drainage flow (hydraulics). Then, the methods used to extract essential input parameters for the SWMM model to operate are reviewed. Generally, these parameters help characterize the site in terms of its slope, imperviousness, surface roughness, infiltration, drainage system and more. Once these parameters are defined, the UWHS configurations identified in step one of the framework (Landscape & Hydrology Analysis) is modelled in SWMM to acquire the validated sizes of the UWHS infrastructure and its associated Hydrological & Treatment Performance for a 10 year return period storm event. The chapter concludes with a parametric study to determine the best approach to modelling a catchment with limited data in SWMM and to provide information for model calibration if site-specific hydrological data becomes available at a later date. For clarity, this chapter corresponds to step two of the feasibility framework (Acquisition of Parameters & Hydraulic modelling).

5.1 SWMM

5.1.1 Introduction

The computational concept of the EPA - SWMM program can be described as a physically based, one-dimensional rainfall-runoff simulation model that can be used for both the single event or long-term simulation of stormwater runoff quantity and quality (Rossman, 2015). SWMM was first developed in 1971 and has since undergone several upgrades in its functionality. In its current revision, SWMM 5.1 allows users to edit catchment areas, corresponding hydrological parameters, perform simulations and view a variety of results in an integrated environment through its user interface. The parameters required for the model parameterization consist of the hydro meteorologic (precipitation), geo-morphologic (terrain), hydrologic (runoff generation), hydraulic (drainage network) and pedologic (infiltration characteristics of soils) varieties. To date, SWMM continues to be one of the most widely used model around the world to plan, analyse and design urban drainage systems (Rossman, 2015).

5.1.2 Subcatchment, conduit and junctions in SWMM

Within a catchment, spatial variability of key parameters like topography, soil and overland flow length is typically expected. These parameters play a significant role in the hydrological processes governing the production of runoff in SWMM. Due to their significance, division of the catchment into a collection of smaller, homogeneous sub-catchments is usually undertaken to discretize and account for the variability in runoff production. Sub-catchments physically represent land that contains a mix of pervious and impervious surfaces, and whose runoff drains to a common drainage point (Rossman, 2015).

In SWMM, sub-catchments are conceptualized as rectangular surfaces with a width of W and a uniform slope of S that facilitates drainage to a single outlet channel (Sun et al., 2014). *Figure 21* illustrates the representation of a sub-catchment in SWMM.

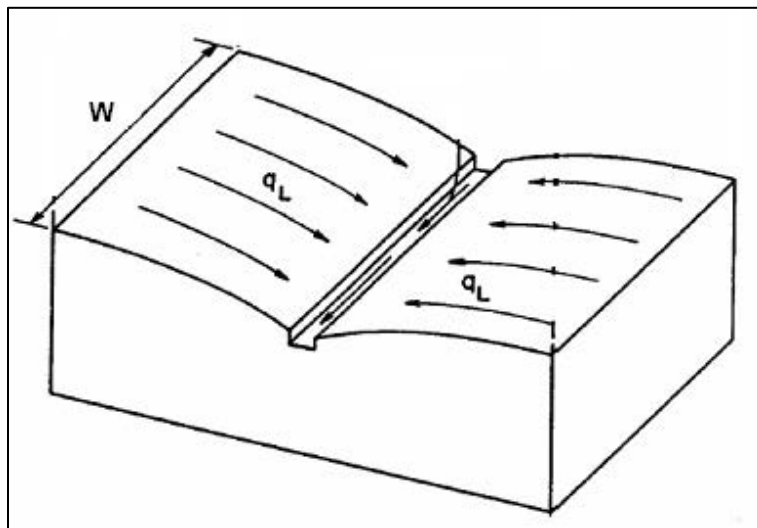


Figure 21: Idealized representation of a subcatchment (Rossman & Huber, 2016)

In general, the user is responsible for dividing the catchment into a suitable number of sub-catchments depending on the intended use of the model and the availability of site data. This process was undertaken in QGIS by defining viable outlet points (junctions) along the drainage plan for the sub-catchments and delineating them based on the site's drainage network, and the cell resolution of the DEM. SWMM's hydrological module simulates the generation of stormwater runoff quantity and quality from a compilation of the sub-catchments receiving rainfall. The hydraulic module then computes the conveyance of runoff through a conceptualized representation of the physical drainage network, allowing for the quantification of stormwater runoff and flow generation for every conduit and subcatchment in the model.

Conduits represent the channels, pipes, drains or any infrastructure meant to convey water from one junction in the model to another (Rossman & Huber, 2016). Junction nodes serve as the connection point for the conduits in the model and physically represent the confluence of pipes or channels in the drainage network. A junction node is also required when adjustments to the characteristics of a conduit are required. The outfall represents the final point of the conveyance network and is used to define the model's downstream boundary (Rossman, 2015).

In this study, the drainage plan illustrated the spatial layout of the drains but did not provide most of the drainage dimensions. As a result, standard rectangular drains were used in place of unavailable data to construct a hypothetical drainage system. The dimensions of the drain were conservatively assumed to be 0.75m (width), 1m (depth) to comply with drainage planning requirements specified in the PUB's Code of Practice (PUB, 2018) and to meet the expected discharge rate of the catchment. Once each component of the catchment has been determined, SWMM modelling can be performed (*Figure 22*).

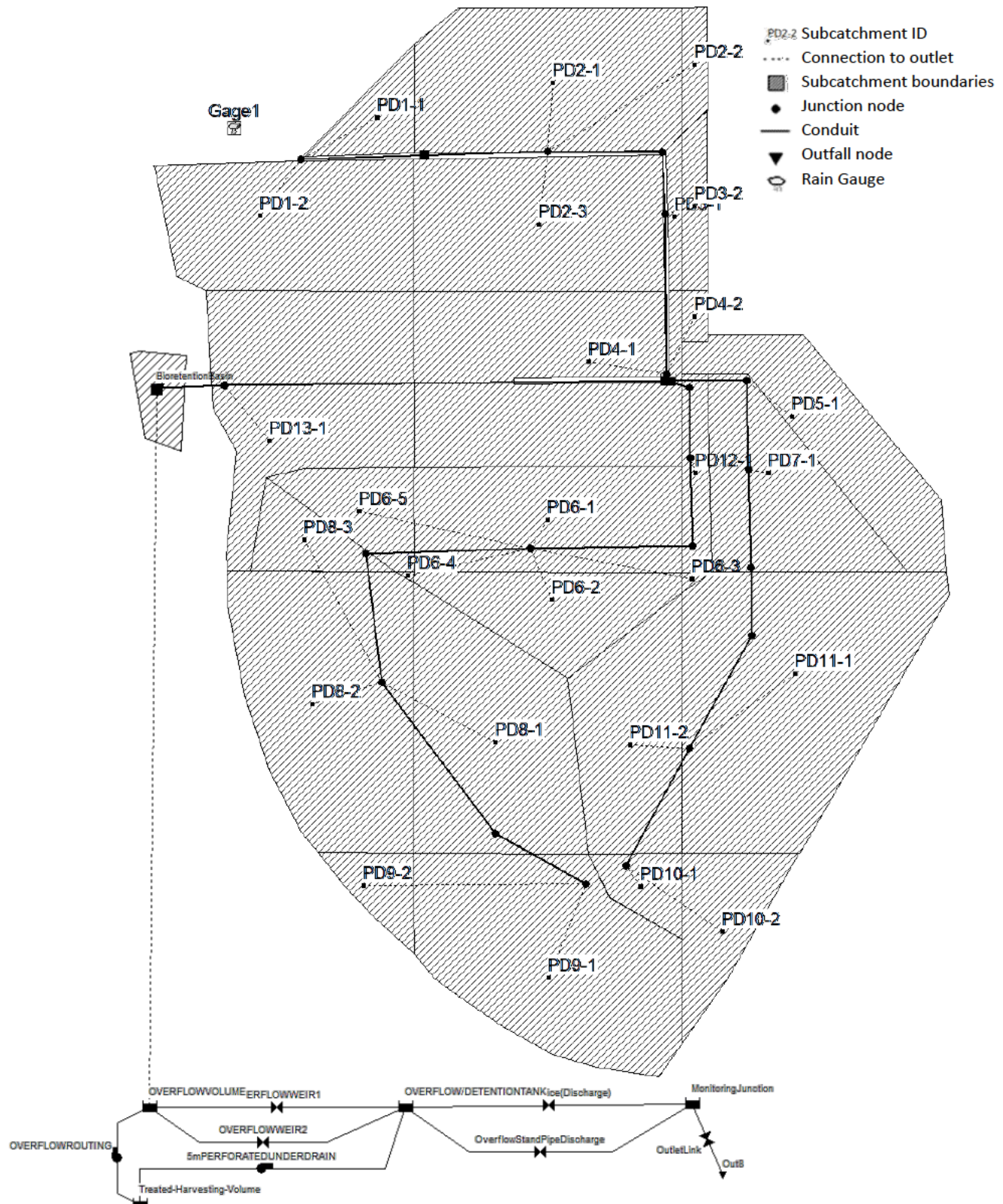


Figure 22: Illustration of SWMM model for the Study Area

5.2 Computational Methodology in SWMM

SWMM is a distributed, discrete-time simulation model based on physical processes. In the simulation model, the fundamental principles of energy, momentum and mass conservation are applied wherever suitable (Rossman, 2015). In this chapter, the methods used by SWMM to simulate surface runoff and the flow within conduits are described. Additionally, the algorithm used by SWMM to simulate the generation of pollutants is briefly described.

5.2.1 Runoff Simulation

SWMM uses a nonlinear reservoir model to estimate the quantity of surface runoff generated from precipitation falling over a subcatchment (Rossman & Huber, 2016). A conceptualized illustration for surface runoff generation in SWMM is depicted in *Figure 23*. In the model, each subcatchment surface is conceptualized as a nonlinear reservoir. A surface water budget relationship then governs the generation of runoff (Smith, 2022). In this representation, the subcatchment experiences inflows from precipitation and upstream subcatchment flows and losses from infiltration, and evaporation (Rossman & Huber, 2016). The net excess between the inflows and the losses ponds atop the surface of the subcatchment to a depth d . When the ponded water with a depth d rises above the depression storage depth d_p , surface runoff (Q) will be generated from excess between the two depths. In the SWMM rainfall-runoff algorithm, depression storage depth d_p is also subjected to evaporation and/or infiltration^a depending on the perviousness of the area in a process where the storage capacity of the reservoir is continuously replenished (Rossman, 2015).

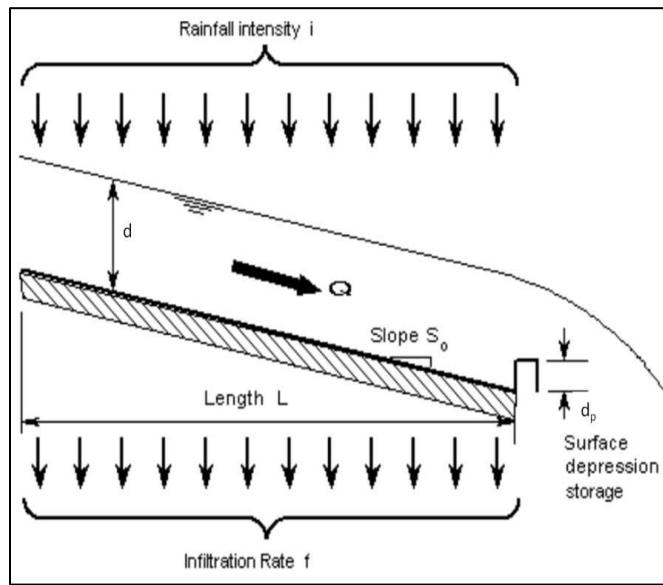


Figure 23: Conceptualization of Surface Runoff in SWMM (Smith, 2022)

^a In practice, water that has infiltrated into the ground can contribute to the total runoff of the simulation through groundwater recharge. However, the lack of data surrounding groundwater characteristics has resulted in the omission of this process in the simulation model. As a result, the volume of water that has infiltrated the ground can be considered as unrecoverable losses.

The simulation of surface runoff for each of the subcatchment is based on two governing equations. The first governing equation utilizes conservation of mass, where net changes in depth d per unit of time t is computed by the difference in subcatchment inflow and outflow rates (Rossman & Huber, 2016):

$$\frac{\partial d}{\partial t} = i - e - f - q \quad (1)$$

In the equation, $\frac{\partial d}{\partial t}$ is the net change in subcatchment water depth with respect to time, with i the precipitation intensity of the rainfall event, e the surface evaporation rate, f the infiltration rate of the surface and q the surface runoff flowrate of the subcatchment.

To model surface runoff, SWMM idealizes the flow across the subcatchment surface and represents it as if it were to mimic uniform flow within a rectangular channel. Due to this simplification, the second governing equation utilizes the following Manning's equation to express the volumetric flowrate of surface runoff:

$$Q = \frac{1}{n} \cdot A_r R_h^{2/3} S_0^{1/2} \quad (2)$$

In Equation 2, the surface roughness coefficient is represented by n , with S_0 representing the modal or average slope of the subcatchment, A_r the cross-sectional area of surface flow across the subcatchment width, and R_h the associated hydraulic radius for the surface runoff. The hydraulic radius can be defined as the fraction of the surface flow cross-sectional area and its wetted perimeter. Referring to *Figure 21* and *Figure 23*, the disparity in dimensions between the flow depth ($d - d_p$) and the subcatchment flow width W is evident. Because the flow depth will always be significantly smaller than W , the hydraulic radius will converge towards the flow depth and can thus be simplified as $R_h = (d - d_p)$. Additionally, A_r is expressed as a rectangle with the width W and a height of $(d - d_p)$. Substituting the new expressions into Equation 2 then gives :

$$Q = \frac{1}{n} \cdot W \cdot S_0^{1/2} \cdot (d - d_p)^{5/3} \quad (3)$$

Equation 3 is then divided by the surface area of the subcatchment to obtain the surface runoff flowrate relative to a unit surface area and gives:

$$q = \frac{W \cdot S_0^{1/2}}{n \cdot A_c} \cdot (d - d_p)^{5/3} \quad (4)$$

Finally, Equation 4 is substituted into the original mass balance equation:

$$\frac{\partial d}{\partial t} = i - e - f - \frac{W \cdot S_0^{1/2}}{n \cdot A_c} \cdot (d - d_p)^{5/3} \quad (5)$$

Equation 5 is a nonlinear differential equation that serves as the algorithmic backbone of the rainfall-runoff simulation in SWMM. During the simulation, for known values of i , e , f , d_p , W , S_0 ,

n , and A_c , the mass balance equation is solved numerically over each time step using the Newton-Raphson method to obtain the ponded depth d . When d is known, runoff flowrate q can be determined using Equation 4. In the event where d is lesser than d_p and the expected runoff flow rate is zero, the mass balance equation is simply modified to:

$$\frac{\partial d}{\partial t} = i - e - f \quad (6)$$

5.2.2 Flow Simulation

The simulation of flow is based on the use of known or synthetic hydrographs at the upstream points of the system to ascertain the magnitude and time of the flow at any position within the drainage system (Cantone, 2010). In SWMM, flow simulation within the conduits is governed by the conservation of mass and momentum equations for gradually varied, unsteady flow through the one-dimensional Saint Venant equations (Rossman, 2017). Depending on the desired sophistication of the constructed model, the user can choose between the Kinematic Wave or Dynamic Wave routing routine to solve the equations.

One Dimensional Saint Venant Equations

For the computation of flow in a single conduit, the system of Saint Venant partial differential equations representing one-dimensional open channel flow can be expressed as:

$$\frac{\partial A}{\partial t} + \frac{\partial Q}{\partial x} = 0 \quad (\text{Continuity}) \quad (7)$$

$$\frac{1}{A} \cdot \frac{\partial Q}{\partial t} + \frac{1}{A} \cdot \frac{\partial(Q^2/A)}{\partial x} + g \frac{\partial H}{\partial x} + g(S_o - S_f) = 0 \quad (\text{Momentum}) \quad (8)$$

Where t is the time, x is the distance along the conduit, A is the average cross-sectional area of the flow, Q is the flow rate, g is the acceleration of gravity, S_o is the bed slope, S_f is the friction slope and H is the hydraulic head of water in the conduit (Rossman & Supply, 2006). The Manning's equation was then utilized to relate the flow rate to the bed slope, friction slope and flow depth parameters so that the equation can be solved (Rossman, 2017).

According to Mujumdar (2001), it is not possible to analytically solve the full one-dimensional Saint Venant equations due to the limitations in the available methods of calculus, however, numerical means are possible with high-speed computers. Depending on the desired accuracy of the final results, the routing routine can either be generated with the full momentum equation (Equation 8) or by removing some of the terms (Mujumdar, 2001).

It should also be noted that the Saint Venant equations are only valid if the channel flow being represented meets the following conditions (Butler and Davies, 2004): hydrostatic pressure distribution in the control volume; small bed slope; velocity distribution at the channel's cross-section is uniform; prismatic channel; frictional losses for steady flow remain valid in unsteady flow; and when the lateral flow is negligible.

Kinematic Wave Routing Routine

For the Kinematic Wave routing routine, the momentum equation is simplified through the removal of the convective acceleration, local acceleration, and pressure terms (Cantone, 2011). As a result, Rossman (2017) reports that the equation can be represented by:

$$S_o = S_f \quad (9)$$

Due to its simplification, the Kinematic Wave routing routine cannot be used to model backwater effects, pressurized flows, reverse flows, entrance/exit losses and flow acceleration (Mujumdar, 2001; Rossman, 2017). Nevertheless, the routing routine performs sufficiently well for steep slope channels subject to inflow hydrographs that produce shallow flows of high velocity (Ponce et al., 1978). In SWMM, this routine is the most basic approximation of the Saint Venant's equation and is consequently able to maintain numerical stability even when time steps in the order of 1 to 5 mins are used for the simulation (Rossman, 2015)

Dynamic Wave Routing Routine

When the Dynamic Wave Routing Routine is selected for the simulation, the complete one-dimensional Saint Venant flow equation is solved, thereby producing the most theoretically accurate results for the conveyance network being simulated (Rossman, 2015). This routine can be used to model backwater effects, pressurized flows, reverse flows, entrance/exit losses and channel storage (Rossman, 2017), however smaller time steps must be used to maintain numerical stability.

5.2.3 Infiltration Simulation

Infiltration refers to rainfall losses that penetrate the surface of the ground and absorbs into the unsaturated soil of the pervious area in a subcatchment (Rossman & Huber, 2016). In SWMM, it often accounts for the largest portion of rainfall losses observed during the runoff simulation presented by Equation 1 (Rossman & Huber, 2016). Several factors influence the infiltration capacity of the soil, including geotechnical characteristics of the soil (hydraulic conductivity & porosity), soil surface, vegetative cover, and the soils moisture content. Theoretically, infiltration is governed by the Richards equation but due to its complexity, engineers have developed simpler infiltration models to capture the general dependency of infiltration capacity on soil characteristics (Rossman & Huber, 2016). Since there is no universal agreement on the best methods to use, SWMM offers four of the most widely used methods for modelling infiltration, among which the National Resource Conservation Service (NRCS) Curve Number method was adopted for this study.

NRCS Curve Number Method

First developed in 1954, the Curve Number method established by the NRCS has been widely used in computer models as well as most hydrology handbooks and textbooks (Rossman & Huber, 2016). The method uses an empirically determined parameter, the Curve Number (CN) to

compute the maximum moisture storage capacity of the soil. CN values are derived from the empirical relationship between the soil and surface cover characteristics of a catchment and the total surface runoff from a rainfall event. Soils are classified into Hydrological Soil Groups (HSG), A, B, C, and D, based on their unsaturated and saturated hydraulic conductivity. Soils with good drainage properties such as sandy soils are classified under HSG “A” while soils with poor permeability like clayey soils are classified under HSG “D”.

Traditionally, the curve number method is a total loss method that accounts for losses from interception, surface depression storage, and infiltration (Cronshay, 1986). However, since abstraction losses from interception and depression storage are modelled separately in SWMM, the CN method was modified and only accounts for infiltration losses in the model (Rossman & Huber, 2016).

In SWMM, the modified Curve Number method relates the total surface runoff Q to the total precipitation from a rainfall event P (NRCS, 2004; Rossman & Huber, 2016) using the following equation:

$$Q = \frac{P^2}{P + S_{max}} \quad (10)$$

In equation 10, S_{max} refers to the maximum moisture storage potential of the soil and can be conceptualized as the absolute change in water volume when the soil in its initial moisture condition becomes fully saturated. Its value can be determined through an accompanying CN value of the site based on the hydrologic characteristics of the soil and antecedent moisture condition (NRCS, 2004):

$$S_{max} = \frac{1000}{CN} - 10 \quad (11)$$

As depicted in Equation 11, CN values are inversely related to the maximum moisture storage capacity of the soil and thus an increase in CN values will result in reduced infiltration losses and greater runoff. The CN values for a variety of soil types and land covers have been tabulated by the National Resource Conservation Service (NRCS) and are available in the attached appendix (Appendix. 10.6).

As mentioned previously, the original Curve Number method accounts for all abstraction losses and can be derived from Equation 10 by replacing the P term with $P - I_a$, with I_a representing the initial abstraction or losses associated with the interception process, depression storage and initial soil saturation. However, since these events are already accounted for through the depression storage parameter d_p in SWMM, the complete CN method equation is not utilized. Next, through the assumption that infiltration equates to the additional losses in precipitation once runoff generation begins, Equation 10 can be manipulated to predict the total infiltration F (Rossman & Huber, 2016):

$$F = P - \frac{P^2}{P + S_{max}} \quad (12)$$

Being a continuous simulation model, SWMM can compute the temporal trend in infiltration rates if Equation 12 is applied incrementally at each timestep. As a result, the precipitation P and infiltration F terms in Equation 12 were re-expressed with P_1 , F_1 and P_2 , F_2 to store computed values at the start and end of the timestep. At the end of each timestep (Rossman & Huber, 2016):

$$P_2 = P_1 + i\Delta t \quad (13)$$

and

$$F_2 = P_2 - \frac{P_2^2}{P_2 + S_{max}} \quad (14)$$

Where i is the rate of precipitation rate during the timestep. The temporal trend of infiltration f can then be calculated using:

$$f = (F_2 - F_1)/\Delta t \quad (15)$$

After which the precipitation terms and infiltration terms are updated in preparation for the next time step.

5.2.4 Pollutant Simulation

The simulation of urban runoff quality is a very imprecise science since there exist large uncertainties in the representation of physical, chemical, and biological processes, as well as in the acquisition of data and parameters for modelling algorithms (Rossman & Huber, 2016). In SWMM, the pollutants generated from runoff of impervious surfaces are predominantly modelled using the concepts of build-up and wash off proposed by Sartor & Boyd (1972).

The true mechanisms of pollutant accumulation are extremely complex and are a result of several unpredictable factors such as wind, traffic, land use, erosion, atmospheric fallout, and cleaning effectiveness alongside many other imponderables. Due to this reason, it is unrealistic to assume that the efforts made to include such factors in physically based equations will provide enough accuracy to represent the process of build-up with any certainty. This is especially the case when applying these equations to a different country or location in which the study was based.

Equally unrealistic is to assume that empirically derived wash off equations can truly represent the localized, complex hydrodynamic, chemical, and biological processes that occur as overland flow moves erratically on the land surface introducing greater uncertainty to the simulation (Rossman & Huber, 2016).

Much of the complexities mentioned above, alongside other difficulties in simulating pollution of urban runoff, have been reviewed by Huber (1986). Nevertheless, these uncertainties can be addressed in one of two ways.

Assuming that calibration and verification data of sufficient quality and quantity is collected for the specific site, the simulation equations encoded in the SWMM model can typically be

manipulated to reproduce the data obtained from instrumentation. This approach, however, would require extensive efforts in parameter estimation and model calibration to produce water quality predictions that may vary greatly from an unknown reality (Rossman & Huber, 2016). The second option is to completely abandon the concept of detailed quality simulation and instead apply a constant concentration of pollutants (event mean concentration or EMC) to the simulated water quantity (runoff from encoded storm event). In view of the innate uncertainties involved in the process and the inability to make reasonable estimates of pollutant loads in advance of calibration, the second approach was adopted for this study.

In approach two, the EMC wash off process during wet weather is calculated directly from the total runoff rate simulated from the land use being analysed as shown in Equation 16:

$$w = K_w q f_{Lu} A \quad (16)$$

Where w is the sediment loading rate, K_w is the EMC concentration expressed in flowrate, q the normalized runoff rate over total subcatchment surface, f_{Lu} the fraction of total subcatchment area devoted to the land use being analysed and A the total subcatchment area.

Although the build-up simulation may be used to limit the maximum mass of pollutants entrained into the surface runoff, the lack of calibration and local site data may result in the premature stoppage of the pollutant load generated from the EMC wash off process. Since the EMC wash off process is only used to compare relative effects of changes with no certainty in parameter magnitude, the build-up process was omitted from the model for more conservative results.

5.3 Extraction of Sub-Catchment Parameters for SWMM

For a SWMM model to be operational, input parameters that are critical for the computation methods briefly described in Chapter 5.2 must first be acquired. As a result, this chapter can be seen as a continuation to Chapter 4.0 where parameters necessary for the SWMM model to operate is acquired. To model sub-catchments, the slope, area, width, percentage of imperviousness, infiltration, Manning's coefficient, and depression storage for permeable and impermeable areas are all essential parameters that must be obtained. Depending on the availability of data, the aforementioned parameters were acquired through various means consisting of literature review, calculation, or manual extraction from QGIS. Subsequently, input parameters were independently varied by $\pm 20\%$ to assess their sensitivity relative to model results. A compilation of the extracted parameters for the study area has also been attached in Appendix 10.3.

5.3.1 Sub-Catchment Area

For the determination of the subcatchment area, the delineated site illustrated in Figure 12 was further discretized according to the resolution of the resampled fill sinks DEM (50m x 50m) and

the drainage network illustrated in the geo-referenced drainage plan (Appendix 10.4). A total of 27 sub-catchments were digitized with a cumulative surface area of 1.978 ha.

5.3.2 Sub-Catchment Width

In theory, the subcatchment width parameter is meant to represent the width of overland surface flow from the subcatchment into the drainage network (Pitts et al., 1999). As illustrated in Figure 21, if the overland surface flow is visualized to flow uniformly over a symmetrical two-sided rectangular subcatchment into a drainage channel situated in the middle, the width of the overland surface flow will be two times the physical width of the subcatchment. However, if the area of the subcatchment remains the same but the subcatchment width is artificially reduced, a bottlenecking effect will be observed, where the conveyance of overland surface flow to the drainage network is reduced in quantity. This leads to generated runoff being retained for longer periods in sub-catchments and causes a delayed occurrence of model peak flow. Hence, this parameter is often deemed to reflect the time of concentration, which represents the time taken for a single drop of precipitation to travel from the catchment's hydraulically furthest point to its outlet (Straub et al., 2000).

Since the shape of a real sub-catchment is seldom rectangular and without properties of symmetry or uniformity, the determination of the subcatchment width can be challenging (Rossman & Huber, 2016). There exist several methodologies to determine this parameter for real sub-catchments, but computed results tend to vary significantly. As a result, the width has been reported to be an arbitrary parameter with no physical meaning (Cantone, 2010), and is often used as a calibration parameter for matching model derived hydrographs to observed hydrographs (Gironás et al., 2009; Rossman, 2015). Nevertheless, the width parameter is necessary for the operation of the model, and two of the most used methods for its computation are described below.

In the first method reported by Gironás et al. (2009) and Rossman (2015), a good estimate of the subcatchment width can be computed by dividing the area of the subcatchment by the average maximum overland flow path length. This maximum length, however, must terminate at the distance when channelized flow prevails, or at the point where generated runoff consolidates into a rivulet flow with significantly faster travel times (Rossman & Huber, 2016). Although there is no generally agreed distance for the termination of the overland flow path, the NRCS (2010) recommends that the length be limited to 100 ft or 30.5m. In this study, the longest overland flow path and its corresponding area were determined using a native measurement tool in QGIS.

Another common estimation for the subcatchment width is typically to equate the width parameter to twice the physical length of the main drainage channel serving the subcatchment. However, this approach is only appropriate when the drainage channel is centred within the subcatchment with approximately symmetrical areas on both its sides as shown in *Figure 21*. Since most real sub-catchments are irregularly shaped with an off-centred drainage channel

(Figure 24), the skew factor method proposed by DiGiano et al. (1977) was also adopted to estimate the catchment width.

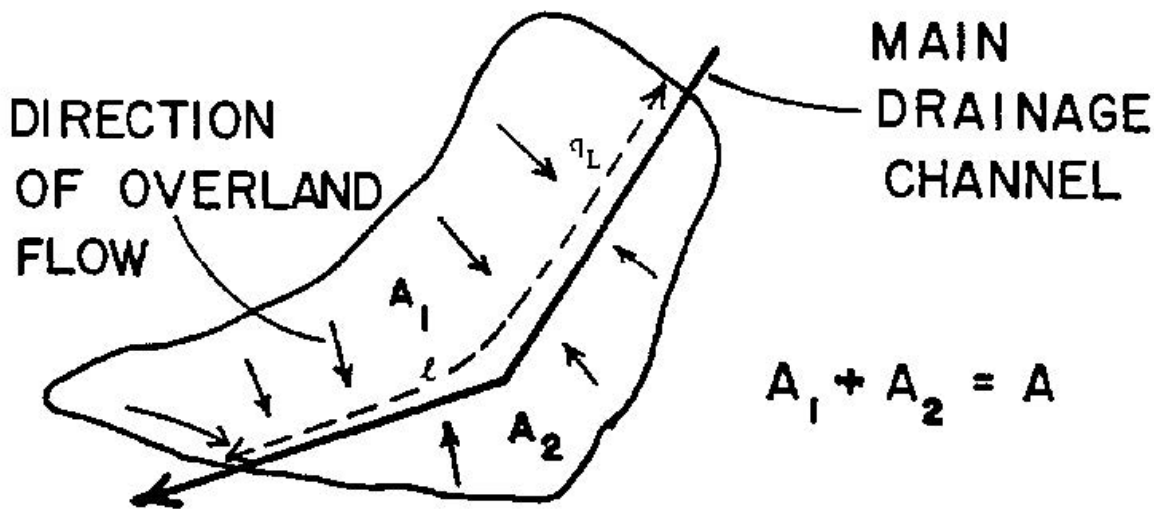


Figure 24: Illustration of irregularly shaped subcatchment (DiGiano et al., 1977)

The skew factor can be computed through:

$$z = A_L/A \quad (17)$$

Where z is the skew factor limited to a range between 0.5 – 1, A_L is the larger area connected to the drainage channel and A is the total area of the subcatchment.

Next, the width w was estimated by computing the weighted sum between the upper and lower limits L and $2L$ respectively, where L is the physical length of the drainage channel serving the subcatchment:

$$w = L + 2L(1 - z) \quad (18)$$

For this study, the adoption of either of these methods were dependent on its applicability in relation to the delineated subcatchment and the position of the nearest drainage channel. Appendix 10.5 depicts the computed width values for the catchment model.

5.3.3 Sub-Catchment Slope

The subcatchment slope in SWMM reflects the physical slope of the land surface on which the overland runoff flow occurs (Gironás et al., 2009). For the study area, subcatchment slopes were computed from the resampled fill sinks DEM with the same resolution of 50m x 50m using the *GDAL-Slope* function in QGIS. A total of 12 cells were used for the entire study area with slope values ranging from 0% to 7.44%. Figure 25 illustrates the slope parameters of the site.

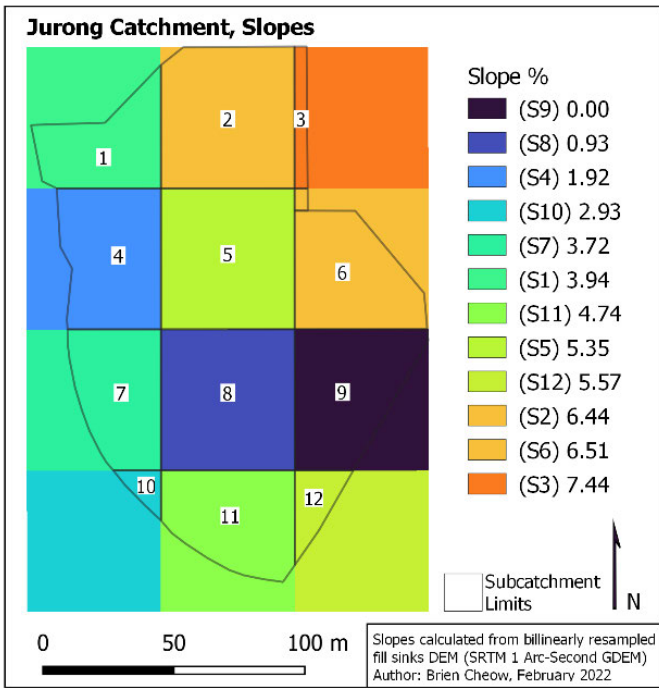


Figure 25: Slopes of subcatchment for the Jurong site

5.3.4 Sub-Catchment Imperviousness

The catchment imperviousness parameter distinguishes the percentage of land area that is impermeable and prohibits the infiltration of rainfall. From literature, there exist several approaches to determining the percentage of imperviousness for a catchment. One common approach involves categorizing the catchment based on its land use (Apartments, General vegetation, Car park, etc.) and applying a corresponding coefficient of imperviousness for that category of land. This approach however introduces uncertainties associated with the coefficient of imperviousness, since subcatchment characteristics can vary significantly even within the same category of land use. *Table 3* details the comparative variance in published coefficient values for the same type of land use.

Table 3: Coefficient of Imperviousness for land use category

Reference	Coefficient of Imperviousness			
	Apartment/Residential	General Vegetation	Carpark	Roads
Mason & Knight (2001)	0.30	0.05	-	-
Guo (2003)	0.70	0.07	0.74	1.00
Washburn et al. (2010)	0.84	0.02	-	0.91
County of San Diego (2008)	0.71	0.06	0.87	0.63

Since the use of these coefficients introduce large uncertainties into the constructed model, a direct measurement approach was adopted to determine catchment imperviousness. Georeferenced drainage plans were used in conjunction with the satellite imagery from Google Earth to polygonise pervious surfaces using the *Add Polygon* function in QGIS depicted in Figure 12.

The area of the polygons was subsequently extracted and processed to create *Figure 26* which depicts the imperviousness of individual sub-catchments within the study area.

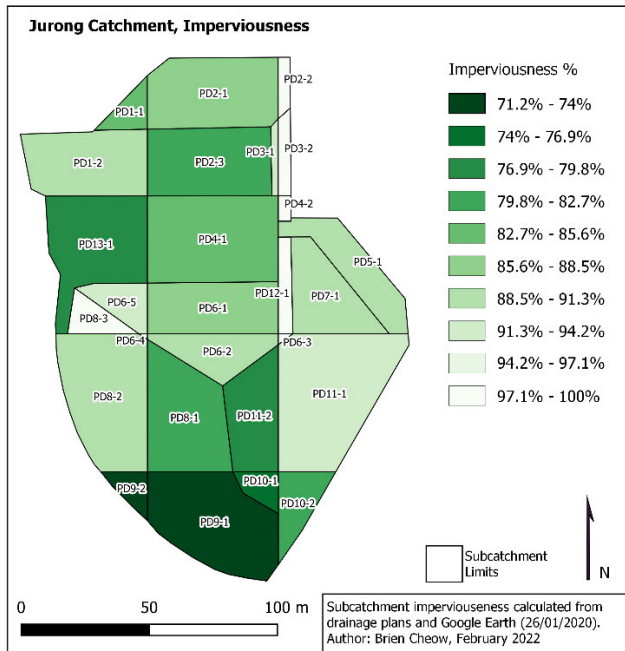


Figure 26: Subcatchment imperviousness

5.3.5 Sub-Catchment Curve Number Values

The Curve Number infiltration method has been covered in Chapter 5.2.3. This section describes how values used for the Jurong catchment model are acquired.

The NRCS, alongside many other hydrological textbooks, provides a highly structured methodology for estimating curve numbers (NRCS, 2004; McCuen, 1998; Bedient et al., 2013). In practice, however, these estimates are acquired from a published table in which curve number values are presented with respect to the land use type and the corresponding Hydrological Soil Group (HSG) (Appendix 10.6).

For Singapore, a local hydrological soil group map exists within the *Global Hydrological Soil Groups* dataset compiled by Ross et al. (2018).

Figure 27 depicts the HSG classification of the soils underlying the Jurong East Precinct. Soil investigation reports (INLIS, 2022) for the study area were subsequently used to satisfy the local accuracy of the *Global Hydrological Soil Groups* dataset.

As presented in Appendix 10.2, the geological stratification of the catchment consisted mainly of clayey soils of HSG D according to the NRCS classification and showed good agreement with the *Global Hydrological Soil Groups* dataset for the study area.

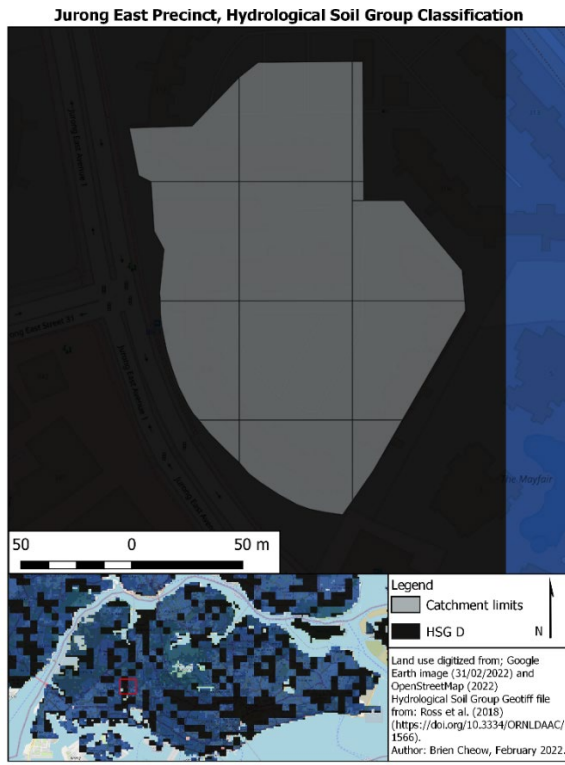


Figure 27: Hydrological Soil Group of Jurong East Precinct

To determine the curve number of the pervious areas in SWMM, only fully pervious land use categories were considered. This is because the assigned curve number for urbanized land use categories in Appendix 10.6 accounts for both the pervious and impervious parts of the subcatchment area and contradicts the modelling approach adopted in this study (*Chapter 5.3.4*).

Finally, it is important to note that the curve number obtained from Appendix 10.6 only applies to soils in their normal antecedent moisture condition, AMC II. In the unlikely event that temporal precipitation in Singapore fluctuates significantly, the curve number for soils in the AMC I condition (low moisture), and AMC III condition (high moisture) may be calculated with:

$$CN_I = \frac{4.2 \cdot CN_{II}}{10 - 0.058CN_{II}} \quad (19)$$

$$CN_{III} = \frac{23 \cdot CN_{II}}{10 - 0.13CN_{II}} \quad (20)$$

Where CN_x denotes the corresponding curve number for AMC X. For the purposes of this study, the pervious land use category was assumed to be pasture or rangeland of good hydrological condition, with soils of hydrological group D assumed to be in their normal antecedent moisture condition. Consequently, a CN value of 80 was applied for the modelling of infiltration in the site.

5.3.6 Sub-Catchment Surface Roughness (Manning's n)

In the physical space, the Manning's coefficient (n) is used to represent the resistance encountered by surface runoff when it meets the surface of the subcatchment (Gironás et al., 2009). And theoretically, the Manning's equation only applies to steady and uniform flow. However, as described in Chapter 5.2.1, idealization of the surface runoff allows SWMM to utilize the Manning's equation to compute the flow rate of surface runoff.

Distinct values of the Manning's roughness coefficient (n) for surface overland flow must thus be provisioned for pervious and impervious surfaces in the subcatchment. This is because n values for pervious surfaces are generally 10 times larger than that of impervious surfaces (Gironás et al., 2009) and can thus significantly affect the computation of surface runoff. In the field, there exists no consensus on the definite range of Manning's roughness coefficient n for overland flow as compared to channel flow due to the significant inconsistency in terrain characteristics, the disproportionately small flow depths, and the unpredictable transitions between laminar and turbulent flow (Rossman & Huber, 2016). Therefore, it is best to refer to similar areas of study to obtain the appropriate values. Chen et al. (2017) evaluated the Manning's n value for overland flow in an urban catchment and obtained by calibration an n value of 0.015 for impervious areas and 0.032 for pervious areas in the constructed model. Javaheri & Liong (2000) modelled the catchment composed of Upper Bukit Timah and utilized the values 0.012 for impervious areas and 0.3 for pervious areas.

The impervious and pervious values chosen for this study were assumed to homogenously characterize the surface roughness of the catchment. They considered the coefficients proposed in the two previous studies, as well as the values tabulated by Rossman and Huber (2016) (*Table 4*). Due to the associated uncertainty in the manning's n value, more conservative values were selected for this study. As a result, the Manning's coefficient for impervious and pervious surfaces were set at 0.012 and 0.24 respectively.

Table 4: Manning's n for Overland Flow (Rossman & Huber, 2016)

Impervious Surface	Surface	N value	Pervious Surface	Surface	N value
	Smooth asphalt	0.011		Fallow soils (no residue)	0.05
	Smooth concrete	0.012		Cultivated soils	
	Ordinary concrete lining	0.013		Residue cover < 20%	0.06
	Good wood	0.014		Residue cover > 20%	0.17
	Brick with cement mortar	0.014		Range	0.13
	Vitrified clay	0.015		Grass	
	Cast iron	0.015		Short, prairie	0.15
	Corrugated metal pipes	0.024		Dense	0.24
	Cement rubble surface	0.024		Bermuda Grass	0.41

5.3.7 Sub-Catchment Depression Storage

In SWMM, the depression storage, represented by depth d_p illustrated in Figure 23 is a volume that must be filled prior to the occurrence of runoff from both pervious and impervious areas (Rossman & Huber, 2016). For context, the parameter is used to signify the losses associated with initial abstractions from interception, surface wetting or ponding. Similar to the determination of the Manning's Roughness coefficient, the depression storage depth is subjected to significant spatial variability and there exist no direct measurement methods to deterministically establish its value. Due to the lack of literature and studies conducted locally, the recommended values of 0.05 inches for impervious areas and 0.15 inches for pervious areas proposed by the American Society of Civil Engineers (1992) were used in this study.

The SWMM model also includes another parameter, the percent of impervious area without depression storage, that models the immediate generation of runoff at the beginning of a storm event before the depression storage volume is satisfied. It physically represents the impervious surfaces that are close to drainage channels with no surface storage or ponding (Gironás et al., 2009). The recommended value of 25% was used for this parameter since no special circumstances are known to exist for the catchment (Gironás et al., 2009).

5.3.8 Sub-Catchment Land Use / Pollutant parameters

To simulate the water quality of surface runoff in SWMM, the event mean concentration (EMC) of TSS, TP and TN were procured from studies performed in accordance with the APHA Standard Methods for Examination of Water and Wastewater (Rice et al, 2012). It is important to note that land use plays a significant role in the observed pollutant concentrations in stormwater runoff (Duncan, 1999). For the HDB precincts of interest in this study, catchments are predominantly highly urbanized residential areas with a high proportion of roof areas that typically have lower levels of pollutants compared to surfaces like parklands, roads, and high footfall pedestrian pathways. As a result, EMC values obtained from catchments with similar properties were prioritized. Lastly, the weighted average of the EMCs from local studies was computed with equation 21:

$$x_{avg} = \frac{\sum_{i=1}^n (E_i \times X_i)}{\sum_{i=1}^n (E_i)} \quad (21)$$

Where x_{avg} is the weighted average of the EMC, n is the number of studies, E_i is the number of events used in each study, and X_i is the average EMC obtained from the study.

As shown in *Table 5*, the weighted average EMC values calculated from the three local studies reported a much lower magnitude between the three main pollutants when compared to the Australian dataset prepared by Duncan (1999) despite similar land use descriptions. This discrepancy may be due to the temporal and climatic differences in rainfall. Since Singapore experiences frequent, short-duration storm events all year round, the antecedent dry period necessary for pollutants to accumulate is relatively shorter when compared to Australia. As a

result, smaller loading rates/concentrations of pollutants were observed from Singapore's stormwater runoff as compared to the results reported by Duncan (1999). In this study, the weighted average values for Singapore were used to model/simulate stormwater quality in SWMM.

Table 5: Runoff water quality of urban precincts and comparison with literature studies

Study	Description	TSS EMC (mg/L)	TP EMC (mg/L)	TN EMC (mg/L)
Neo et al. (2022)	High Urban Residential (Singapore)	49.9	0.2	1.47
	No. of Events	17	17	17
Song et al. (2019)	High Urban Residential (Singapore)	31.92	0.07	1.16
	No. of Events	8	8	8
Lim (2003)	High Urban Residential (Singapore)	100	0.13	1.25
	No. of Events	188	111	106
Weighted Average (Singapore)		93.44	0.14	1.27
Duncan (1999)	High Urban Areas (Australia)	155	0.32	2.63
	No. of Events	247	116	139

TSS: total suspended solids, TP: total phosphorus, TN: total nitrogen.

5.4 Conduit and Junction Parameters in SWMM

For each conduit encoded in the SWMM model, the length, slope, Manning coefficient n, shape, width, and depth parameters must first be obtained. Twenty-one conduits and twenty junctions were conscientiously encoded in the model using the geo-referenced drainage plans. In SWMM, junctions only require the invert elevation parameter since their main function is to represent known invert elevation points within the drainage network.

5.4.1 Conduit parameters

Length and Slope

The invert elevations in the upstream and downstream regions for each conduit must be encoded into the model so that the slopes of drains in the catchment can be computed. Georeferenced drainage plans of the site were primarily used to determine the length and slope of the conduits. The measurement tool in QGIS was subsequently used to verify the length of the conduits.

Manning's Coefficient (n)

Similar to the simulation of overland flow in SWMM, the Manning's equation is used to simulate the open channel flow rate observed in the drainage network.

According to Rossman (2017), the Manning's n value for a cement-lined channel ranges between an n value of 0.01 and 0.015, while Javaheri & Liang (2000) estimated an n value of 0.012 for

concrete-lined channels. Due to the uncertainty associated with the actual value, a conservative approach was adopted and an n value of 0.01 was utilized for all conduits created in the model.

Channel geometry, depth, and width

Chapter 5.1.2 explained how the shape, depth and width of the conduits represented in SWMM were established for this study. Due to the lack of available data, typical rectangular drains were conservatively sized to ensure compliance with the local codes as well as to meet the discharge requirements of the catchment during a 10-year storm. Drains were assumed to have a width of 0.75m with a depth of 1m. It should be noted that the central c-channel used to convey flows during dry seasons was omitted in the modelling since its contribution during a high flow event was deemed to be insignificant.

5.4.2 Junction invert elevation

Junction elevations were determined with reference to the invert elevation values in the drainage plan as well as back-calculated as required using the slope value of the conduits.

5.5 Bioretention Basin and Detention Tank Parameters

As depicted in *Figure 2b*, the integration of stormwater management infrastructures from both the On-site Stormwater Detention Tank Systems Technical Guide & the Condensed Booklet on Engineering Procedures for ABC Waters Design Features were proposed to meet the runoff and communal objectives of the site.

With reference to the study area (*Figure 12*), the free grass patch would be replaced with a bioretention basin that is linked to an underground stormwater detention tank and a separate underground harvesting tank. The Bioretention Basin will act as the first treatment point for discharge from the catchment, and would first convey the treated water into the harvesting tank until it is full before draining excess water into the detention tank. During high intensity storm events (≥ 10 -yr storms), the high flow bypass channel of the bioretention basin would enable excess stormwater to be channeled directly into the detention tank, where it is collected and released into the downstream drainage system at controlled rates.

To perform a comparative assessment between the feasibility of the original UWHS presented in *Figure 2a* (Detention tank w/o Bioretention Basin) and the newly proposed UWHS presented in *Figure 2b* (Detention tank w Bioretention Basin), examples of both systems were modelled and analyzed in this study.

Figure 28 provides an overview of the two stormwater management systems analyzed in the context of this study.

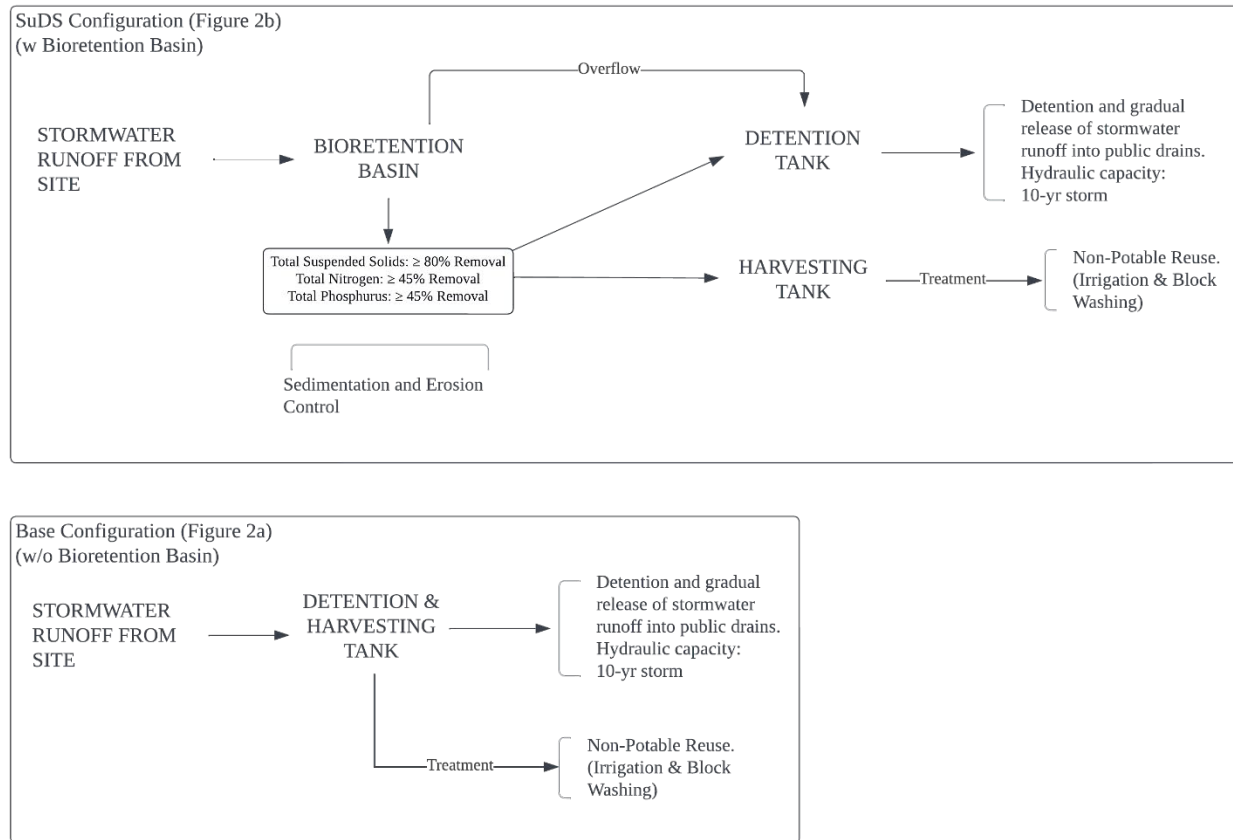


Figure 28: Proposed Stormwater Systems

5.5.1 Bioretention Basin parameters

For the initial parameterization of the Bioretention Basin, a design spreadsheet developed in accordance with the Condensed Booklet on Engineering Procedures for ABC Waters Design Features, PUB (2018) was used to determine the required Weirs, Channel Flow Area, Sediment Forebay, Infiltration Rate and Underdrain infrastructure. The computed parameters were then translated and encoded into the SWMM model either directly if the same equations were used in the model or through back-calculation of the specific parameters to ensure that model output results match the results from the design spreadsheet. In SWMM, the modelling of a Bioretention Basin is performed through the LID control editor where the process layers consisting of the Surface, Soil, Storage, Drain, and Pollutant removal of the bio-retention basin are encoded into the model.

5.5.1.1 Surface Layer

Within the Surface layer, the parameters berm height, vegetation volume fraction, surface roughness, and surface slope help characterize the surface of the Bioretention Basin.

In this study, the berm height was set to 300mm, while all other parameters were set to zero as recommended by the SWMM user manual prepared by Rossman (2015).

Surface Layer	Units	Value
Berm Height	mm	300
Vegetation Volume Fraction	-	0
Surface Roughness	Manning's N	0
Surface Slope	%	0

5.5.1.2 Soil Layer

The soil layer in the LID control editor describes the characteristics of the engineered soil mixture used in the bio-retention basin and consists of the thickness, porosity, field capacity, wilting point, conductivity, conductivity slope and suction head parameters.

For this study, the thickness and conductivity parameters were directly imported from the design sheet and were set at 600mm and 180mm/hr.

To obtain the porosity, field capacity, wilting point, conductivity slope and suction head parameters, the soil characteristics table provided in the SWMM user manual was used. The soil texture class of sand was selected, and parameters were set to 0.437, 0.062, 0.024, 53.92 and 43.16mm respectively.

Soil layer	Units	Value
Thickness	mm	600
Porosity	-	0.437
Field Capacity	-	0.062
Wilting Point	-	0.024
Conductivity	mm/hr	180
Conductivity Slope	-	53.92
Suction Head	mm	43.16

5.5.1.3 Storage layer

Within the storage layer, the data fields consisting of thickness, void ratio, seepage rate and clogging factor help characterize/describe the properties of the crushed stone/ gravel layer used in Bioretention Basins.

Similar to the parameters used for the preliminary design calculations, the thickness of the storage layer was set at 200mm. Since the PUB guidelines do not include the expected void ratio of the gravel beds, the values (0.5-0.75) recommended in the SWMM user manual were used. The void ratio was assumed to be 0.5 to be more conservative, and the seepage rate and clogging factor parameter were both set at 0 since the bio-retention basin was assumed to be lined with an impermeable membrane preventing exfiltration.

Storage layer	Units	Value
Thickness	mm	200
Void Ratio	-	0.5
Seepage Rate	mm/hr	0
Clogging Factor	-	0

5.5.1.4 Drain layer

For the underdrain system of the bio-retention basin, SWMM utilizes an equation consisting of a drain coefficient and drain exponent term to compute the flow rate capacity:

$$q = Ch^n \quad (22)$$

Where q is the outflow, h is the height of saturated media above the drain, C is the drain coefficient, and n is the drain exponent.

Documented in the SWMM user guide are several ways where equation 22 can be manipulated to represent the desired hydraulic behaviour of the underdrain exist. For this study, the approach adopted assumes that the drainage layer can carry all flows that enter the storage layer up to a certain maximum value. The maximum filtration rate or design flow for the under-drainage system is then estimated by applying Darcy's equation:

$$q_{max} = k_{sat} \cdot \frac{(d + d_m)}{d_m} \quad (23)$$

Where q_{max} is the maximum filtration rate, k_{sat} is the saturated hydraulic conductivity of the soil, d is the height of extended detention/ berm height, and d_m is the filter media depth.

The drain exponent in equation 22 is then set to zero and the drain coefficient is substituted with the maximum filtration rate computed from equation 23:

$$q = q_{max} \cdot h^0 \quad (24)$$

As a result of these calculations, the following parameters were encoded for the Drain layer of the Bio-retention basin in SWMM.

Drain Layer	Units	Value
Flow Coefficient	mm/hr	270
Flow Exponent	-	0
Offset	mm	0
Open level	mm	0
Close Level	mm	0
Control Curve	-	-

5.5.1.5 Pollutant removal layer

The treatment performance curves attached in the Condensed Booklet on Engineering Procedures for ABC Waters Design Features were used to determine the pollutant removal efficacy of the bioretention basin. The curves illustrate the relationship of the bioretention treatment performance as a function of the area fraction between the treatment area and the contributing catchment area. The table below depicts the pollutant removal efficacy encoded into the model.

Pollutant Removal Layer	Area (m ²)	Units	TSS	TN	TP
3% Fraction	514.71	% Removal	89	45.5	74
4% Fraction	686.28	% Removal	91	49	78
5% Fraction	857.86	% Removal	94	52	80

5.5.2 Detention Tank parameters

For the initial parameterization of the detention tank, design procedures documented in the On-site Stormwater Detention Tank Systems Technical Guide published by PUB (2021) were used.

Storm hydrographs for the catchment in the study were constructed using the modified rational method approach, and a generalized function for the storage volume was obtained by subtracting the area of the catchment's hydrograph from the area of the desired outflow hydrograph. The approach, however, requires iterative calculations to determine corresponding storage volumes for different storm durations in order to determine the maximum tank capacity required. Due to this inefficient procedure, a direct solution using the first derivative of the storage function was formulated. The On-site Stormwater Detention Tank Systems Technical Guide published by PUB (2021) describes the design procedures for detention tanks in greater detail.

To determine the total detention volume required for the proposed system (Figure 2b), the above-mentioned procedure to calculate the required detention volume was developed as a design spreadsheet. Subsequently, the detention tank volume was determined by subtracting the bioretention basin's available ponded volume from the total detention volume. The height of the detention tank was assumed to be 2.3m and the area of the orifice was computed using Torricelli's equation (Rossman, 2017; PUB, 2021):

$$Q_o = C_o A_o \sqrt{2gH_e} \quad (25)$$

Where Q_o is the orifice discharge rate, C_o is the orifice discharge coefficient, A_o is the area of the orifice, g is the acceleration due to gravity, and H_e is the effective head observed by the orifice.

The computed parameters were then directly encoded into the SWMM model whenever the same equations were used in the model representation or through back-calculation of the specific parameters to ensure model output results match the results from the design spreadsheet. In SWMM, the modelling of a detention tank is performed using the storage units (drainage system nodes that provide storage volumes).

5.5.2.1 Invert elevation

Similar to the junction elevations, the invert elevation of the detention tank was determined with reference to the invert elevation values in the drainage plan and backcalculated using the depth of the bioretention basin.

5.5.2.2 Depth & Storage Curve

As mentioned earlier, the height of the detention tank was assumed to be fixed at 2.3m for this study. To represent the height of the detention tank in SWMM, the depth parameter was set to 2.3m.

To represent the volumetric properties of the detention tank in SWMM, SWMM allows the user to define a tabular or functional storage curve to describe the surface area of the storage unit with respect to water depth. Since the detention tank is a regular rectangular box, the functional storage curve method expressed with Equation 26 was used.

$$Area = A \cdot (Depth)^B + C \quad (26)$$

Parameters B and C were set to zero while A was adjusted using the calculated surface area of the detention tank.

5.5.2.3 Omitted Parameters

In addition to physically representing storage infrastructure, the storage units in SWMM can be modelled to receive or discharge stormwater to specific nodes in the drainage network as well as lose water from both surface evaporation and seepage into the native soil. Since the above-mentioned mechanisms do not apply to the detention tank model in this study, their respective input parameters were set to zero.

5.5.2.3 Detention Tank Parameters

Table 6: Storage Unit Parameters

Bioretention Basin Area (m ²)	Detention Tank Volume (m ³)	Max Depth (m)	Storage Curve	Coefficient (A)	Exponent (B)	Constant (C)
514.71	399.53	2.3	Functional	0	0	173.71
686.28	348.06	2.3	Functional	0	0	151.33
857.86	296.59	2.3	Functional	0	0	128.95
0.00	553.95	2.3	Functional	0	0	240.85

Table 7: Orifice Parameters

Bioretention Basin Area (m ²)	Detention Tank Volume (m ³)	Type	Shape	Height (m)	Width	Inlet Offset	Discharge Coeff.
514.71	399.53	Side	Circular	0.465	-	0	0.6
686.28	348.06	Side	Circular	0.465	-	0	0.6
857.86	296.59	Side	Circular	0.465	-	0	0.6
0.00	553.95	Side	Circular	0.465	-	0	0.6

5.6 Rainfall Hyetographs and Discharge

According to Rossman & Huber (2016), the rainfall hyetograph is the single most important hydrological data requirement for a SWMM model. To construct a good representation of the physical catchment, model calibration must be done using site measured hydrographs and corresponding rainfall hyetograph due to the highly complex and varied composition of catchments. Regrettably, the study site along with many other precincts in Singapore do not have the instrumentation to collect these data. Additionally, the installation of these apparatus may not be economically feasible for the purposes of conducting an exploratory feasibility study for every precinct. As a result, synthetic hyetographs were constructed in place of measured rainfall data using the alternating block method and the Huff rainfall method. Model peak discharge rates were subsequently validated using the rational method described in the Code of Practice on Surface Water Drainage published by PUB (2018).

5.6.1 Rainfall Data

The formulaic representation of the IDF (Intensity-Duration-Frequency) curves provided by PUB can be used to create the synthetic hyetograph used for the SWMM model (*Table 8*). In the published charts, IDF curves are available for storm events with return periods ranging from 2 years to 100 years. The return period of a storm event is used to represent the statistical time interval in between the occurrence of rainstorm events of a given intensity. For this study, the IDF curve with a return period of 10 years was used in the SWMM model so that the performance of the implemented stormwater management systems can be assessed using the existing guidelines published by PUB.

Table 8: Singapore IDF Curves

Return Period (yr):	2	3	5	10	15	25	50	100
Rainfall Intensity* (mm/hr):	6078 $35.6 + T_d$	6889 $35.8 + T_d$	7783 $35.9 + T_d$	8913 $36.0 + T_d$	9526 $35.9 + T_d$	10300 $35.8 + T_d$	11336 $35.7 + T_d$	12362 $35.6 + T_d$

* T_d represents rainfall duration in minutes

5.6.2 Synthetic rainfall hyetographs

5.5.2.1 Huff Rainfall Distribution

There exist several hydrological methodologies for approaching the design of hyetographs for urban drainage systems, but among them, the Huff rainfall method is the most used approach. The method was first discovered by Huff (1967) through the analysis of rainfall data from 49 rain gauges across 400 square miles in east Illinois over the span of 12 years. The discovery that rainfall distribution could be characterized into four distinct groups depending on the maximum intensity occurring in the first, second, third or fourth quarter of the rainfall event, led to the creation of the Huff Curves (*Figure 29*).

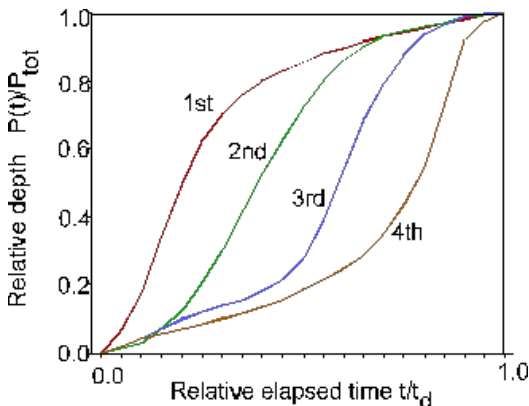


Figure 29: Huff's Curves (Smith, 2022)

Several studies have been conducted since the inception of Huff curves, with one study in Korea reporting that the Huff method estimated the longest critical storm duration and therefore the highest peak runoff for the selected watersheds in the study (Kang et al., 2013). In another study, Jun et al. (2018) analysed historical rainfall events in Singapore using the Huff method and discovered that local rainfall distributions tend to have characteristics reflected by the type 2 huff distribution curve. To construct the temporal distribution of rainfall intensity using the Huff method, the total depth of the design rainfall must first be computed using the IDF curves. The Huff rainfall distribution table is then used to derive the profile of the synthetic hyetograph using the total depth of rainfall.

5.5.2.2 Alternating Block Hyetograph

Similar to the Huff rainfall method, the alternating block method (Chow et al., 1988) is another commonly used approach in the design of synthetic hyetographs for urban drainage systems. In adopting the alternating block method, average rainfall intensities are calculated from the local IDF curve representing the desired return period based on the storm duration and time step of the final hyetograph. The highest rainfall intensity is assumed to occur at the centre of the total design storm duration, with the remaining blocks of rainfall arranged in descending order from the centre block, alternating from the right and then the left until the storm hyetograph is fully constructed.

5.5.2.3 Comparison of the Alternating Block Method and the Huff's Method

Due to the inherently different approach to constructing a synthetic hyetograph using the Alternating Block Method (ABM) and the Huff's method, model predicted discharge rates may vary significantly. As a result, synthetic hyetographs representing a 10-year, 4hr storm event were constructed using both methodologies and encoded into the SWMM model to investigate the differences in model results. The resulting discharge hydrographs were plotted and illustrated in *Figure 30*. The estimated peak discharge rate using the rational method was also plotted in the figure to serve as a basis for evaluation. From the figure, a significant difference between estimated peak discharge rates and the discharge profile of the catchment was observed. The ABM produced a much more aggressive ascent/peak in the discharge profile with a maximum

discharge rate estimated to be $0.922 \text{ m}^3/\text{s}$, approximately two and a half times larger in magnitude when compared to the $0.369 \text{ m}^3/\text{s}$ observed in the model constructed with the Huff's method.

When compared to the peak discharge rates predicted from the rational method, the ABM demonstrated better agreement with the estimated results as opposed to the Huff's method despite the findings in previous studies.

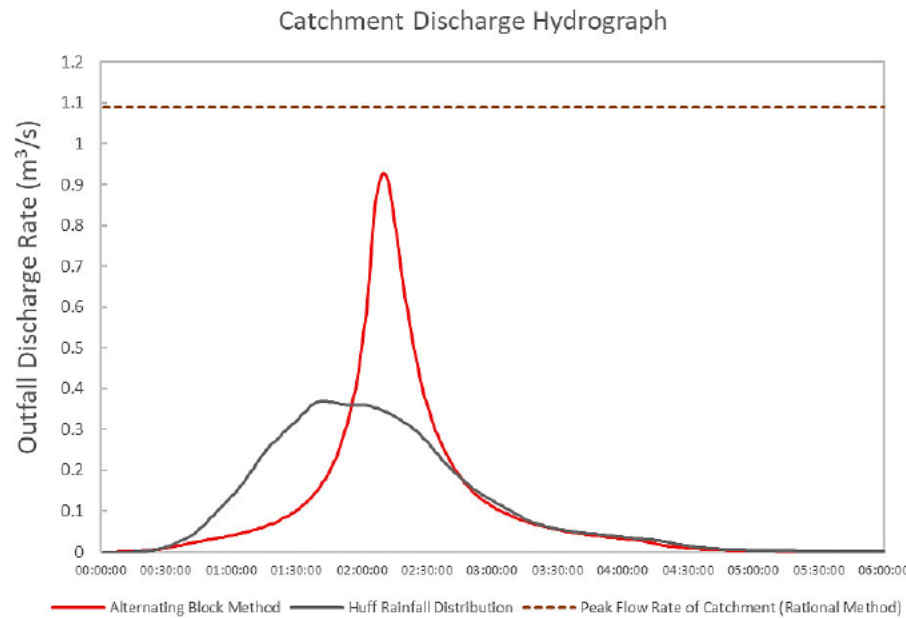
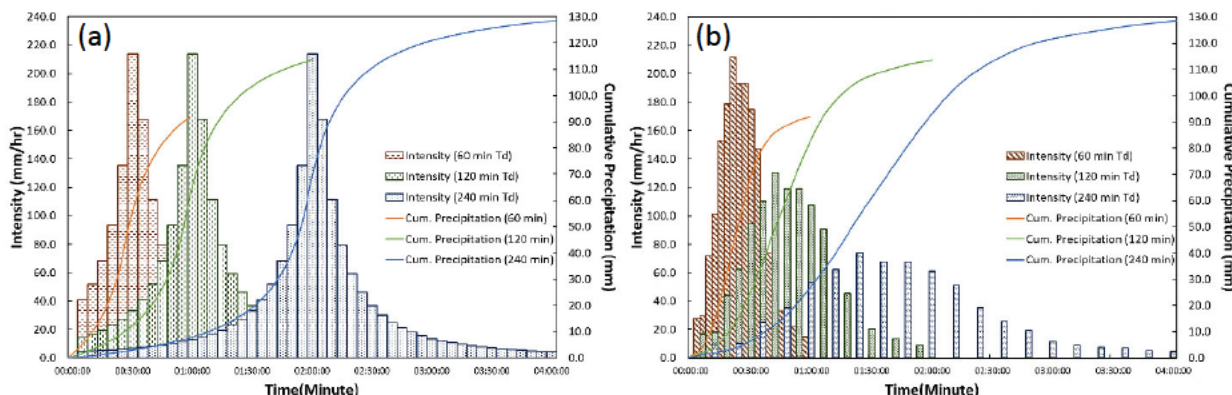


Figure 30: Comparison between the Alternating Block Method & Huff Rainfall Distribution

The significant mismatch in estimated peak discharge rates and the desire to make a well-rounded assessment of the two methodologies prompted a further investigation into the creation of synthetic hyetographs using the Huff's Method. Since the design rainfall duration can have a significant impact on the generation of rainfall intensity profiles, synthetic hyetographs for 10-year storm events of varying durations (1hr, 2hrs and 4hrs) were recreated using the Huff's method and the ABM. *Figure 31* illustrates the differences in the created rainfall distribution profiles.



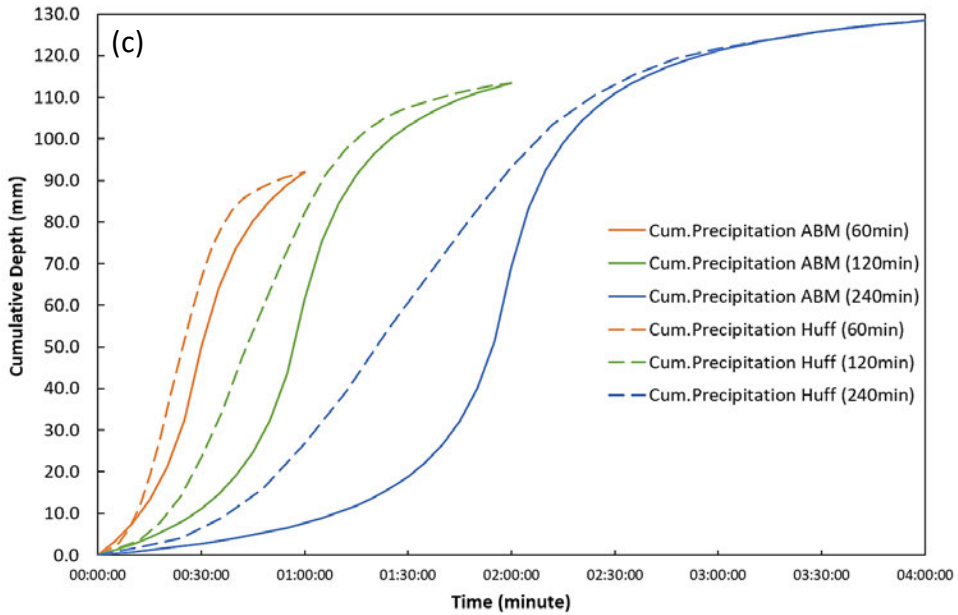


Figure 31: Synthetic Hyetograph Comparison: (a) ABM; (b) Huff's Method; (c) Cumulative Rainfall Depth

As depicted in the plotted hyetographs, the Huff's distribution produces hyetographs of decreasing peak rainfall intensity as storm duration increases. On the contrary, the ABM produces hyetographs with peak rainfall intensity of the same magnitude irrespective of the changing storm durations. This trend is further exemplified by the plotted cumulative rainfall depth graph. When constructing a 10-yr, 1hr design storm event, the huff method approximates a more aggressive ascend to the peak rainfall intensity, as reflected by the steeper gradient illustrated in the cumulative rainfall depth. However, as the duration of the storm event increases, the gradient/ aggressiveness of the Huff rainfall distribution diminishes. In contrast, the gradient of the cumulative rainfall depth for the ABM remained relatively consistent across the different design storm durations.

To investigate the impact of trends observed in the two approaches, a total of six model simulations were performed using the previously constructed hyetographs. The results were plotted for comparison and are illustrated in *Figure 32*.

As shown in the figure below, the profile of the simulated hydrographs exhibited similar characteristics to that observed in the constructed hyetographs (*Figure 31*). The discharge profile simulated with the Huff's rainfall distribution continues to show high sensitivity to the design storm duration. For a design storm duration of one hour, the Huff's method produced a marginally more conservative discharge profile for the study area with an estimated peak discharge rate of $0.978 \text{ m}^3/\text{s}$ as opposed to the estimated peak discharge rate of $0.907 \text{ m}^3/\text{s}$ from the ABM. However, as the design storm duration increases, the aggressive peak in the discharge profile derived from the Huff's method started to diminish with peak discharge rates significantly diverging from the values computed using the rational method. Due to the added complexity/ variability of applying the Huff's Method, the ABM was selected for the purposes of this study.

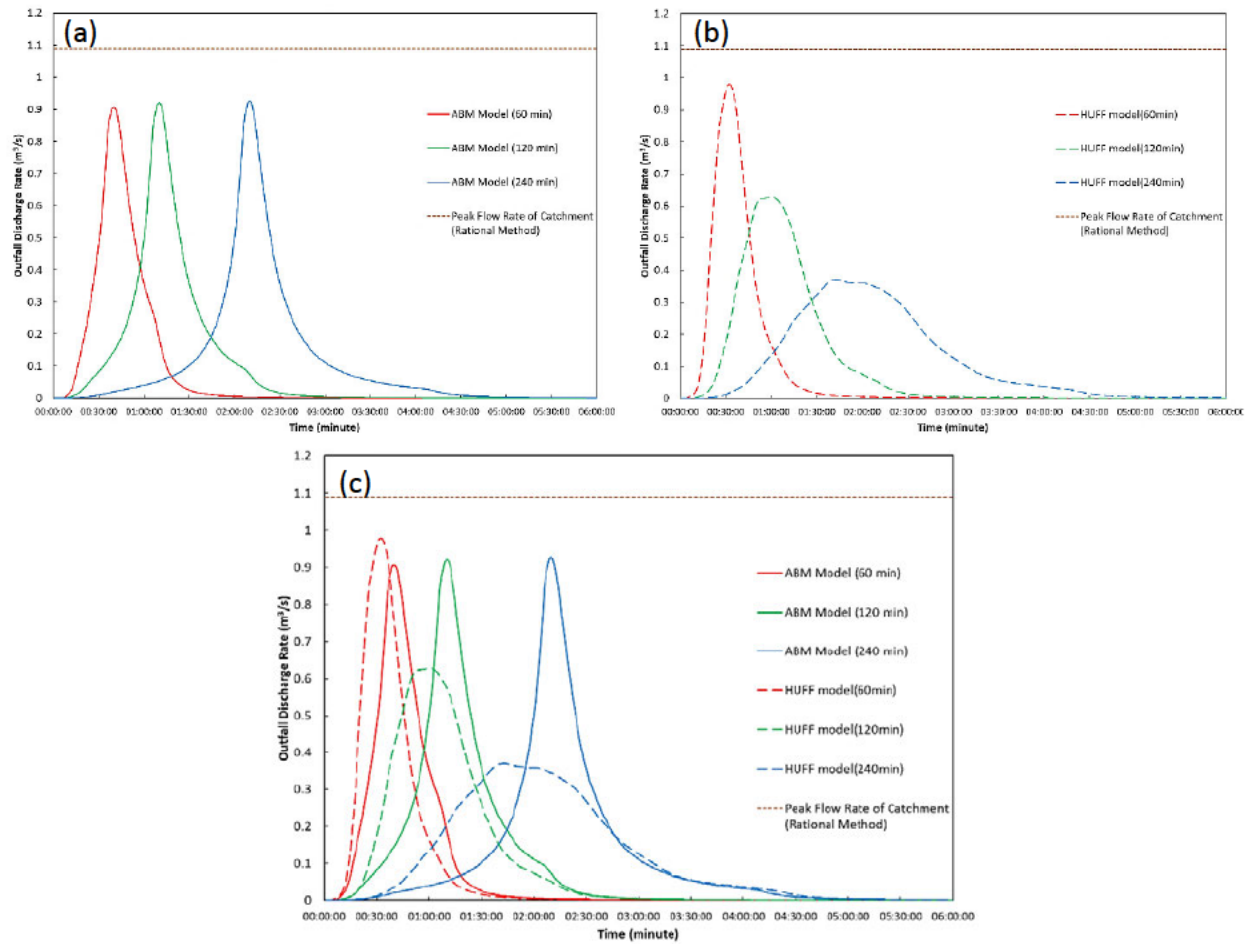


Figure 32: Estimated Hydrograph Comparison: (a) ABM; (b) Huff Method; (c) ABM & Huff Method Comparison

5.6.3 Discharge data

As mentioned above, it is not economically feasible to measure the hydrologic and hydraulic characteristics of every catchment to conduct an exploratory feasibility analysis. Nevertheless, the rational method approach adopted by PUB may be used to provide a good estimate of the expected peak discharge rate of the catchment in the absence of site measured data.

The Rational method was first proposed in 1851 by Thomas Mulvan (Dooge, 1957) through the following equation:

$$Q = \frac{1}{360} CIA \quad (27)$$

Where Q is the peak design runoff of the catchment (m^3/s), C is the dimensionless runoff coefficient, I is the average rainfall intensity of the design storm (mm/hr) and A is the catchment area (hectares). Although the formula has been widely applied in the field to compute the runoff of small urban catchments due to its low data requirements and ease of use (Hua et al., 2003), there exist limitations in the accuracy and uncertainty in the runoff coefficient characterizing the site. Nonetheless, in situations where there are severe limitations in available site data, the

rational method approach offers the means to estimate the hydrological response of the catchment.

In the Code of Practice on Surface Water Drainage published by the PUB (2018) and the On-site Stormwater Detention Tank Systems Technical Guide (PUB, 2021), the runoff coefficient (C) in Singapore can be categorized based on the density and type of development characterizing the catchment or the type of surface cover characterizing the catchment. *Table 9* depicts the general characteristics of a fully developed catchment and its associated runoff coefficient. Due to the uncertainties associated with a generalized land use runoff coefficient, the runoff coefficients for the impervious and pervious areas were used to compute the peak discharge of the catchment.

Table 9: Singapore's Runoff Coefficient

Characteristics of catchment when fully developed	Runoff Coefficient (C)	Source
Roads, highways, airport runways, paved areas	1.00	Code of Practice (PUB, 2018)
Urban areas fully and closely built up	0.9	Code of Practice (PUB, 2018)
Residential/industrial areas densely built up	0.8	Code of Practice (PUB, 2018)
Residential/industrial areas not densely built up	0.65	Code of Practice (PUB, 2018)
Rural areas with fishponds and vegetable gardens	0.45	Code of Practice (PUB, 2018)
Impervious Areas	1.00	Technical Guide (PUB, 2021)
Pervious Areas	0.45	Technical Guide (PUB, 2021)

Subsequently, local IDF curves were used to determine the average rainfall intensity I. To obtain the maximum peak runoff using the rational method, the time of concentration for the catchment is used in place of the rainfall duration to determine average rainfall intensity I from the IDF curves. The time of concentration and return periods adopted for the design of stormwater management infrastructure in Singapore have been categorized and tabulated by the PUB in relation to the area of the catchment as shown in *Table 10* and *Table 11* respectively.

Table 10: Selection of Storm Return Period (PUB, 2018)

Area served by Drainage Systems	Return Period
Catchment of less than 100 ha	10 years
Catchment of 100 to 1000 ha	25 years
Catchment of more than 1000 ha or critical installations	50 to 100 years

Table 11: Time of Concentration (PUB, 2021)

Site Area (ha)	Time of Concentration (min)
0.2 – 2.0	5
2.0 - 6.0	10
6.0 - 10.0	15
≥ 10	15*

5.7 Detail level/Resolution of SWMM Model

Although it is possible for a SWMM model to represent catchment detail down to an infinitesimal scale, the amount of detail required depends upon the purpose of the simulation (Rossman & Huber, 2016). Ideally, the catchment model should include detailed information on the catchment hydrological characteristics and the drainage network, however, the lack of available data with regards to the drainage details (Size, Geometry, etc), and site measured hyetographs and hydrographs may result in the construction of an aberrant model with no means of validation other than the rational method.

According to Rossman & Huber (2016), if the purpose of the simulation is to determine the flow at the outlet of the catchment, it is usually acceptable to encode minimal detail (few or one subcatchment, one or no channel/pipes) into the SWMM model. Since the necessary data to carry out sophisticated calibration and validation of the model is likely to be unavailable, the inclusion of the drainage network may introduce greater uncertainty and inaccuracies into the model. Thus, two SWMM models of varying resolution were constructed to investigate the impact of removing the drainage network from the catchment.

5.7.1 Output Hydrograph Evaluation

The visual comparison of model-simulated hydrographs can provide the first indication of the model's performance. As a result, output hydrographs simulated using the Dynamic Wave Routing method from the varied SWMM models were observed to identify the temporal change in magnitude of peak discharge rates, and the profile of the flow recession curves. The peak flows at the outlet of the catchment were also compared and validated using the peak discharge rate computed with the rational method in accordance with the Code of Practice on Surface Drainage published by PUB (2018).

Figure 33 shows the resulting runoff hydrographs for the two SWMM models subjected to a 10-year design storm. From the figure, it can be seen that the inclusion or omission of the drainage network in the SWMM model affects the estimated catchment response and provides different results primarily in peak flowrate estimates. For the SWMM model with a drainage network, a delay in the simulated catchment response was observed. The shape of the output hydrograph was also slightly "flatter" with significantly reduced peak flow rates when compared to the peak flow computed using the rational method. Due to the considerable disparity between the model results and the rational method, the drainage network was omitted from the SWMM model for the remainder of this study.

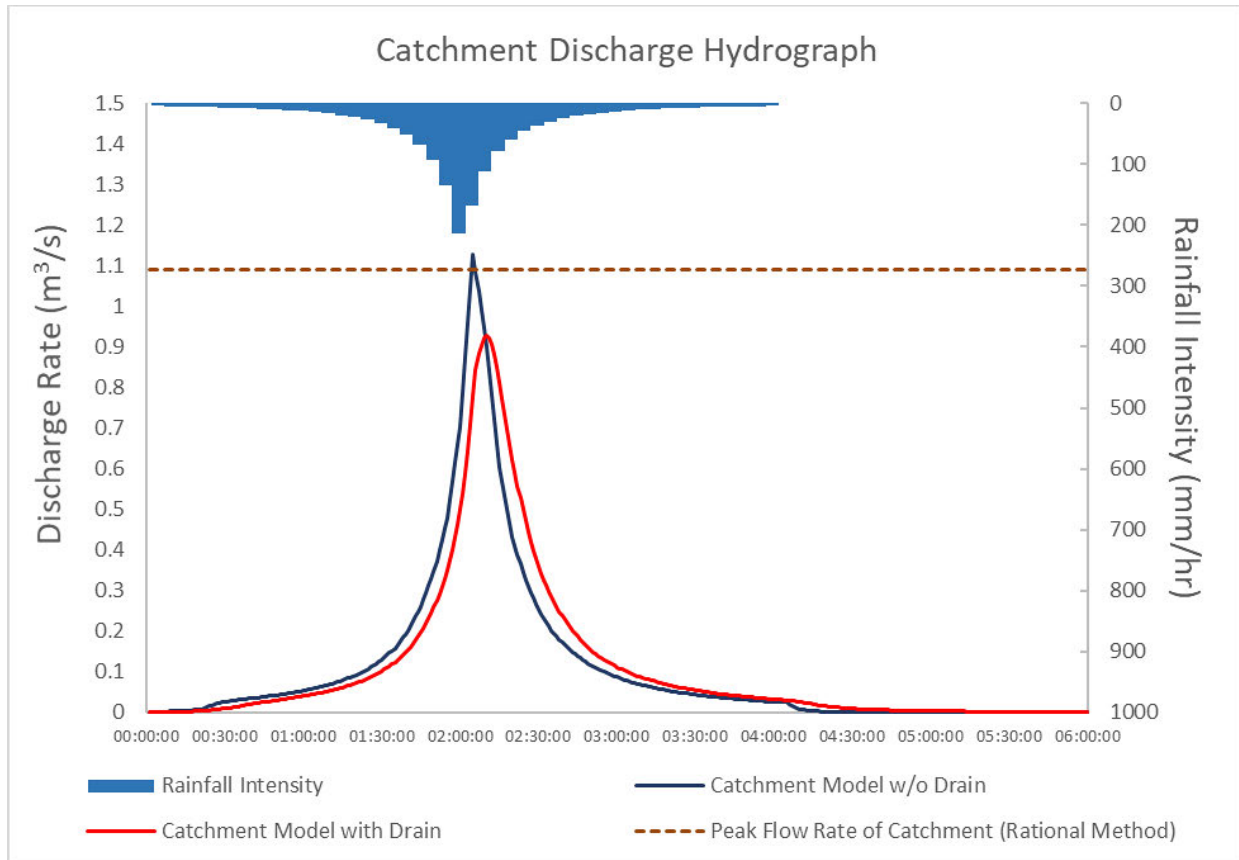


Figure 33: Simulated hydrographs for catchment models subjected to a 10-year design storm

5.8 Validated sizes of the UWHS System & Performance

Finally, having developed four separate SWMM models to represent the configurations of the UWHS, the rainfall-runoff simulation model was executed to validate the predetermined sizes of the detention tank and to ensure that the peak discharge rate of the catchment complies with local regulatory requirements. For the simulations performed, an ABM synthetic hyetograph reflecting a 10 year return period storm event (240min) was encoded and used as the basis of evaluation. The simulations were performed using the dynamic wave routing model, and a time step of 5 min, and 0.1s were used for the hydrological simulation and hydraulic/routing simulation respectively.

As a result of the validation and adjustment process, the final UWHS component sizes for the four configurations are as follows (Table 12):

Table 12: Validated Storage Unit Parameters

Case	Bioretention Basin Area (m ²)	Detention Tank Volume (m ³)	Max Depth (m)	Storage Curve	Coefficient (A)	Exponent (B)	Constant (C)
S4	0	547.40	2.3	Functional	0	0	238.00
S1	514.71	510.60	2.3	Functional	0	0	222.00
S2	686.28	496.80	2.3	Functional	0	0	216.00
S3	857.86	473.80	2.3	Functional	0	0	206.00

To evaluate the hydrologic and treatment performance of the UWHS configurations, a system of hydrologic performance indicators and treatment performance indicators were developed. In particular, the reduction rates of runoff volume (R_v), peak flow ($R_{q, \text{peak}}$), concentration time(R_{tc}) and runoff pollution reduction consisting of TSS (R_{tss}), TN (R_{tn}), TP (R_{tp}) were computed to comparatively assess the baseline performance of the four configurations.

5.8.1 Hydrological Performance Metrics

To determine the relative improvements in runoff volume reduction when compared to the base case scenario, the runoff volume (R_v) reduction rate was computed using the following equation:

$$R_{v(i)} = \frac{vol_{base} - vol_i}{vol_{base}} \times 100\% \quad (28)$$

Where $R_{v(i)}$ is the runoff volume reduction rate for configuration i , vol_{base} is the outflow volume of the catchment without any hydrological infrastructure, and vol_i is the outflow volume of the catchment under configuration S1, S2, S3 and S4.

The peak flow ($R_{q, \text{peak}}$) reduction rate was calculated in a similar way:

$$R_{q,peak(i)} = \frac{q_{base} - q_i}{q_{base}} \times 100\% \quad (29)$$

Where $R_{q,peak(i)}$ is the peak flow reduction rate for configuration i , q_{base} is the peak flow rate from the catchment without any hydrological infrastructure, and q_i is the peak flow rate under configuration S1, S2, S3 and S4.

While the concentration time (R_{tc}) delay rate was defined as:

$$R_{tc(i)} = \frac{TC_i - TC_{base}}{TC_{base}} \times 100\% \quad (30)$$

Where $R_{tc(i)}$ is the concentration time delay rate for configuration i , TC_{base} is the concentration time of the catchment without any hydrological infrastructure, and TC_i is the catchments concentration time under configuration S1, S2, S3 and S4.

5.8.2 Treatment Performance Metrics

To determine the relative improvements in runoff volume reduction when compared to the base case scenario, the TSS (R_{tss}) reduction rate was computed using the following equation:

$$R_{tss(i)} = \frac{TSS_{base} - TSS_i}{TSS_{base}} \times 100\% \quad (31)$$

Where $R_{tss(i)}$ is the TSS reduction rate for configuration i , TSS_{base} is the TSS pollution load of the catchment without any hydrological infrastructure, and TSS_i is the TSS pollution load of the catchment under configuration S1, S2, S3 and S4.

The TN (R_{tn}) reduction rate was calculated in a similar way:

$$R_{tn(i)} = \frac{TN_{base} - TN_i}{TN_{base}} \times 100\% \quad (32)$$

Where $R_{tn(i)}$ is the TN reduction rate for configuration i , TN_{base} is the TN pollution load of the catchment without any hydrological infrastructure, and TN_i is the TN pollution load of the catchment under configuration S1, S2, S3 and S4.

While the TP (R_{tp}) reduction rate was defined as:

$$R_{tp(i)} = \frac{TP_{base} - TP_i}{TP_{base}} \times 100\% \quad (33)$$

Where $R_{tp(i)}$ is the TP reduction rate for configuration i , TP_{base} is the TP pollution load of the catchment without any hydrological infrastructure, and TP_i is the TP pollution load of the catchment under configuration S1, S2, S3 and S4.

The computed hydrologic and treatment performance metrics for configurations S1, S2, S3 and S4 when subjected to the same 10 year return period ABM synthetic hyetograph is reflected below (Table 13 & Figure 34):

Table 13: Hydrological & Treatment Performance of UWHS

Case	Bioretention Basin Area (m^2)	Detention Tank Volume (m^3)	Hydrological Performance			Treatment Performance		
			R_v	$R_{q,peak}$	R_{tc}	R_{tss}	R_{tn}	R_{tp}
S4	0	547.40	0%	43%	7%	0%	0%	0%
S1	514.71	510.60	6%	43%	17%	26%	22%	20%
S2	686.28	496.80	6%	43%	17%	33%	29%	27%
S3	857.86	473.80	6%	43%	17%	40%	36%	32%

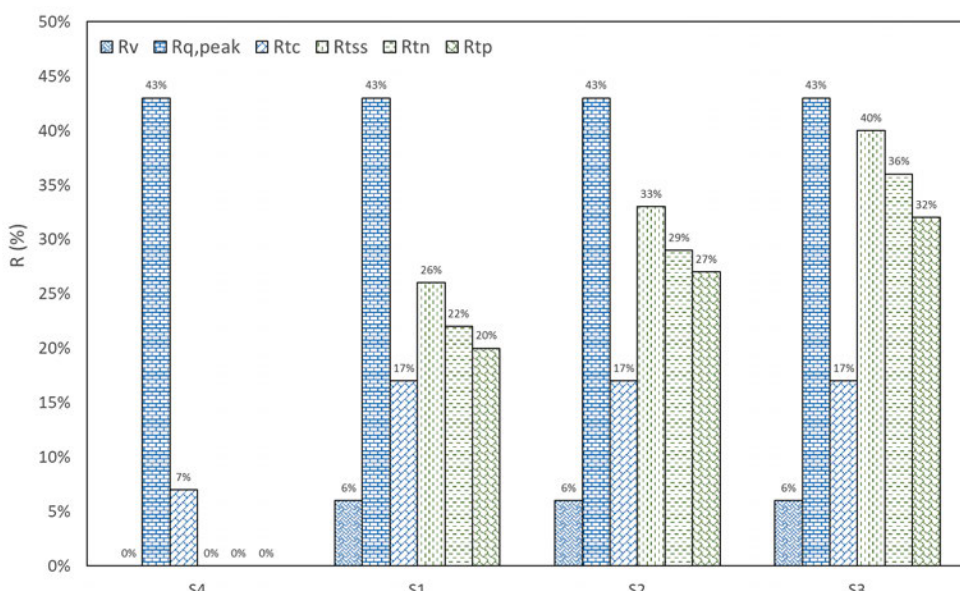


Figure 34: Hydrological & Treatment Performance of UWHS

5.9 Sensitivity analysis of input parameters

In this chapter, a parametric study of the SWMM model was conducted using the ABM hyetograph. Although a conscientious effort was made to extract accurate input parameters for the sub-catchment, the lack of site-specific discharge and rainfall data in this study meant that the constructed model could not be calibrated or validated against the actual hydrological response of the catchment. As a result, a total of fifty-seven tests simulations were performed to ascertain the sensitivity and impact of the catchment parameters on the model outputs. The knowledge obtained from these tests will provide the necessary background for deeper analysis, contributing to an improved understanding of the model behaviour, and thus guiding future attempts at model calibration and data collection.

5.9.1 Local Sensitivity Analysis

Local sensitivity analysis (also known as “point sensitivity analysis”) examines the sensitivity of parameters to simulation results at certain parameter values (Kleidorfer, 2010). As sensitivity may vary depending on the value being analysed, the selection of the parameter values should be within the expected range of values applicable to the model. According to Kleidorfer (2010), these values can be obtained from literature studies or from preliminary analysis.

To quantify the local sensitivity of a parameter, the slope of the linearised function $f(O_j)$ in dependency of the model parameters O_j was computed (*Equation 21, Figure 35*).

$$s(O_j) = \frac{\partial f(O_j)}{\partial O_j} \quad (34)$$

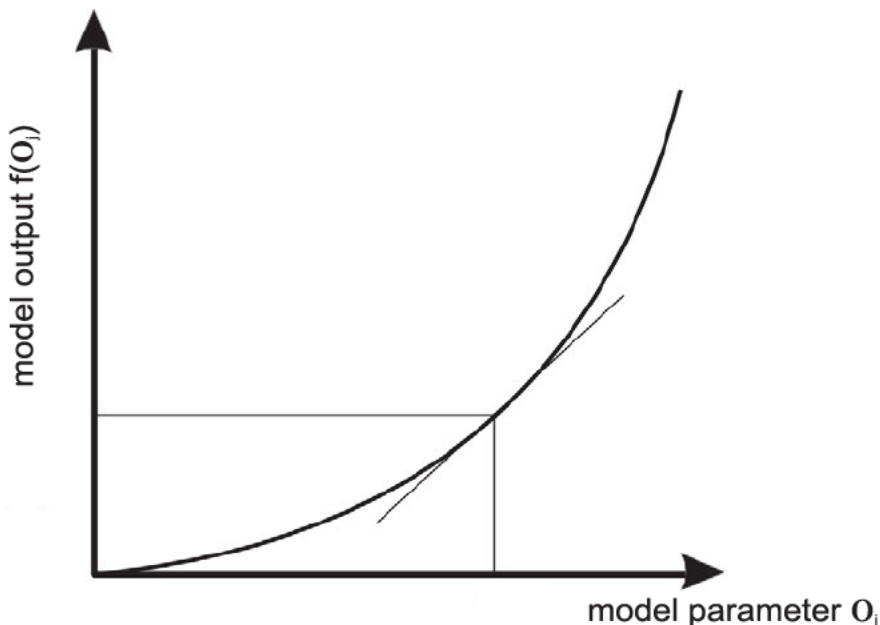


Figure 35: Local parameter sensitivity slope (Adapted: Kleidorfer, 2010)

Due to the discretization of the SWMM model, multiple sub-catchments with disproportional weightages contribute toward a single model output. This resulted in complications when attempting to relate the absolute changes in input parameters for each subcatchment to the model result. Thus, the terms $\partial f(O_j)$ and ∂O_j in Equation 21 was expressed as the percentage change in values relative to the default values for the model to permit the computation of parameter sensitivity.

The evaluation of the parameter sensitivity for the subcatchment width, area, slope, Manning's N for overland flow, Impervious percent and Curve number was performed by altering individual input parameters by $\pm 10\%$ and $\pm 20\%$ wherever reasonable and comparing the variations in model results. *Table 14* illustrates the range of input parameters derived for the purposes of the sensitivity study.

Table 14: SWMM model parameters

Parameter	Abbreviation	Unit	Range of Values		
			Default	Varied +20%	Varied -20%
Subcatchment Width	Width	m	[7.02, 202.54]	[8.42, 243.05]	[5.62, 162.03]
Subcatchment Area	Area	ha	[0.004, 0.275]	[0.005, 0.330]	[0.003, 0.220]
Surface Slope	%Slope	%	[0.5, 7.44]	[0.60, 8.93]	[0.4, 5.95]
Manning's N for impervious area	Nimperv	-	[0.012]	[0.014]	[0.01]
Manning's N for pervious area	Nperv	-	[0.24]	[0.288]	[0.192]
Impervious percent	%Impervious	%	[71.23, 93.21]	[85.48, 100]	[56.98, 74.57]
Curve Number	CN	-	[80]	[89]	[74]

5.9.2 Sensitivity Analysis Results

A summary of the findings from the sensitivity analysis is described in this section. The results illustrated in *Figure 36* indicate that the Area parameter is the most sensitive input contributing to changes in the model results, followed by the %Impervious parameter and then the CN parameter.

The relative change to the point sensitivity of model parameters when varied by $\pm 20\%$ typically ranges between 0.01% to 0.1% denoted by the error bars in the figure. However, point sensitivity variation observed from the %Impervious parameter was discernibly larger than that of other input parameters.

This irregularity was found to be attributed to several sub-catchments reaching the absolute limit of the parameter (100%) before the full 20% increase/change can be applied. Nevertheless, the point sensitivity of the %Impervious parameter was deemed to provide a good indication of the actual parameter sensitivity since its value was derived from the average of all its derivatives/contributing subcatchments in the model.

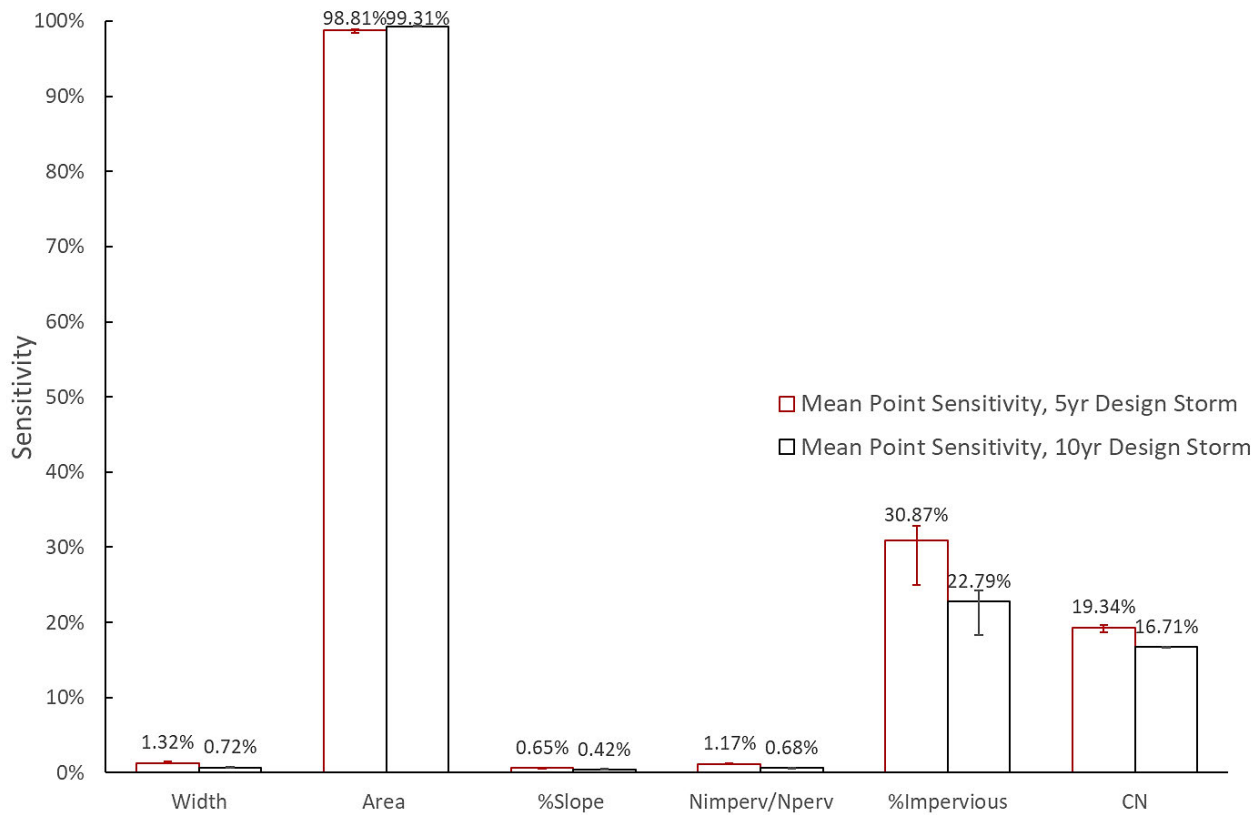


Figure 36: Mean sensitivity of model parameters

Additionally, the point sensitivity of all parameters besides the Area parameter reflected marginally reduced sensitivity as the intensity of the storm event increased. This observed trend underlines the declining importance of hydrological processes associated to losses and runoff generation as the intensity of the storm increases.

It is hypothesized that as rainfall intensity increases, the catchment's surface converges to an arbitrary point of hydrologic saturation or flooding. Consequently, as the catchment advance towards this point of saturation, the land surface represented in the model begins exhibiting behaviour similar to that of an impervious surface thus nullifying the effects of the hydrological processes represented by the input parameters.

These results also help to provide confidence in the previously constructed hydrological model since extracted parameters with high uncertainty, typically ranks in the lower end of the sensitivity analysis results.

The observed impacts of the six parameters covered in this study have been summarized in Table 15 to guide future calibration efforts.

Table 15: Sensitivity of input parameters

Parameter	Sensitivity Rank	Uncertainty Rank	Effect on hydrograph	Effect of increase on runoff volume	Effect of increase on runoff peak	Comments
Subcatchment Width	4	2	Affects shape	Increase	Increase	Increasing the width parameter results in a faster catchment response. Hydrographs are generated with faster, higher, and narrower peaks. Runoff volume may be marginally affected where the reduction in width for pervious areas allows more time for infiltration.
Subcatchment Area	1	6	Significant	Increase	Increase	Amplifies the shape and magnitude of the hydrograph. Impact may be reduced for a highly porous catchment.
Surface Slope	6	1	Affects shape	Increase	Increase	Similar to the width parameter but less sensitive.
Manning's N for Overland Flow	5	4	Affects shape	Decrease	Decrease	Inverse effect to the width parameter.
Impervious percent	2	5	Significant	Increase	Increase	Increasing the Impervious percent parameter significantly impacts the rising limb of the catchment response, resulting in hydrographs with faster and higher peaks.
Curve Number	3	3	Moderate	Increase	Increase	Increasing the Curve Number parameter results in a moderately amplified catchment response, where hydrographs with narrower and higher peaks are produced. Reduction of the parameter will increase infiltration capacity of the pervious areas.

5.7.2.1 Subcatchment Width Parameter (Width)

The output hydrographs of the parametrically varied models for the width parameter were computed for storm events with a return period of 5 years and 10 years and plotted in a graph as illustrated in *Figure 37*. As observed from the figure, the width parameter variations barely impacted the discharge profile of the catchment across both the storm events. Nevertheless, it is desirable to examine the impacts that can be expected from varying the width parameter for future calibration.

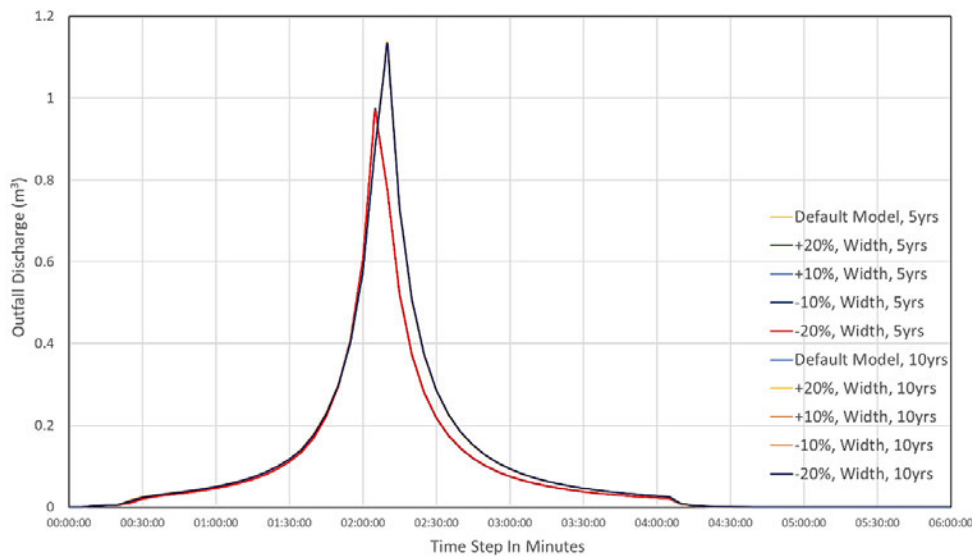


Figure 37: Model Hydrographs (Width)

Since the impact of the width parameter is difficult to perceive from the figure depicting the entire discharge profile of the catchment, another graph was plotted by utilizing the relative change in discharge to investigate the influence of the parameter on the catchment's hydrograph (*Figure 38*). From the figure below, a positive shift in discharge magnitude was observed on the rising limb of the hydrograph when subcatchment widths were increased from default values. Additionally, a negative shift in discharge magnitude on the falling limb of the hydrograph was also observed. Consequently, when subcatchment width was reduced, the opposite effect was observed, where discharge magnitudes on the rising limb of the hydrograph were negatively impacted while discharge magnitudes on the falling limb were subjected to a positive shift.

Due to the observed impacts resulting from this parametric study, the width parameter was deemed to have a narrowing or widening effect on the discharge hydrograph of the catchment, where the gradient of the rising and falling limbs in the hydrograph was either amplified or dampened depending on the subcatchment width parameter. Additionally, the width parameter was observed to have a greater impact on the catchments discharge profile for less intense storms.

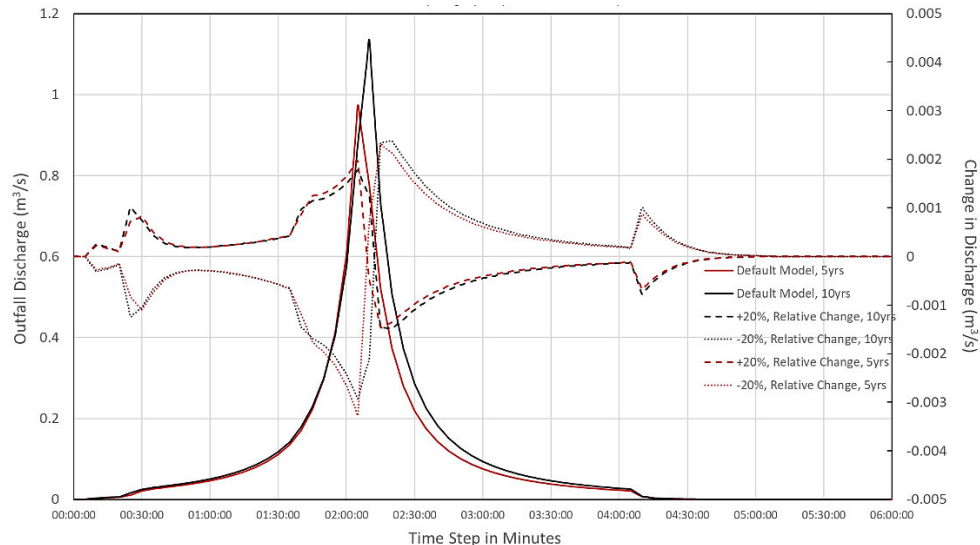


Figure 38: Change in Model Discharge Hydrographs (Width)

5.7.2.2 Subcatchment Area Parameter (Area)

The output hydrographs of the parametrically varied models for the Area parameter were computed for storm events with a return period of 5 years and 10 years and plotted in a graph as illustrated in *Figure 39*. As observed from the figure, the Area parameter variations significantly impacted the discharge profile of the catchment across both the storm events. When plotting the model results, it was observed that a 20% increase or decrease in the Area parameter, resulted in a corresponding change of equal magnitude in the model output results.

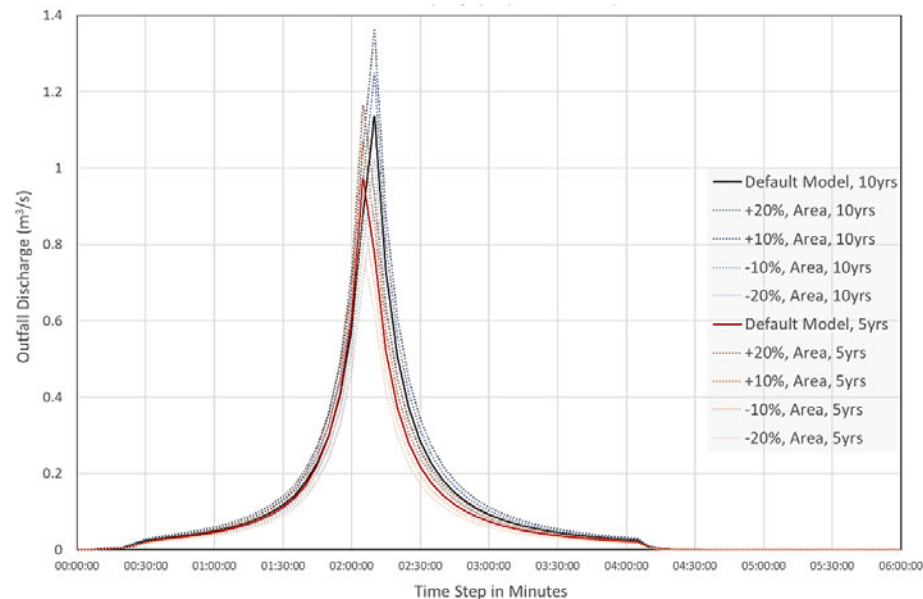


Figure 39: Model Hydrographs (Area)

Since it is desirable to examine the impacts that can be expected from varying the Area parameter for future calibration purposes, a separate graph was plotted by computing the relative change

in discharge values resulting from the change in Area parameter values (*Figure 40*). From the figure below, a positive shift in discharge magnitude was observed throughout the entire discharge hydrograph when the Area parameter was increased from default values. On the contrary, when the Area parameter was artificially reduced, discharge magnitudes across the entire hydrograph were negatively impacted. Due to the observed impacts of the Area parameter with regards to the model hydrograph, the Area parameter was deemed to have an amplifying effect on the discharge hydrograph of the catchment, where the volume and intensity of precipitation from a storm event were amplified depending on the subcatchment area parameter.

Additionally, the Area parameter was observed to have a greater impact on the catchment's discharge profile for storm events of increasing intensity. The observed change influenced by the area parameter was measured to be 2 orders of magnitude larger than that of the Width parameter.

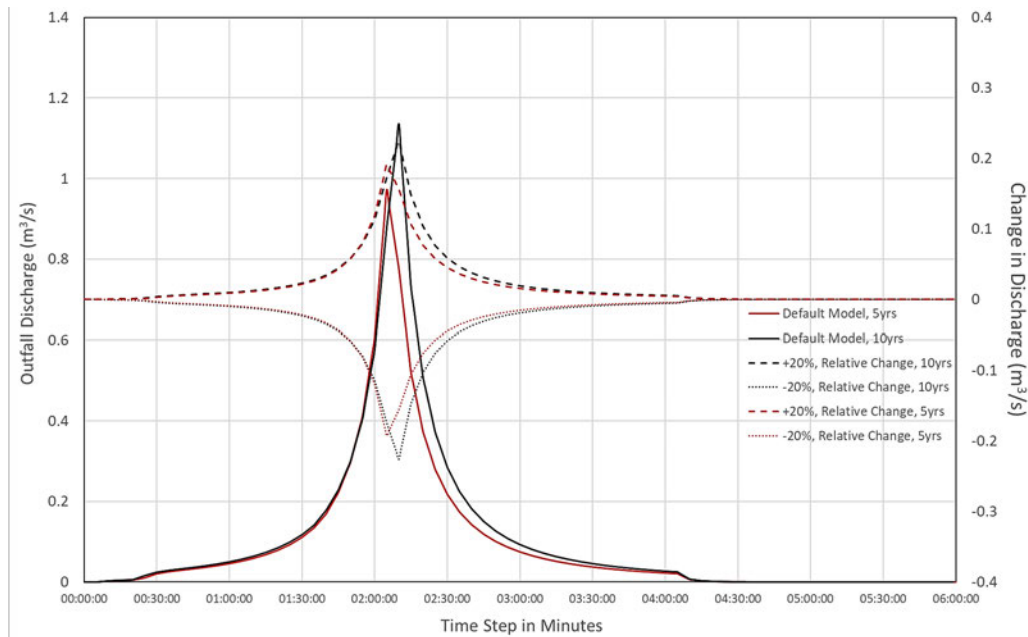


Figure 40: Change in Model Discharge Hydrographs (Area)

5.7.2.3 Slope Parameter (%Slope)

The output hydrographs of the parametrically varied models for the %Slope parameter were computed for storm events with a return period of 5 years and 10 years and plotted in a graph as illustrated in *Figure 41*. Similar to the width parameter, variations made to the %Slope parameter barely impacted the discharge profile of the catchment between the two storm events of different intensities. In fact, the %Slope parameter was found to have the least impact on model results across the two storm events used for this study (Figure 36). Nevertheless, it is important to examine the impacts that can be expected from varying the %Slope parameter for future calibration purposes.

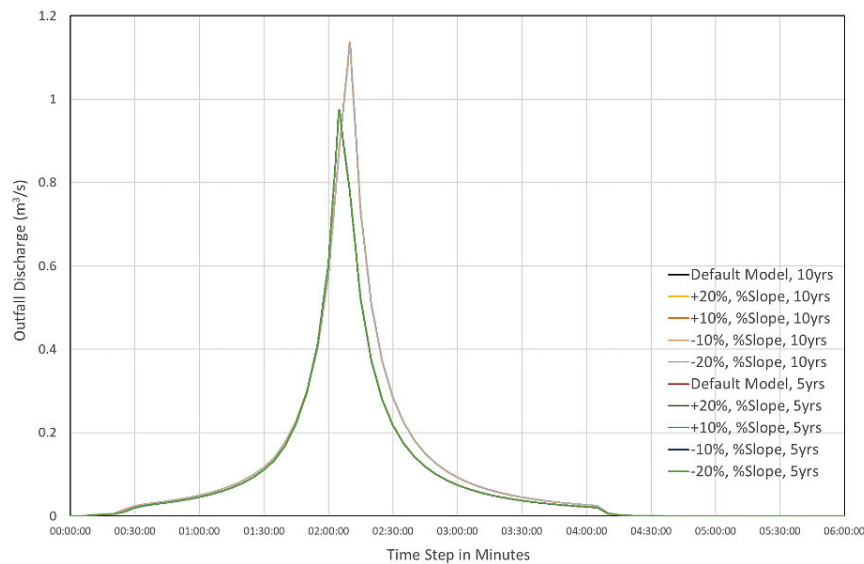


Figure 41: Model Hydrographs (%Slope)

Since the impacts of the %Slope parameter are difficult to identify from the figure depicting the entire discharge profile of the catchment, another graph was plotted by utilizing the relative change in discharge to investigate the influence of the parameter on the catchment's hydrograph (*Figure 38*). From the figure below, a positive shift in discharge magnitude was observed for the rising limb of the hydrograph when subcatchment %Slope parameters were increased from the default values. Additionally, for the falling limb of the same hydrograph, a negative shift in discharge magnitude was observed.

For the model with the reduced subcatchment %Slope, the opposite effect was observed where discharge values on the rising limb of the hydrograph were negatively impacted while discharge values on the falling limb experienced a positive shift. These impacts although of smaller magnitude, strongly resemble that of the Width parameter.

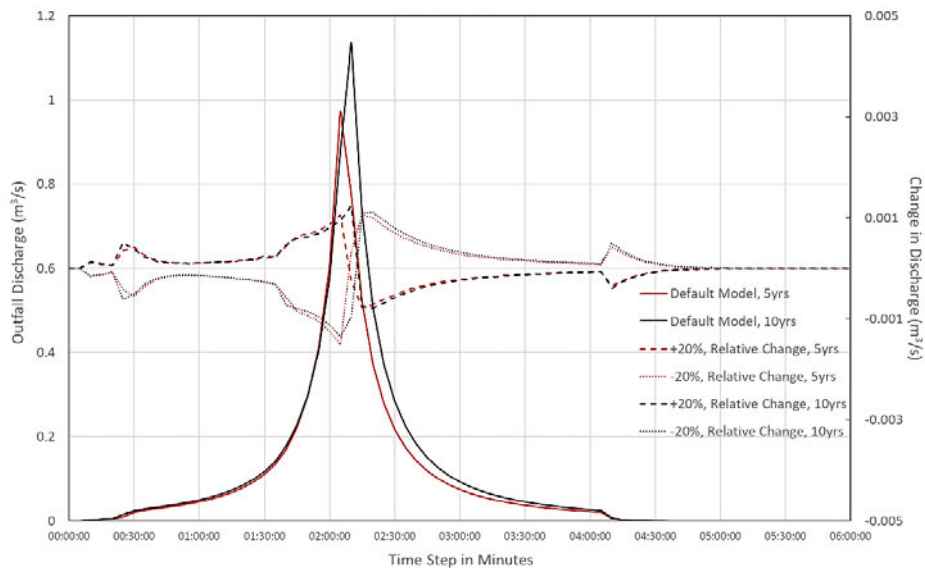


Figure 42: Change in Model Discharge Hydrographs (%Slope)

5.7.2.4 Manning's N for Overland flow Parameter (N_{perv}/N_{imperv})

The output hydrographs of the parametrically varied models for the ManningsN parameter were computed for storm events with a return period of 5 years and 10 years and plotted in a graph as illustrated in *Figure 43*. Due to its low sensitivity, no discernible change was observed between the discharge profile of the catchment across both the storm events for the alterations of the parameter. Nevertheless, since this study was conducted for the purposes of examining the comprehensive effects of the parameter on model results, the relative change in outfall discharge at each time step was computed and plotted at a reasonable scale to investigate the influence of the parameter on the catchments discharge profile.

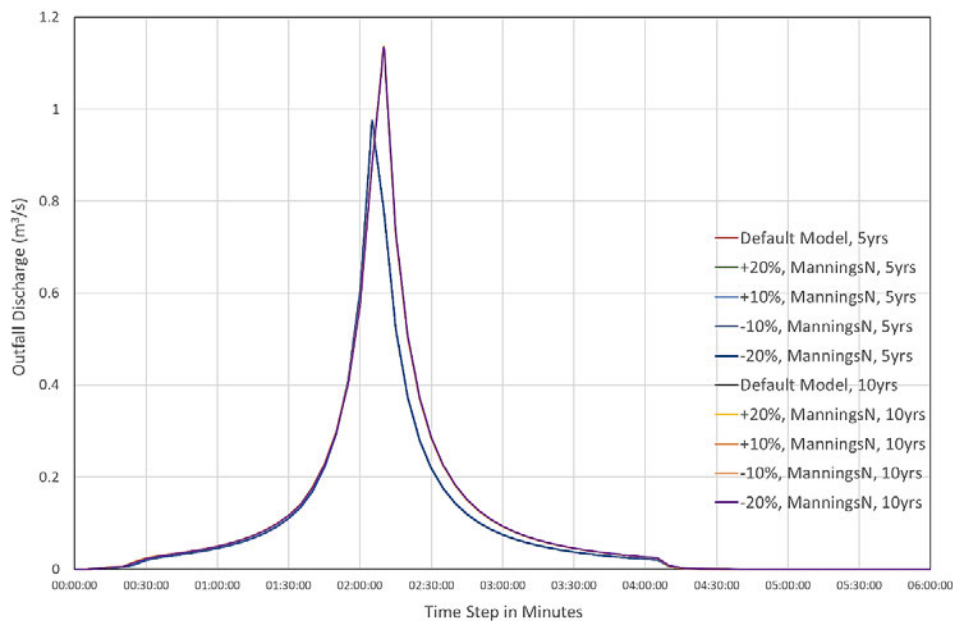


Figure 43: Model Hydrographs (ManningsN)

Figure 44 depicts the change in catchment discharge resulting from different permutations of the ManningsN parameter. From the figure, a “narrowing” effect of the hydrographs peak was illustrated by the positive shift in discharge magnitude on the rising limb of the hydrograph and a negative shift in discharge magnitude on the falling limb of the hydrograph when the ManningsN parameter was incrementally varied from default values. On the contrary, when the ManningsN parameter was reduced, a “widening” effect of the hydrographs peak was observed, where the gradient of discharge magnitudes on the rising limb and falling limb of the catchment’s hydrograph were dampened. Similar to the Width and %Slope parameter, the ManningsN parameter was observed to have a greater impact on the catchments discharge profile for less intense storms.

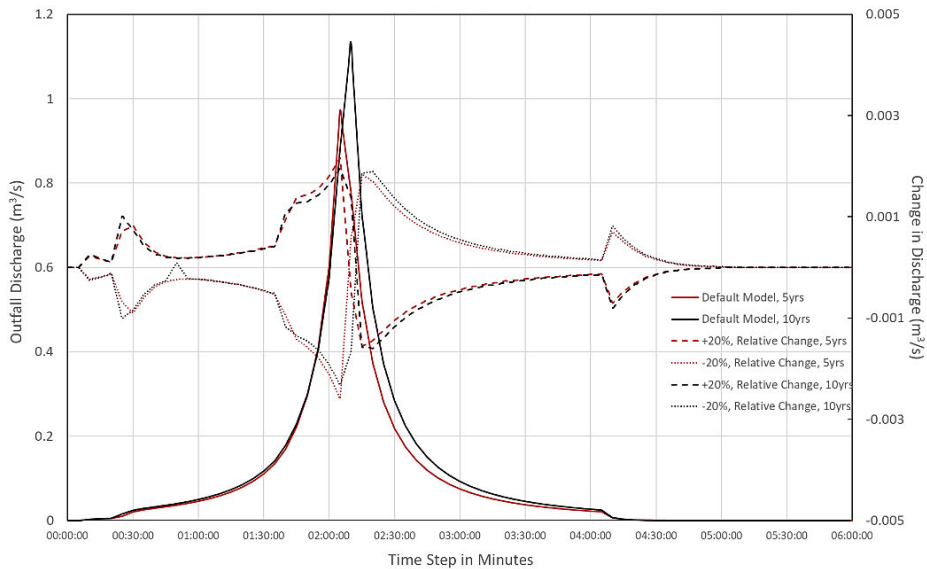


Figure 44: Change in Model Discharge Hydrographs (ManningsN)

5.7.2.5 Percent Imperviousness Parameter (%Impervious)

The output hydrographs of the parametrically varied models for the %Impervious parameter were computed for storm events with a return period of 5 years and 10 years and plotted in a graph as illustrated in *Figure 45*. As observed from the figure, alterations made to the %Impervious parameter considerably impacted the discharge profile of the catchment across both the storm events. When the model results are jointly plotted together, significant divergence from the default model's hydrograph was observed between the start and the peak of the hydrograph. However, following the peak of the hydrograph, discharge profiles for all models irrespective of %Impervious variation were found to converge and fit the hydrograph computed from the default model.

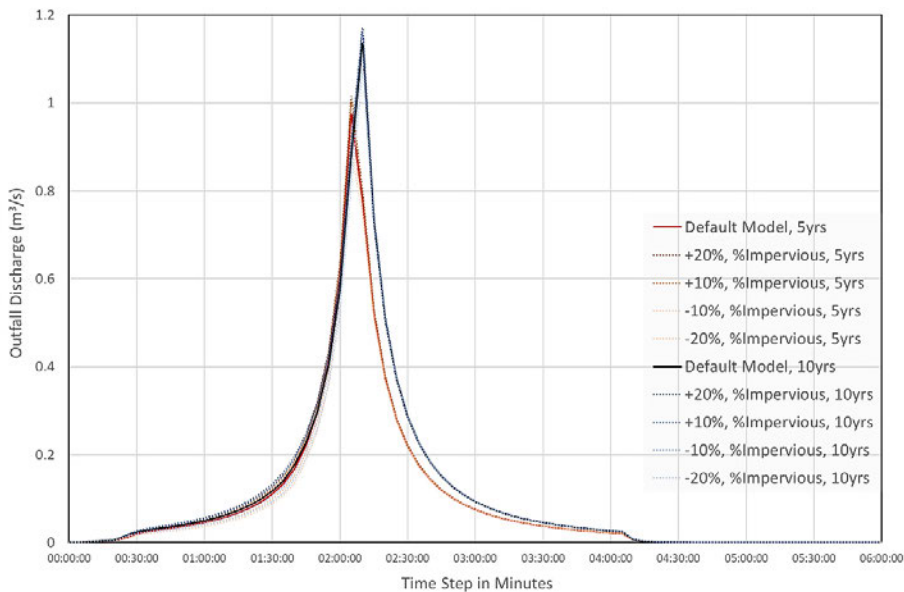


Figure 45: Model Hydrographs (%Impervious)

To provide a better representation of the effects observed from varying the %Impervious parameter, a separate graph was plotted by computing the relative change in outfall discharge at each time step (*Figure 38*). As shown in the figure below, the increase and decrease of the %Impervious parameter influenced discharge magnitudes of the catchment model to trend towards the same direction. Additionally, changes in discharge magnitudes were observed to primarily concentrate between the start and peak of the hydrograph. Relative change to discharge magnitudes were also observed to progressively rise/ fall until the peak change is reached before sharply declining/ converging to a magnitude of zero.

Due to the observed impacts resulting from this parametric study, the %Impervious parameter was deemed to have a dampening/intensifying effect on the gradient of the discharge hydrograph of the catchment, primarily affecting the gradient of the rising limb in the hydrograph. Additionally, the %Impervious parameter was observed to have a greater impact on the catchments discharge profile for less intense storms. It is important to note that the unequal change in discharge magnitude between the increase or decrease of the %Impervious parameter is not due to trends underlying the parameter. Instead, the irregularity was attributed to several sub-catchments reaching the absolute limit of the %Impervious parameter (100%) before the full 20% increase/change can be realized.

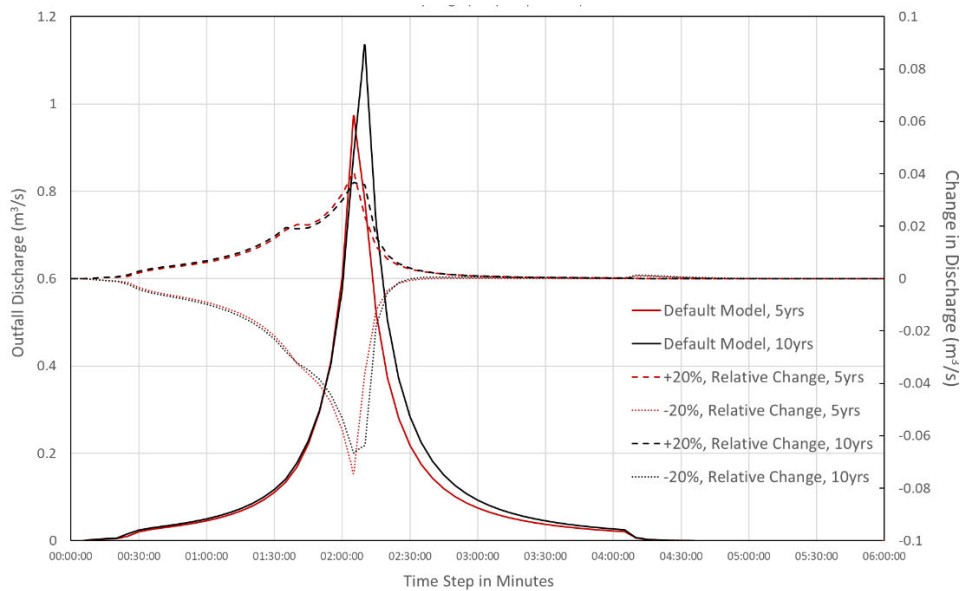


Figure 46: Change in Model Discharge Hydrographs (%Impervious)

5.7.2.4 Curve Number Parameter (CN)

The output hydrographs of the parametrically varied models for the CN parameter were computed for storm events with a return period of 5 years and 10 years and plotted in a graph as illustrated in *Figure 37*. As observed from the figure, the alteration of the CN parameter slightly impacted the discharge profile of the catchment, contributing to marginal changes in peak discharge magnitude and shape of the rising limb in the hydrograph.

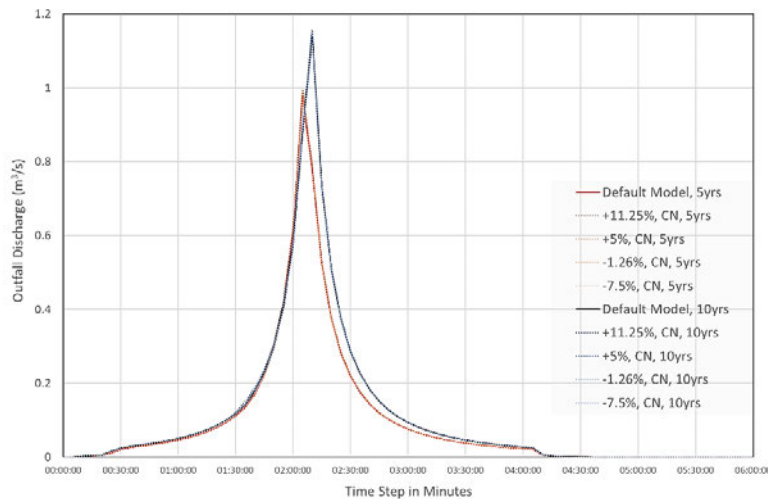


Figure 47: Model Hydrographs (CN)

Since the impacts of the CN parameter are difficult to perceive from the figure depicting the entire discharge profile of the catchment, another graph was plotted by utilizing the relative change in discharge to investigate the influence of the parameter on the catchment's hydrograph (*Figure 48*). Illustrated in the figure below, a positive shift in discharge magnitude was observed when the CN parameter was increased from default values. Similarly, a negative shift in discharge magnitude was observed when the CN parameter was decreased relative to default values. The magnitude of change observed in the discharge profile sharply increased near the onset of the rising limb, and peaks when the peak discharge rate hydrograph is reached. Subsequently, the change in discharge gradually converges to a magnitude of zero as the hydrograph reaches its inflection point. Due to the observed impacts resulting from this parametric study, the CN parameter was deemed to have a small amplifying effect on the discharge hydrograph of the catchment, where the discharge profile of the model is scaled in a near-uniform manner. The observed change caused by the CN parameter was measured to be 1 order of magnitude larger than that of the Width, %Slope and ManningsN parameter.

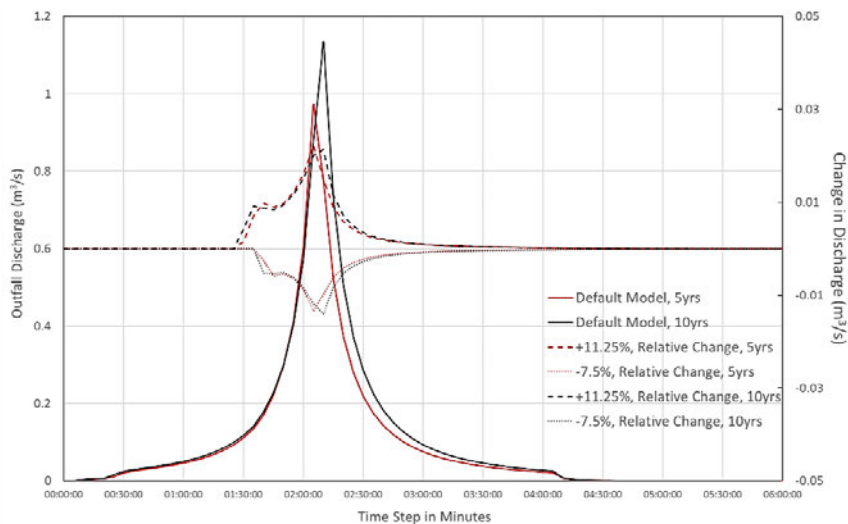


Figure 48: Change in Model Discharge Hydrographs (CN)

6.0 Probabilistic Life Cycle Cost Assessment (LCCA) Model

This chapter aims to provide an overview to the development of an automatic cost estimation methodology based on historical project costs. It first presents the factors that led to the selection of an appropriate probability density function (PDF) before describing the functional variables that characterize the shape and scale of the probability distribution. Subsequently, the two computational methodologies for fitting the model distribution to historical cost data were reviewed and iteratively tested to discover a better approach to modelling distributions of cost data. Finally, an Application Programming Interface (API) subroutine was developed with the xlwings python package to facilitate the interaction of the cost estimating system with an excel spreadsheet containing the life cycle cost financial model.

For clarity, this chapter is the preamble to **step three of the feasibility framework** (Performance Evaluation) and describes the investigation and development of a computational model used to conduct the LCC/NPV/IRR evaluation.

6.1 Introduction

Project cost estimation plays an integral role when performing financial risk assessments throughout all stages of a project ranging from pre-project planning to construction. However, conventional cost estimation techniques are often based on a deterministic approach and cannot accurately reflect the inherent variability observed in the real world (Curran, 1989).

A prevalent example of the deterministic approach used within many segments of the industry includes the development of a single point estimate and applying a contingency factor typically as a percentage of the base cost to artificially inflate the estimation due to project-related risk and uncertainty. Although this contingency factor is typically determined by experts who take into account specific project and economic circumstances, deterministic methods are still unable to provide a formal and comprehensive risk analysis of the cost variables and thus cannot provide a confidence interval specifying the adequacy of the estimated total costs. To overcome the shortcomings of a deterministic approach, techniques such as range estimation have grown to become a recognized and adopted methodology in the field of cost engineering. When employing the range estimation method, random variables are used to define the cost elements instead of known parameters, and as a result, total project costs can be expressed as a probability distribution as opposed to a point estimate produced by adopting deterministic methods.

The resulting probability distribution of total cost then allows the user to present cost estimates associated with specific levels of confidence, thereby enabling the quantification of exposure to financial risk (Back et al, 2000). These attributes of the range estimation method stand to be enormously useful to the financial estimator when preparing comprehensive financial evaluations and overseeing the deployment of financial resources during the implementation of a project.

The most prevalent methodology for performing range cost estimates involves employing probabilistic techniques such as Monte Carlo simulations to compute the full spectrum of probable total cost estimates for a project. In the Monte Carlo simulation, individual cost elements in a financial model are each defined as random parameters sampled from a defined/known probability distribution. The financial model is then simulated iteratively with each iteration representing a single probabilistic scenario. In practice, the sampling and simulation process of the financial model is usually repeated thousands of times to generate a probability distribution of the total project costs, and in doing so incorporates the inherent variability in components costs as well as enables a level of confidence to be assigned to the distribution of final results.

6.2 Probability Density Functions (PDF)

The selection of probability density functions to represent historical cost information is a crucial consideration in the development of cost estimation systems. As mentioned in a paper by Back et al (2000), PDFs selected for probabilistic cost modelling should demonstrate similar characteristics to the expected economic behaviour of the input cost parameters being modelled. Since there exist, several families of density functions with different qualities, important properties were defined to guide the selection of an appropriate PDF to represent the cost parameters being modelled.

1. In any cost estimate, lower and upper limits should exist. Where estimates that go beyond these limits are largely deemed irrational. To mimic this aspect of cost, the selected probability distribution function should have bounded ends.
2. Since it is irrational/ illogical to suppose that project costs components are discrete, the distribution function selected should be continuous to generate a representative probabilistic model for cost components.
3. The probability of occurrence is assumed to decline as the lower and upper limits of the distribution function are approached. This characteristic complements the anticipated economics of construction costs where there exists a most probable value. Due to this, the probability distribution is expected to be unimodal with a convex shape.
4. Finally, since actual costs for components typically tend towards higher values relative to the estimated mean and mode, the probability distribution function must permit the modelling of skewness.

As illustrated in *Table 16*, the properties of the lognormal, normal, gamma, uniform, beta, and triangular distributions were compared in relation to the aforementioned properties deemed desirable for the modelling of construction costs.

Table 16: Comparison of Probability Density Functions (Back et al, 2000)

Probability Distribution	Bounded	Desired Properties	
		Unimodal	Skewness
Lognormal	At one end	Yes	Yes
Normal	No	Yes	No
Gamma	At one end	Yes	Yes
Uniform	Yes	No	No
Beta	Yes	Depends	Yes
Triangular	Yes	Yes	Yes

As shown in the table above, the triangular and beta distributions were found to be the only families of probability distributions that comply with the aforementioned constraints defined in Chapter 6.2.

To select the more desirable distribution of the two, Back et al (2000) tested both the beta and triangular distributions on historical project cost datasets obtained from the Texas Department of Criminal Justice (TDCJ), and through various modelling and testing initiatives, found the triangular distribution to be more desirable. In the study, Back et al (2000) reports three main issues in employing the beta distribution for cost modelling.

The first and primary reason for selecting the triangular distribution revolves around the inconsistency in obtaining a unimodal n-shaped distribution when employing the beta distribution for many of the datasets provided by the TDCJ. This resulted in the modelled distribution consisting of two most-likely values for many of the datasets and goes against the previously defined economic characteristics anticipated in construction costs.

The second reason contributing to the selection of the triangular distribution stems from the added complexity of employing the beta distribution. In its general form, the beta distribution requires four shape parameters to be defined in order to form a representative distribution. Due to the larger number of variables, the general form may not be feasible/intuitive to employ in an automated cost estimating system. As an alternative, the beta distribution in its standard form only requires two shape parameters, but severely restricts the x parameters to a range between zero and one, creating a need to rescale and shift samples in the distribution to accommodate the full range of values in the underlying dataset.

The third reason/ downside of employing the beta distribution stems from the convoluted and unintuitive process of computing and defining the two shape parameters alpha (α) and beta (β), as opposed to the minimum, most likely and maximum values, deemed necessary for the triangular distribution. The most prevalent approach to defining the alpha (α) and beta (β) parameters, involves first determining the supposed parameters of the underlying triangular distribution, where an estimate for the minimum (a), most likely value (m), and maximum (b) is achieved by approximating the mean with the following equation:

$$\mu = \left(\frac{a + 4m + b}{6} \right) \quad (35)$$

It is important to note that Equation 29 is only valid under the assumption that the distribution is largely symmetrical or moderately skewed with a standard deviation equating to one-sixth of the total range of the dataset (Back et al, 2000). Subsequently, with the assumption that the population mean is not equal to the most likely value of the dataset, the two shape parameters alpha (α) and beta (β) can be approximated by means of Equations 30 and 31:

$$\alpha = \frac{(x - a)(2m - a - b)}{(m - x)(b - a)} \quad (36)$$

$$\beta = \frac{(b - x)}{(x - a)} \alpha \quad (37)$$

This convoluted process with multiple presumptions made to the dataset thereby limits the flexibility of employing the beta family of probability density functions and leads to a less intuitive understanding of the relationship between the shape factors and the range of values in the dataset. Due to these reasons, the family of triangular distribution functions was deemed to be more suitable for the automatic cost estimation system. In addition, several authors focused on the subject of cost estimation have either recommended the family of triangular distributions or recognized their prevalence in probabilistically modelling cost-related data (Ahmad 1992; Back et al, 2000; Curran, 1989; Knoke & Spitter, 1990; Mlakar & Bryant, 1992; Rowland & Curran, 1991).

6.3 Methods to Model Distribution of Cost Data

Most cost estimates using the triangular distribution assumes that experts and experienced estimators can effortlessly estimate the minimum, most likely, and maximum values (Back et al, 2000). However, in a 1995 study by Wing Chau, the validity of subjective determination or approximation of a triangular distribution for cost estimation purposes was investigated. The study concluded that the tradition of subjectively designating values from historic datasets as triangular distribution parameters resulted in higher biases in estimates. Additionally, the results of the study showed that the error introduced by the assumption of triangular distribution parameters was systematic and significant, leading to an upward bias of about 20% in general.

To overcome the limitations and dependence in estimating subjective values for the triangular distribution function, Back et al (2000) proposed the use of more robust statistical procedures such as the moment matching, maximum likelihood, and least-squares curve fitting methods to approximate (a), (b) and (m) values. These procedures would allow the automated generation of a PDF without the assistance of an expert or any other subjective evaluations when a finite quantity of historical data points is presented for analysis.

Figure 49 depicts the triangular distribution in its general form with parameters equivalent to the minimum (a), mode (m), and maximum (b) of the dataset to be modelled.

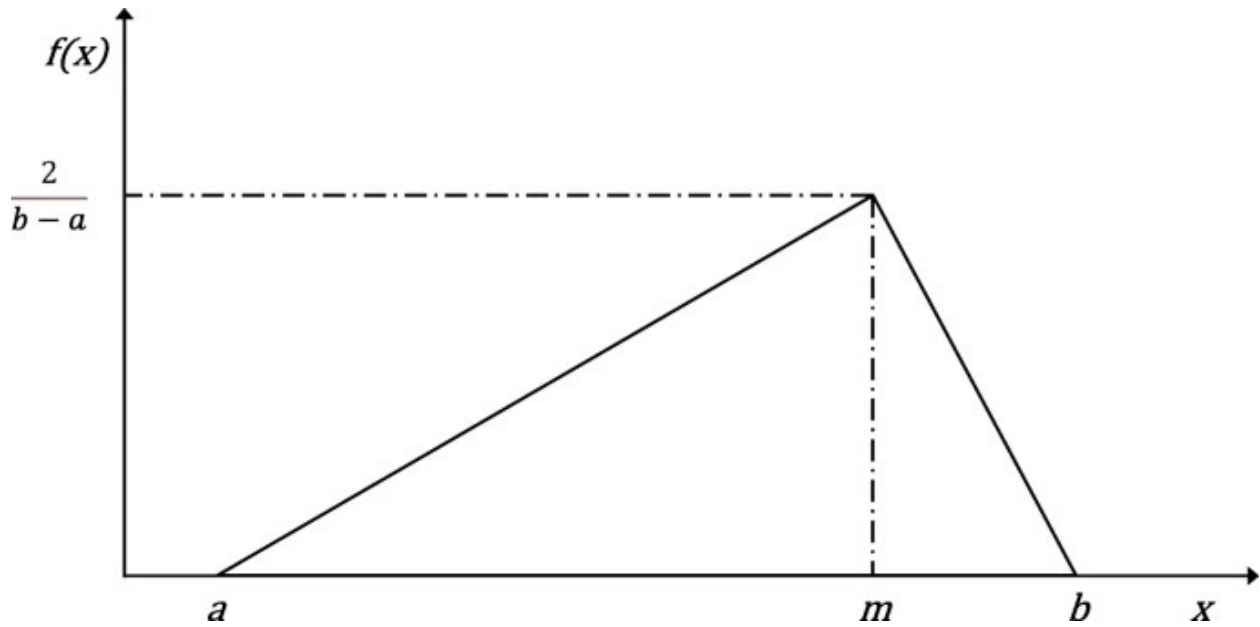


Figure 49: Triangular Density Function (Abraham & Punniyamoorthy, 2021)

Additionally, the formulaic representation of the triangular PDF observed in Figure 49 can also be defined as:

Where $a \leq x \leq m$

$$f(x) = \frac{2(x - a)}{(m - a)(b - a)} \quad (38)$$

Where $m \leq x \leq b$

$$f(x) = \frac{2(b - x)}{(m - a)(b - a)} \quad (39)$$

As reported by Back et al (2000), the most prevalent approaches to estimating the parameters of PDFs involves the use of maximum likelihood estimation, moment matching, or the method of least squares to fit the theoretical cumulative distribution function (CDF) to a known CDF of the dataset. These approaches were employed by Back et al (2000) for fitting triangular distributions as well as AbouRizk et al (1994) to fit beta distributions to historic datasets.

The results obtained by both AbouRizk et al (1994) and Back et al (2000) revealed that the least-squares method generally yielded equal or better results when compared to either the moment matching method or the method of maximum likelihood. For context, AbouRizk et al (1994) performed the comparative analysis of the methods using a visual-based assessment of the quality of fit whereas Back et al (2000) computed the average error of estimated parameters and employed statistical means such as the Analysis of Variance (ANOVA) test as well as pairwise

comparison of the methods using a test for the least significant differences (LSD) to perform the comparative analysis.

Due to their findings, the least-squares methodology was adopted to automatically fit the triangular PDF to the historic data points available for analysis. The following section describes in detail the procedures used in this study.

6.4 Non-Linear Least Squares Minimization Algorithms

As mentioned previously, the least-squares methodology was employed to fit the cumulative distribution function of the triangular PDF to historical data points. Given that the triangular distribution is composed of two segments of straight lines connected at the mode, the CDF can also be represented by two parabolical arcs connected at the mode (Back et al, 2000). Assuming that $L(x)$ represents the left segment of the CDF arc between “ a ” and “ m ”, and $R(x)$ represents the right segment of the CDF arc between “ m ” and “ b ”, the polynomial representation of the arc lengths can be expressed as:

$$L(x) = L_1x^2 + L_2x + L_3 \quad (40)$$

and

$$R(x) = R_1x^2 + R_2x + R_3 \quad (41)$$

Where L_1, L_2, L_3, R_1, R_2 , and R_3 are constants.

Figure 50 depicts the relationship between the probability density function in Figure 49 and the polynomial representation of the CDF defined above (Equations 34 & 35). According to Back et al (2000), as well as the first principles of statistics, if the CDF is examined analytically, the following boundary conditions must exist:

$$L(a) = 0; \quad L'(a) = 0; \quad L(m) = R(m); \quad L'(m) = R'(m); \quad L(b) = 1.0; \quad R'(b) = 0;$$

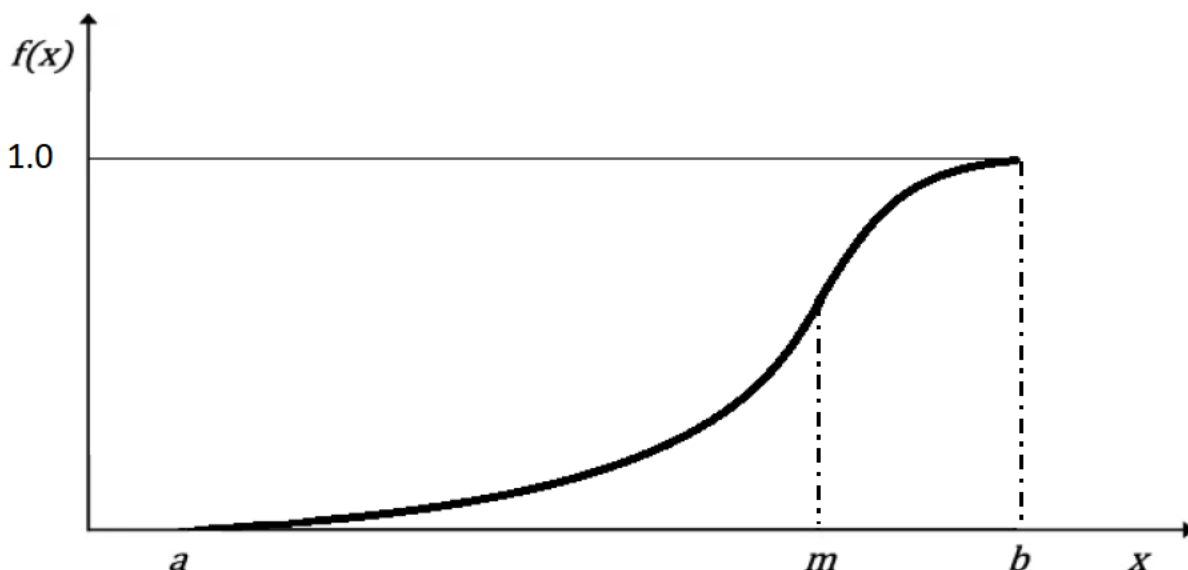


Figure 50: CDF for a Triangular distribution, expressed by $L(x)$ and $R(x)$ unified at mode “ m ”

To derive the expressions necessary to implement the least-squares methodology for the triangular distribution, one of the underlying equations for the triangular distribution (Equation 36) was used:

$$\mu = \frac{a + m + b}{3} \quad (42)$$

Where μ is the mean of the density function, with a , b , and m being the lower bound, the upper bound, and the mode of the density function.

By considering the above-mentioned boundary conditions as numerical constraints and imposing an additional control where the mean of the triangular distribution (μ) is equal to the mean of the data set (\bar{x}), Back et al (2000) derived the general form representation of the coefficients in equations 36 and 37:

$$L_3 = \frac{a^2}{(b - a)(3\bar{x} - 2a - 2b)} \quad (43)$$

$$R_3 = 1 + \frac{b^2}{(a - b)(a + 2b - 3\bar{x})} \quad (44)$$

$$L_2 = \frac{2a}{(b - a)(2a + b - 3\bar{x})} \quad (45)$$

$$R_2 = \frac{2b}{(b - a)(a + 2b - 3\bar{x})} \quad (46)$$

$$L_1 = \frac{1}{(b - a)(3\bar{x} - 2a - b)} \quad (47)$$

$$R_1 = \frac{1}{(b - a)(3\bar{x} - a - 2b)} \quad (48)$$

As a result, Equation 34 representing the left segment [$a \leq x \leq m$] of the CDF parabola for the triangular distribution can be rewritten as:

$$L(x) = \frac{(x - a)^2}{(b - a)(3\bar{x} - 2a - b)} \quad (49)$$

while Equation 35 for the right segment [$m \leq x \leq b$] of the CDF parabola can be likewise re-expressed as:

$$R(x) = \frac{a^2 + ab - b^2 - 2bx + x^2 - 3a\bar{x} + 3b\bar{x}}{(b - a)(3\bar{x} - a - 2b)} \quad (50)$$

By iteratively adjusting the values for “ a ” and “ b ” in the non-linear equations above (Equations 43 and 44), an approximation of the parameters for the hypothetical probability distribution can be obtained for the historical data by employing a regression-based technique to minimize the

difference in squares between the CDF derived from the historical data points and the theoretical curve (Back et al., 2000).

For this study, the author was able to identify two optimization algorithms namely the Levenberg-Marquardt algorithm and the Trust Region Reflective algorithm to minimize the differences in squares between the CDF derived from the historical data points and the theoretical best fit curve. Although both the Levenberg-Marquardt and Trust Region Reflective algorithms are Newton Step-based methods (“Restricted Newton Step methods”) (Berghen, 2004), when the initial approximation for the multivariate polynomial function is far from the actual solution, inherent differences between the two algorithms result in differing speeds of convergence as well as differing accuracy in optimized results.

Due to this, the trial procedure developed by Back et al. (2000) was used in this study to determine if the Levenberg-Marquardt optimization algorithm produced better results than the Trust Region Reflective algorithms. The following section details the procedure used to perform the comparative analysis/ trial of the algorithms.

6.5 Trial Methodology

To perform the trial, the test procedure developed by Back et al. (2000) was reconstructed in this study to analytically determine the more precise optimization algorithm of the two. The test consists of a collection of 44 predetermined triangular density functions (*Table 17*), from which a set of 100 values will be randomly drawn from each density function.

The set of 100 values then formed the test dataset and the CDF expressed by equations 43 and 44 was fitted using each of the two algorithms to determine the accuracy in estimating the parameters of the underlying distribution. The PyCharm Edu program, a Python Integrated Development Environment (IDE), was used to accomplish the analysis combined with functions in the python standard library as well several other libraries namely, pandas, NumPy, matplotlib, lmfit, and scipy. It should be noted that the sample size of 100 values was selected for this study on the basis of the author’s judgement on what would be a reasonable/attainable quantity for an organization like HDB to collect.

Sets of 10, 30, 50 and 100 trials were performed for each of the 44 triangular distributions, and because the optimization algorithms require an initial estimate of the trial value, the minimum random value obtained from the sampled dataset was assumed to be the “a” parameter while “b” was the maximum random value obtained. “m” was encrypted within the python code as a mathematical constraint derived from equation 36 and expressed as:

$$m = 3\mu - a - b \quad (51)$$

Where μ is the mean of the density function, and a , b , and m are the lower bound, the upper bound, and the mode of the density function respectively.

Table 17: Triangular Distribution Data (Back et al, 2000)

Forty-Four Triangular Distribution Data used for average error tabulation (a,m,b)								
Set 1	Set 2	Set 3	Set 4	Set 5	Set 6	Set 7	Set 8	Set 9
5, 5, 10	5, 10, 10	-	-	-	-	-	-	-
5, 5, 15	5, 10, 15	5, 15, 15	-	-	-	-	-	-
5, 5, 20	5, 10, 20	5, 15, 20	5, 20, 20	-	-	-	-	-
5, 5, 25	5, 10, 25	5, 15, 25	5, 20, 25	5, 25, 25	-	-	-	-
5, 5, 30	5, 10, 30	5, 15, 30	5, 20, 30	5, 25, 30	5, 30, 30	-	-	-
5, 5, 35	5, 10, 35	5, 15, 35	5, 20, 35	5, 25, 35	5, 30, 35	5, 35, 35	-	-
5, 5, 40	5, 10, 40	5, 15, 40	5, 20, 40	5, 25, 40	5, 30, 40	5, 35, 40	5, 40, 40	-
5, 5, 45	5, 10, 45	5, 15, 45	5, 20, 45	5, 25, 45	5, 30, 45	5, 35, 45	5, 40, 45	5, 45, 45

6.6 Analysis of Results

The test procedure consisted of producing a random set of 100 values for each of the defined 44 triangular density functions. Utilizing the 100 values generated as a starting point, a new triangular distribution was defined using each of the optimization algorithms to estimate the distribution parameters. On the presumption that the optimization algorithms are effective in modelling the data correctly, estimated parameters are expected to be reasonably consistent with the known parameters.

Every time a new triangular distribution is defined using each of the optimization algorithms, a new set of 100 random samples will be generated from the originally defined triangular density function. This procedure was repeated in a set of 10, 30, 50 and 100 times for each of the 44 triangular density functions developed for the analysis. It is worth noting that the 44 triangles (Table 17) defined by Back et al (2000) were constructed with the aim of providing a comprehensive range of forms for the triangular distribution, systematically varying from an exceedingly skewed form with a leftward bias to an exceedingly skewed form with a rightward bias.

This procedure eventually produced 440, 1320, 2200 and 4400 estimated triangular-density functions for each optimization algorithm, consisting of 10, 30, 50 or 100 approximations for every one of the 44 predefined triangular distributions summarized in *Table 17*. Since each of the newly generated triangular distributions had a new approximation for the (a), (b) and (m) parameters, the newly generated parameters were examined against the “known” parameters of the original triangular distribution. As a result of the study, the average absolute error between the estimated and original parameters of the triangular distribution was computed.

Figure 51 depicts the average absolute error computed from running the above-mentioned simulations of the trial procedure and attempts to evaluate the accuracy of the optimization algorithm across an increasing number of simulations.

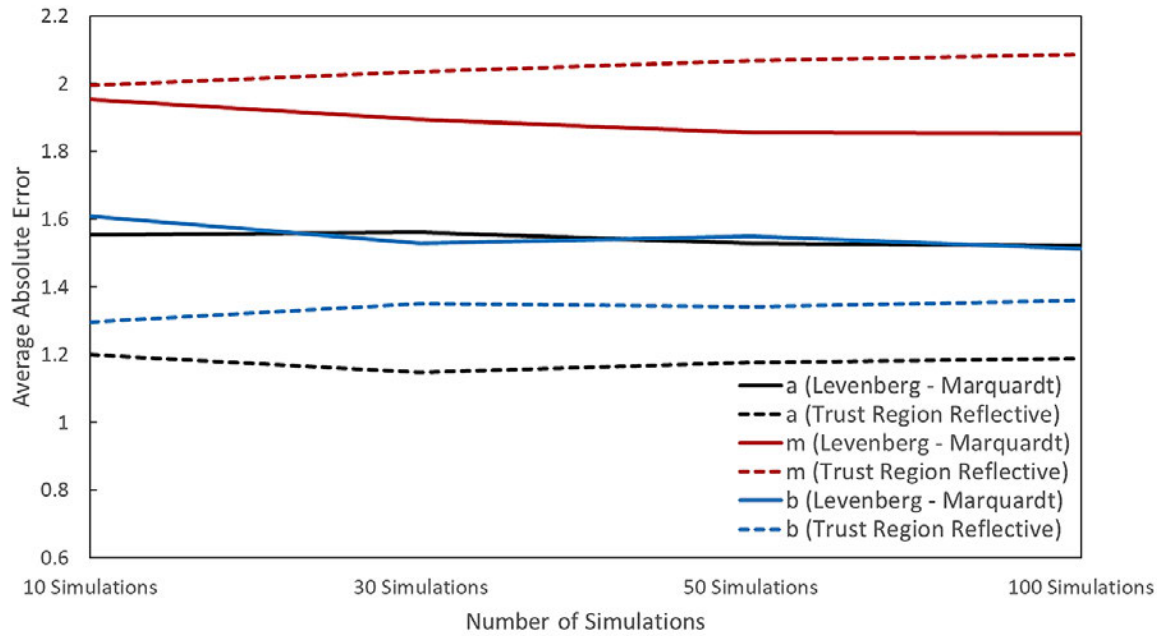


Figure 51: Convergence of Average Absolute Error between Levenberg - Marquardt and Trust Region Reflective

As indicated in the figure, the Levenberg-Marquardt optimization algorithm (LM) generally produced a higher average absolute error than the Trust Region Reflective algorithm (TRR). Although no definitive convergence of absolute average error between the two optimization algorithms was observed with increasing simulations, the TRR algorithm exhibited marginally greater fluctuations in average absolute errors as the number of simulations varied.

Figure 52 summarizes the overall average absolute error computed from the results depicted in Figure 51 for both optimization algorithms.

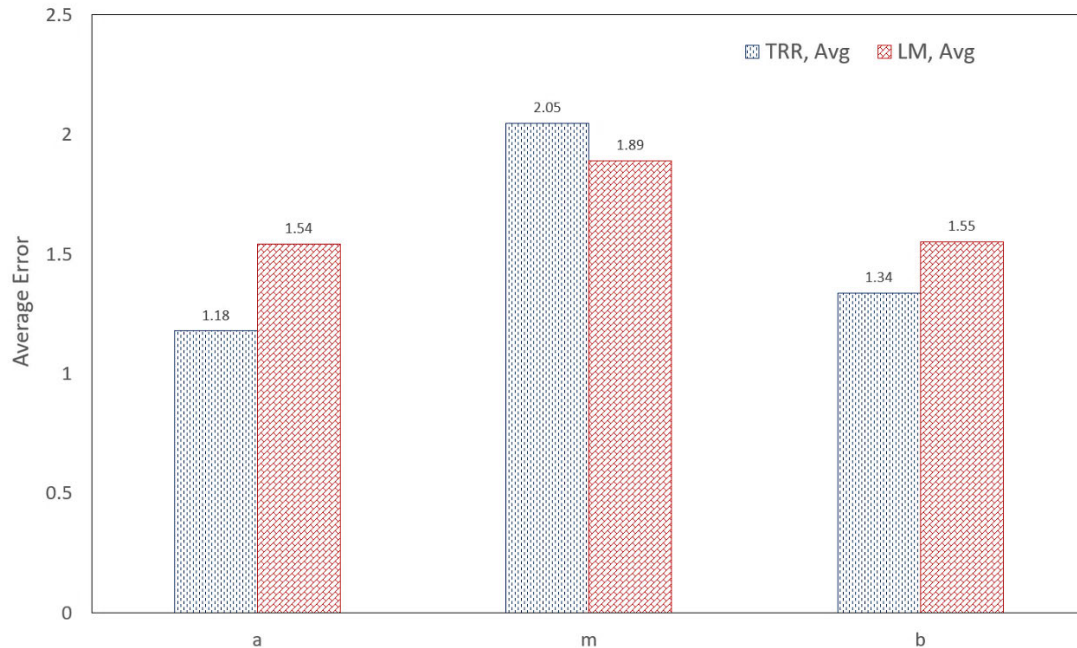


Figure 52: Overall Average Absolute Error

As illustrated in *Figure 52*, the TRR algorithm generated the most accurate estimates for the known parameters of (*a*) and (*b*) when evaluated in comparison to the LM algorithm. The average absolute error for the estimated (*a*), (*m*) and (*b*) parameters were 1.18, 2.05, and 1.34 respectively for the TRR algorithm, as opposed to the values 1.54, 1.89, and 1.55 respectively for the LM algorithm.

The disparity in accuracy was also observed when conducting the trial procedure with the LM algorithm. When the optimization/ "exploratory search" function was executed within the parameter space for all 3 parameters of the triangular distribution, the LM algorithm was not able to reliably converge. This may be due to the small step size used during the iterative "search" phase of the LM algorithm, and the ensuing omission of parameters deemed to be insignificant to the non-linear minimization function developed in python.

The non-linearity of the function also introduces additional issues since the sensitivity of all 3 parameters may not be constant within the parameter space being explored. As a result, although the LM method is "faster" when compared to the TRR method empirically, the algorithm may prematurely stop the iterative exploration of a parameter space when the local minima of the minimization function is reached. Consequently, the trust-region reflective method generated better results for (*a*) and (*b*) parameter estimations and demonstrated better stability/ more consistent results across the number of simulations ran.

6.6.1 Analysis of Optimization Algorithms for Skewed Triangular Distributions

To further investigate the capabilities of the LM and TRR algorithms for non-linear least-squares minimization of the triangular distribution, subgroups of the previously defined triangular distributions were categorized for the study. The subgroups were categorized into 5 categories consisting of extremely skewed distributions [positive (right) & negative (left)], moderately skewed distributions [positive (right) & negative (left)] as well as symmetrical distributions. The five subsets/ categories used for this study are summarized in *Table 18*.

Table 18: Triangular Distribution Data based on Skewness (*a,m,b*)

Set 1 Extreme Positive	Set 2 Extreme Negative	Set 3 Symmetry	Set 4 Moderate Positive			Set 5 Moderate Negative		
			-	-	-	-	-	-
5, 5, 10	5, 10, 10	-	-	-	-	-	-	-
5, 5, 15	5, 15, 15	5, 10, 15	-	-	-	-	-	-
5, 5, 20	5, 20, 20	-	5, 10, 20	-	-	5, 15, 20	-	-
5, 5, 25	5, 25, 25	5, 15, 25	5, 10, 25	5, 15, 30	-	5, 20, 25	-	-
5, 5, 30	5, 30, 30	-	5, 10, 30	5, 15, 35	-	5, 25, 30	5, 20, 30	-
5, 5, 35	5, 35, 35	5, 20, 35	5, 10, 35	5, 15, 40	-	5, 30, 35	5, 25, 35	-
5, 5, 40	5, 40, 40	-	5, 10, 40	5, 15, 45	5, 20, 40	5, 35, 40	5, 30, 40	5, 25, 40
5, 5, 45	5, 45, 45	5, 25, 45	5, 10, 45	5, 15, 30	5, 20, 45	5, 40, 45	5, 35, 45	5, 30, 45

The same test was performed for the five subsets of the triangular distribution summarized in *Table 18* using the same procedure as the previously mentioned trial. After 10, 30, 50 and 100 test fits were completed by each of the optimization algorithms, where each fit was constructed from 100 random samples of a defined distribution (*Table 18*), the absolute error for the (a), (m) and (b) parameters was computed. Absolute errors in this instance are defined as absolute values of differences between the estimated and known parameters.

Figure 53 summarizes the analysis results in relation to the extremely skewed, positive (right) triangular distribution. For this subset defined as the extremely skewed negative distribution, the parameter (m) is equivalent to parameter (a), forming a right-angled triangular distribution.

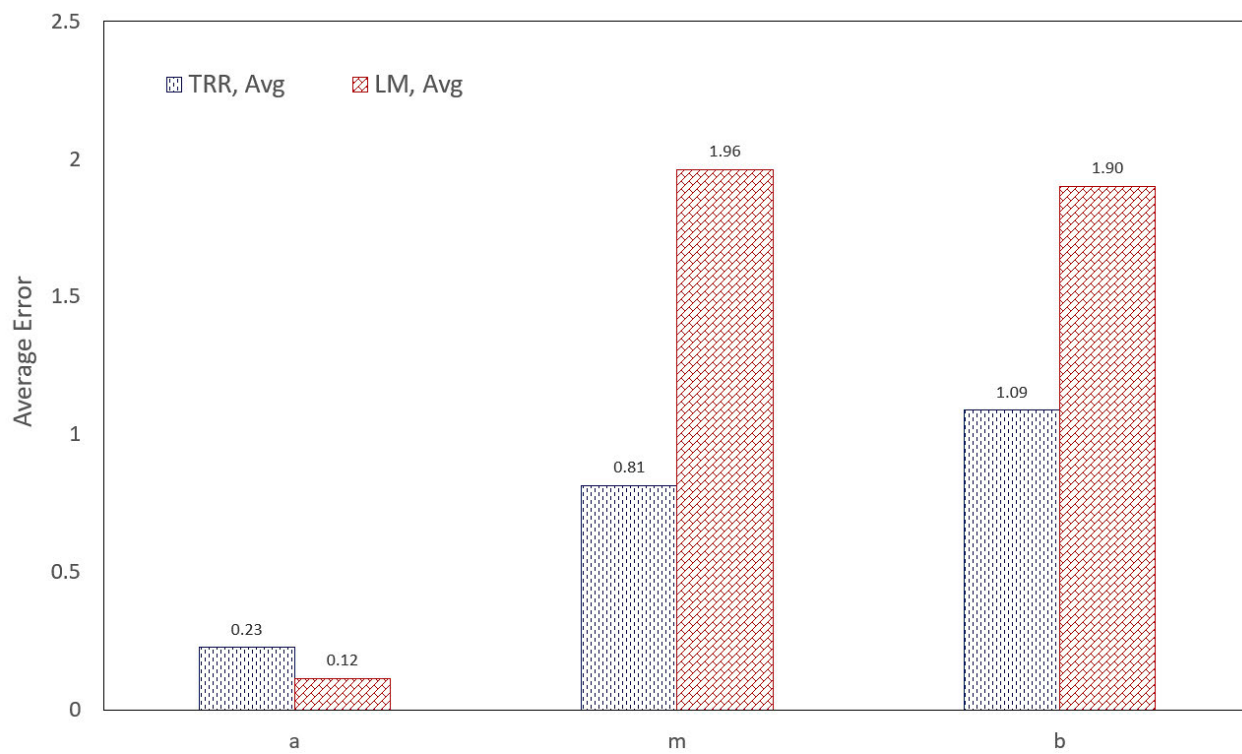


Figure 53: Average Absolute Error, Extremely Skewed (Right)

As shown in the figure, the LM algorithm appears to have relatively low performance in estimating parameters (m) and (b) when compared to the TRR algorithm. Diametrically opposite to the results for the (m) and (b) parameters, however, the (a) parameter estimates were more accurate and generally better than the TRR algorithm employed.

A similar trend was observed when analysing the results acquired from the moderately skewed, positive (right) triangular distribution (*Figure 54*). As illustrated in the figure, the TRR algorithm seemed to perform significantly better than the LM algorithm, yielding an average absolute error of 0.72, 1.27, and 1.30 for the (a), (m) and (b) parameters respectively as opposed to 0.94, 1.98, and 2.25 generated from the LM algorithm. These results provide the empirical evidence to substantiate and employ the TRR algorithm in events where the sample distribution is observed to skew towards the left.

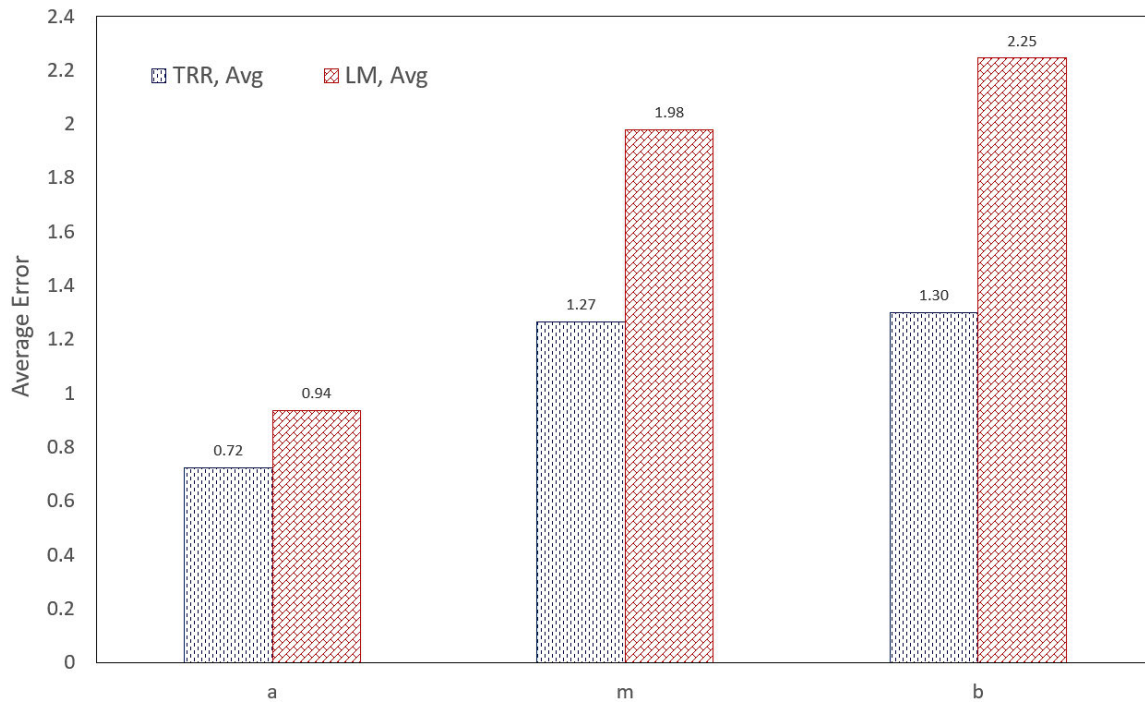


Figure 54: Average Absolute Error, Moderately Skewed (Right)

As presented in *Figure 55*, the analysis results obtained from the extremely skewed, negative (left) triangular distribution, where the (m) parameter is equivalent to the (b) parameter, depict the TRR algorithm performing a better job in estimating the parameter (a). On the contrary, the LM algorithm was observed to significantly outperform the TRR algorithm for both parameters (m) and (b), in terms of accuracy.

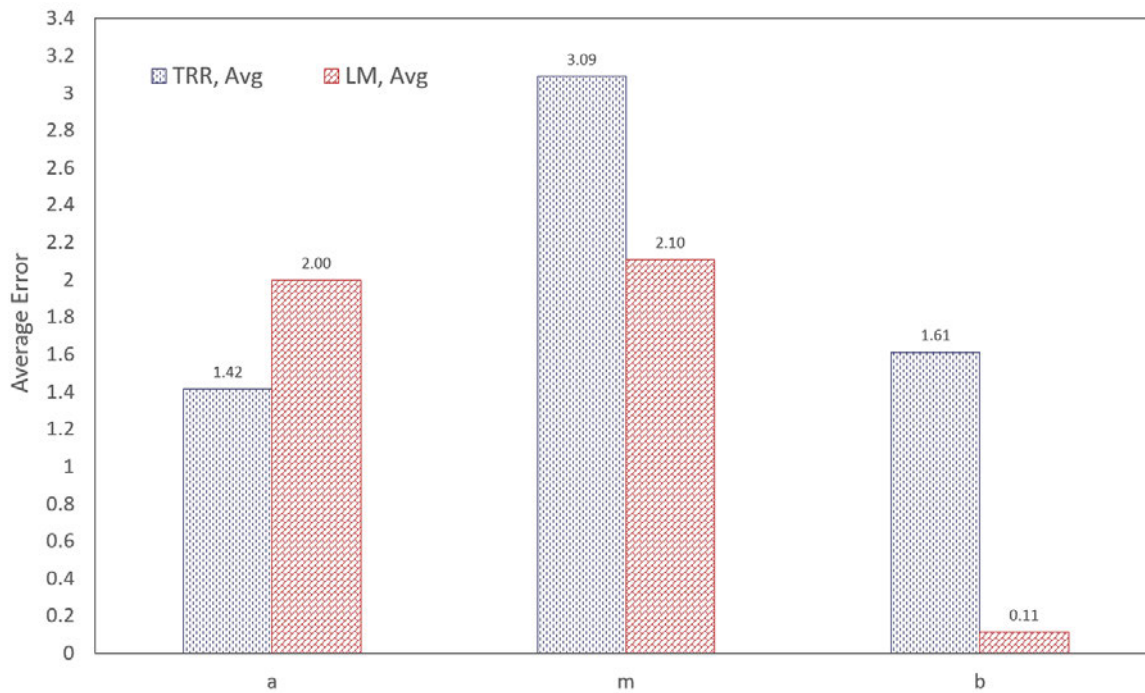


Figure 55: Average Absolute Error, Extremely Skewed (Left)

A marginally similar trend was observed when analysing the results obtained from the moderately skewed, negative (left) triangular distribution (*Figure 56*).

As shown in the figure, the TRR algorithm appears to have performed slightly better than the LM algorithm, reporting an average absolute error of 1.79, 2.67, and 1.33 as opposed to 2.38, 1.90, and 1.35 for the estimated (a), (m) and (b) parameters reported by the LM algorithm.

Although the TRR algorithm produced more accurate estimates for the (a) and (b) parameters, the disparity in average absolute error computed for (m) was significantly greater than the improvements gained from both the (a) and (b) parameters combined (0.77 vs 0.61). Nevertheless, it was decided that the TRR algorithm was more suitable for modelling moderately skewed negative (left) triangular distributions since the lower bound (a) and upper bound (b) of the fitted distribution hold greater importance in creating a realistic PDF.

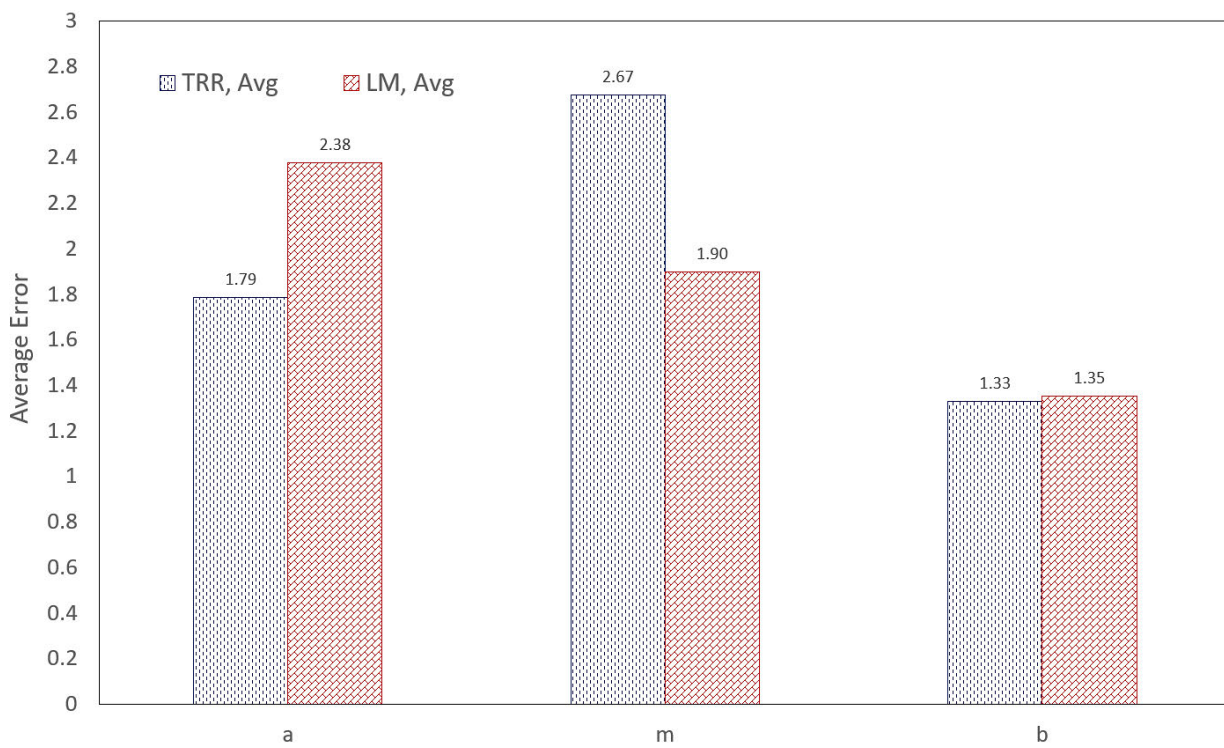


Figure 56: Average Absolute Error, Moderately Skewed (Left)

Lastly, *Figure 57* summarizes the analysis results generated from the tests conducted on the defined symmetrical triangular distributions. As illustrated in the figure, significantly better results were generated by the TRR algorithm, with a reported average absolute error of 1.18, 1.54, and 1.10 for the estimated (a), (m) and (b) parameters in comparison to the 1.55, 1.36, and 1.61 reported for the LM algorithm. These results help provide the empirical evidence to substantiate and employ the TRR algorithm in events where the sample distribution portrays symmetrical characteristics.

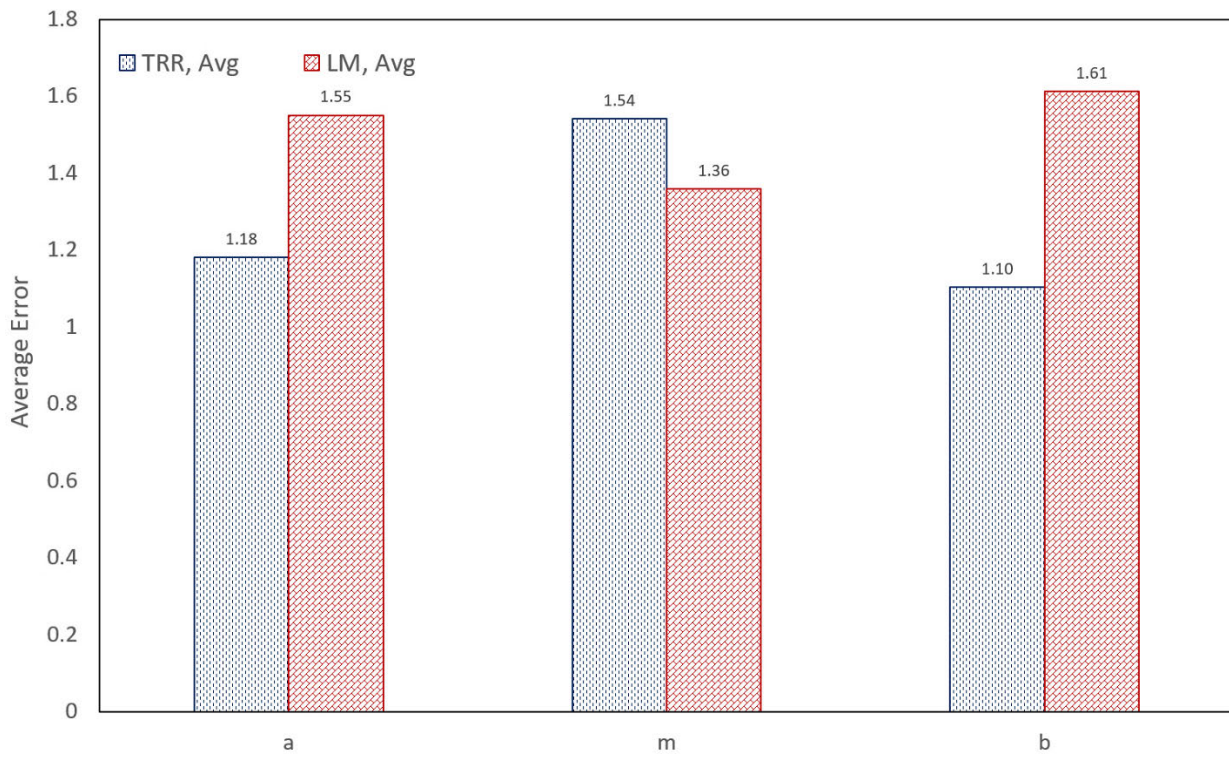


Figure 57: Average Absolute Error, Symmetrical

6.6.2 Optimization of Computational Structure for Least Squares Minimization

By executing the trials described above, the accuracy of both the TRR and LM optimization algorithm was investigated based on the skewness of the dataset being modelled. Through analysing the results obtained from the trials, the TRR algorithm was found to perform incrementally better in cases where the distribution of data points systematically varied from a moderately skewed, negative (left) triangular distribution to an extremely skewed, positive (right) triangular distribution. However, in sharp contrast to the previous observation, the LM algorithm was found to significantly outperform the TRR algorithm if the distribution of the data points exhibits similar characteristics to an extremely skewed, negative (left) triangular distribution.

Having established that the two optimization algorithms (LM & TRR) yielded a different average error depending on the skewness of the underlying dataset, it was important to incorporate both algorithms to create a more optimized computational structure for fitting PDFs to historic cost datasets. It was also important to identify trends in the performance of the newly developed computational structure and identify the optimal degree of skewness at which the algorithmic change occurs.

To develop and optimize the existing computational structure, it was necessary to first generate a quantifiable measure of skewness from the underlying dataset. Although there exists a number of different procedures to measure the skewness of a dataset, the Pearson's second coefficient

of skewness and the derived equation for the skewness (γ_1) in a triangular distribution (Weisstein, 2001) was selected for this study.

The Pearson's second coefficient of skewness can be computed using the following equation:

$$Sk_2 = \frac{3(\bar{x} - M_d)}{S_d} \quad (52)$$

Where Sk_2 is the Pearson's second coefficient, \bar{x} is the mean, M_d is the median and S_d is the standard deviation of the historical dataset.

While the derived equation for the skewness of a triangular distribution can be written as:

$$\gamma_1 = \frac{\sqrt{2}(a + b - 2m)(2a - b - m)(a - 2b + m)}{5(a^2 + b^2 + m^2 - ab - am - bm)^{3/2}} \quad (53)$$

Where γ_1 is the skewness coefficient of the dataset, a the lower bound of the distribution, b the upper bound of the distribution, and m the mode of the dataset. When Equation 47 is executed, it should be noted that the a , b , and m values used are identical to the assumed parameter estimates defined in Chapter 6.5.

For both Equations 46 and 47, a positive final result would imply that the analysed dataset had a positive (right) skewness. On the contrary, a negative final result would indicate that the dataset being analysed had a negative (left) skewness. Finally, if the final result equates to zero, the dataset is believed to have no skewness, and must therefore be symmetrical about the mode of the distribution. When dealing with a sample size of probabilistic data, there exists no exact/definite coefficient value capable of defining the form (skewness) of a distribution with full certainty. However, employing different methodologies for the computation of dataset skewness may lead to more reliable results.

To investigate the reliability of both Equations 46 and 47 in defining the skewness of the underlying dataset, a comparative analysis was performed using 44 sets of 100 samples, generated with the triangular distribution defined in *Table 18*. Both Equations 46 and 47 were employed to compute the skewness of the 44 random datasets and the reliability of the computed coefficient values relative to the original form of the distribution was investigated.

Figure 58 summarizes the results obtained from computing the skewness coefficient for 44 sets of 100 samples generated from the defined range of triangular distribution. The results are plotted systematically, ranging from the distributions with an extreme right skewness to distributions with an extreme left skewness.

As shown in the figure below, the Pearson's second coefficient approach (Equation 46) produced results with high variance across the 44 distributions. On multiple occasions, the method also produced conflicting results in relation to the original distribution used to generate the set of 100 samples (e.g.: Original distribution = Symmetrical but $Sk_2 > 0.4$). Comparatively, the derived

equation to compute the skewness of a triangular distribution (Equation 47) portrayed superior reliability in computed results, with little to no conflicting results in relation to the original distribution. Due to these findings, Equation 47 was chosen to quantitatively define the skewness of the underlying dataset.

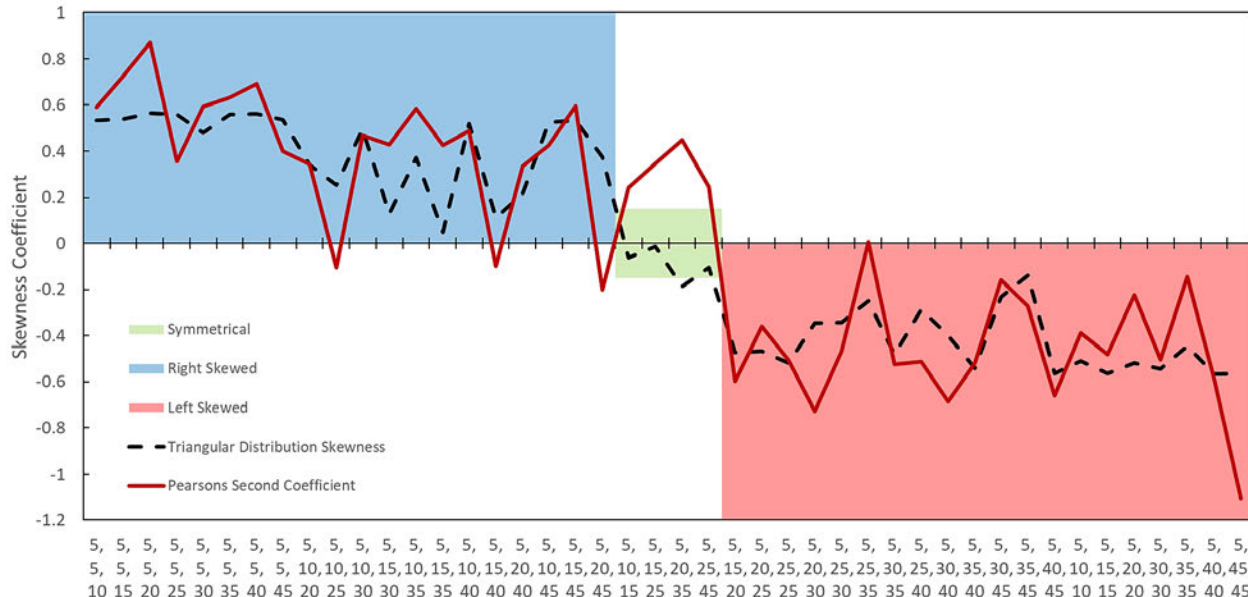


Figure 58: Comparative Analysis of Skewness Coefficient (a, m, b)

The previously computed results from Equation 47 were compiled and used to approximate a range of values (γ_1) based on the degree of skewness observed in the data set. *Table 19* illustrates the defined range in relation to the skewness of the dataset.

Table 19: Skewness Coefficient Range

Set 1 Extreme Positive	Set 2 Extreme Negative	Set 3 Symmetry	Set 4 Moderate Positive			Set 5 Moderate Negative		
			-	-	-	-	-	-
5, 5, 10	5, 10, 10	-	-	-	-	-	-	-
5, 5, 15	5, 15, 15	5, 10, 15	-	-	-	-	-	-
5, 5, 20	5, 20, 20	-	5, 10, 20	-	-	5, 15, 20	-	-
5, 5, 25	5, 25, 25	5, 15, 25	5, 10, 25	5, 15, 30	-	5, 20, 25	-	-
5, 5, 30	5, 30, 30	-	5, 10, 30	5, 15, 35	-	5, 25, 30	5, 20, 30	-
5, 5, 35	5, 35, 35	5, 20, 35	5, 10, 35	5, 15, 40	-	5, 30, 35	5, 25, 35	-
5, 5, 40	5, 40, 40	-	5, 10, 40	5, 15, 45	5, 20, 40	5, 35, 40	5, 30, 40	5, 25, 40
5, 5, 45	5, 45, 45	5, 25, 45	5, 10, 45	5, 15, 30	5, 20, 45	5, 40, 45	5, 35, 45	5, 30, 45
Skewness Coefficient (γ_1)								
> 0.4	< -0.4	-0.1 to 0.1	0.1 to 0.4			-0.1 to -0.4		

Table 19 was then used as a guide to optimize the computational structure of the least-squares minimization and to serve as a basis for validation. To perform the optimization, a trigger point for the algorithmic switch was developed through an if-else loop in python. An arbitrary variable (d_n) was defined, and in the event where $[y_1 < d_n]$, the LM algorithm would be the approach selected to perform the least-squares minimization. In contrast, if (y_1) is not less than (d_n) , the TRR algorithm would instead be adopted for the ensuing computation.

A comparative analysis between varying values of (d_n) was subsequently performed to ascertain the optimal trigger point at which the new computational structure would yield the lowest absolute average error for the (a), (m) and (b) parameters. The same test procedure described in Chapters 6.5 and 6.6 was employed to compute the absolute average error of the 3 parameters, with the only difference being that only 100 test fits were performed for each d_n value.

Figure 59 summarizes the results yielded from performing the test procedure on the varied range of d_n values, systematically ranging from [-0.8, 0.8].

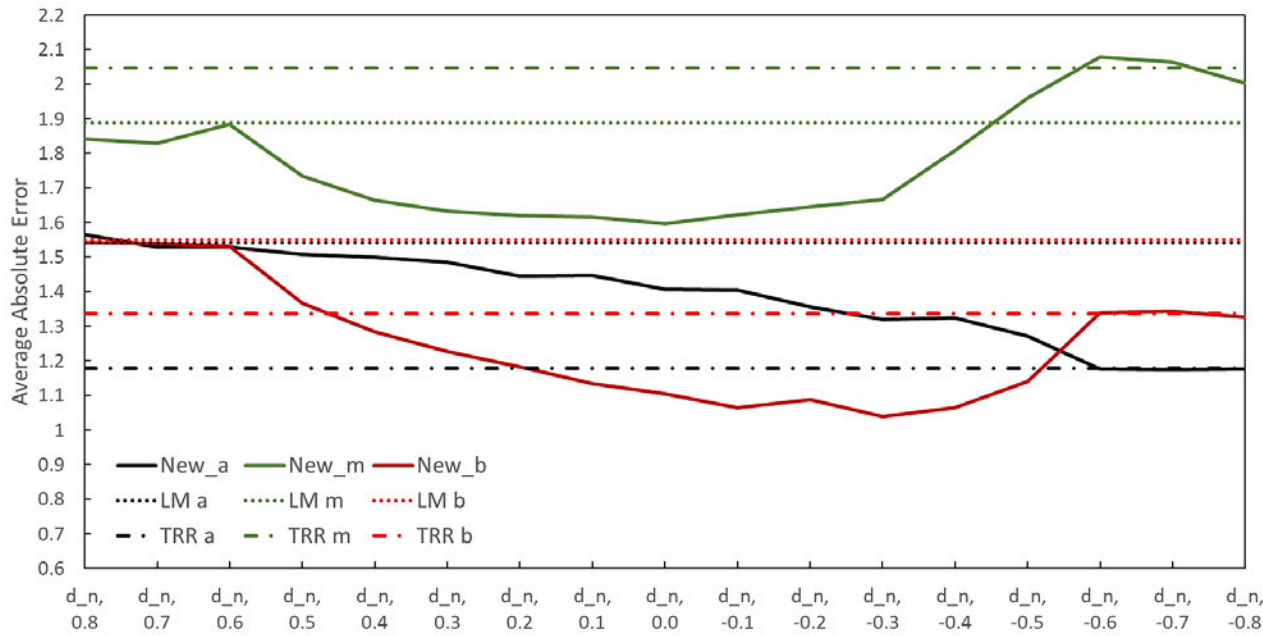


Figure 59: Trends in Performance of New Computational Structure

As illustrated in the figure, d_n values greater than 0.6 and lesser than -0.6 resulted in the new computational structure converging towards either the LM algorithm or the TRR algorithm respectively. This observation then helped to highlight the effective range of d_n values [-0.6 to 0.6] at which the new computational structure starts functioning as intended. To select the most optimal trigger point, the total sum of average absolute error for the 3 parameters was computed for each d_n value.

Figure 60 illustrates the total average error computed from the values of the three parameters for each d_n value depicted in *Figure 59*. As shown by the results illustrated in the figure, the new computational structure yielded improvements in the total average error when the d_n

value was between a range of -0.5 to 0.5. The d_n value of -0.3 was also observed to have the lowest total average error and was thus selected as the optimal trigger point for the new computational structure.

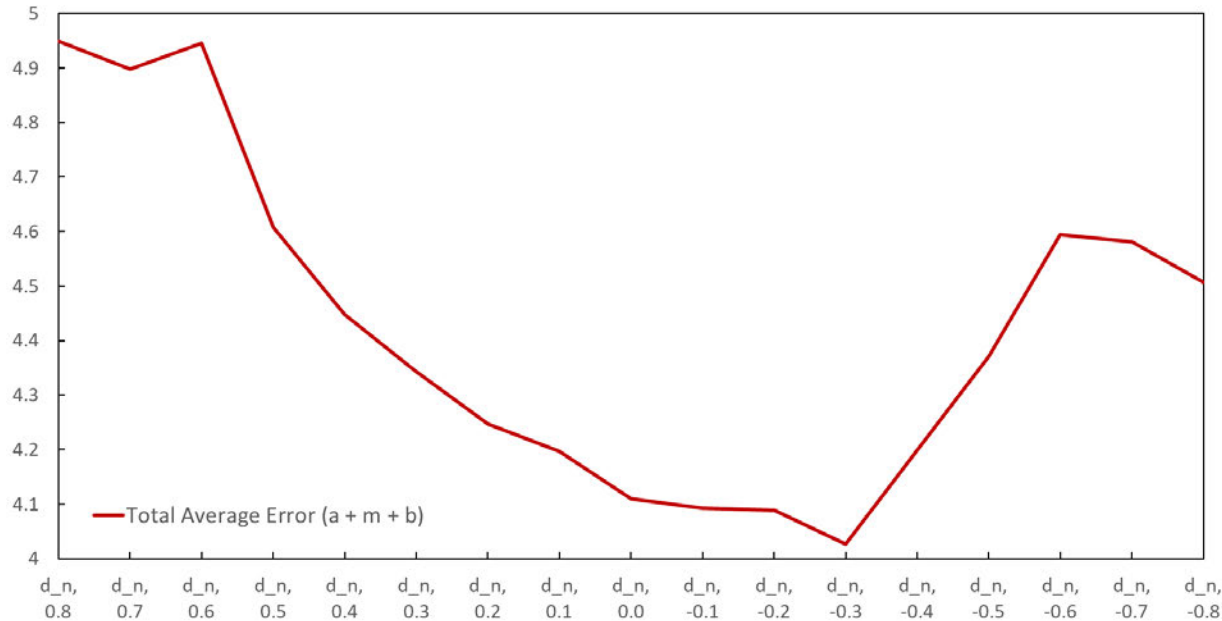


Figure 60: Trends in Performance of New Computational Structure (Total Average Error)

Figure 61 illustrates the total average error computed from the values of the three parameters for each d_n value depicted in Figure 59. As shown by the results illustrated in the figure, the new computational structure generated meaningful improvements in the overall average absolute error for all 3 parameters of the triangular distribution.

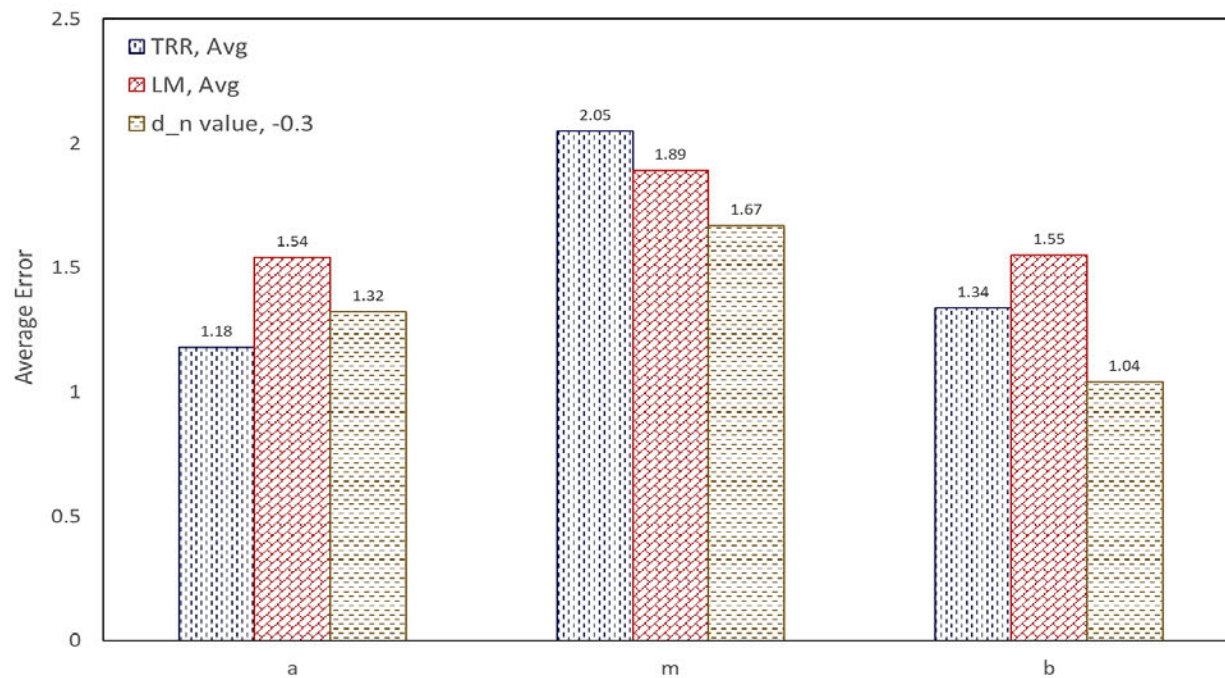


Figure 61: Overall Average Absolute Error

It should be noted that the findings observed from this study should still apply to any other forms or scale of the triangular distribution since:

1. the dataset used incorporates all forms of the triangular distribution, systematically ranging between the left and right most extremities
2. and the results summarized in *Figure 58* depict little to no variations in the skewness coefficient even as extremely right-skewed or left-skewed distributions undergo significant variations in scale.

Having selected an appropriate d_n value for the trigger point of the new computational structure, it was now also important to determine the effects of sample size relative to the performance of the newly developed computational structure observed in Chapter 6.6.2.

The test procedure consisted of producing a random set of 10 to 200 values for each of the defined 44 triangular density functions, with each simulation increasing the sample size by 10. Utilizing the set of values generated as a starting point, a new triangular distribution was defined using the newly developed computational structure with a d_n value of -0.3 to estimate the distribution parameters.

Every time a new triangular distribution is defined, a new set of random samples will be generated from the originally defined triangular density function. This procedure will then be repeated 100 times for each of the 44 triangular density functions developed for the analysis. The procedure eventually produced 4400 estimated triangular-density functions for each variation of the generated sample size (10 to 200 samples @ 10 samples increment) and consisted of 100 approximations for every one of the 44 predefined triangular distributions summarized in *Table 17*.

Since each of the newly generated triangular distributions had a new approximation for the (a) , (b) and (m) parameters, the newly generated parameters were assessed against the “known” parameters of the original triangular distribution.

As presented in *Figure 62*, there exists a clear relationship between the initial sample size used for the estimation and the performance of the newly developed computation structure. Generally, the trend indicates that an increase in sample size led to more accurate estimates for all 3 parameters of the triangular distribution.

A similar trend was observed in *Figure 63* when the total average error was plotted relative to the sample size. To illustrate the improvements in accuracy relative to the samples size, the relative improvement parameter was computed using the following equation:

$$\text{Relative improvement}_i = \frac{E_{i-1} - E_i}{E_{i-1}} \quad (54)$$

Where E_i is the total average error associated with the current sample size and E_{i-1} is the total average error associated with the previous sample size used. Recall that the sample size was systematically increased with a step size of 10. As depicted in *Figure 63*, relative (step-wise) improvements in accuracy were the greatest when the sample size was in the range of 10 to 100. The improvements however gradually waned off as the sample size exceeded 100. Through this observation, it can be said that a sample size of 100 values may serve as a reasonable stopping point for the user.

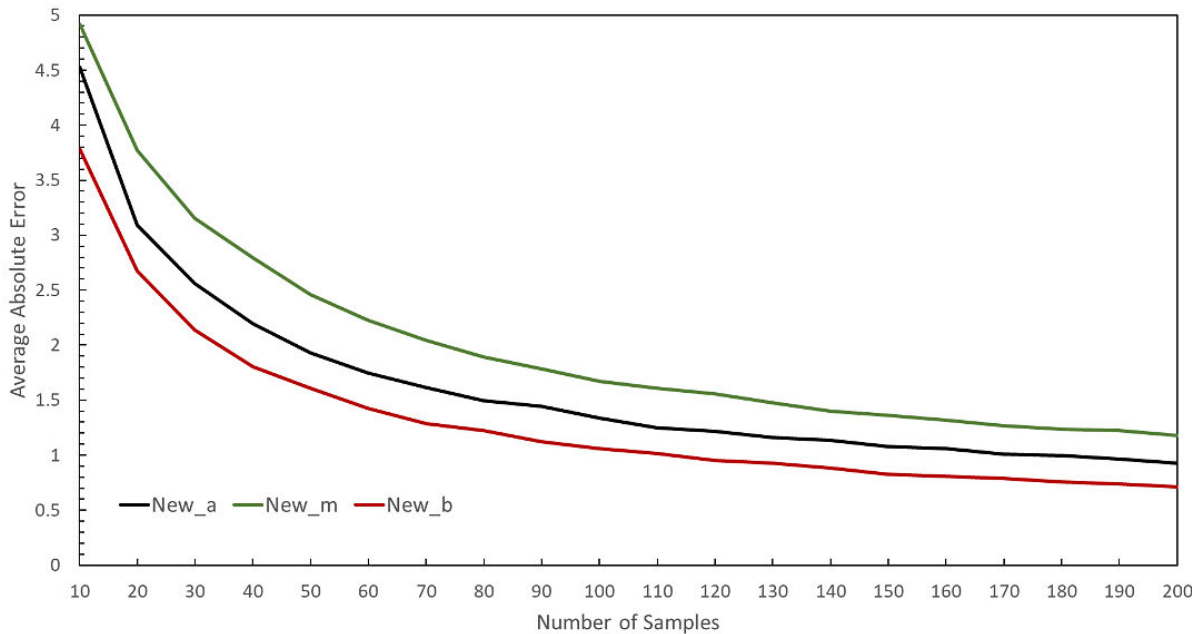


Figure 62: Average absolute error of computational structure relative to sample size

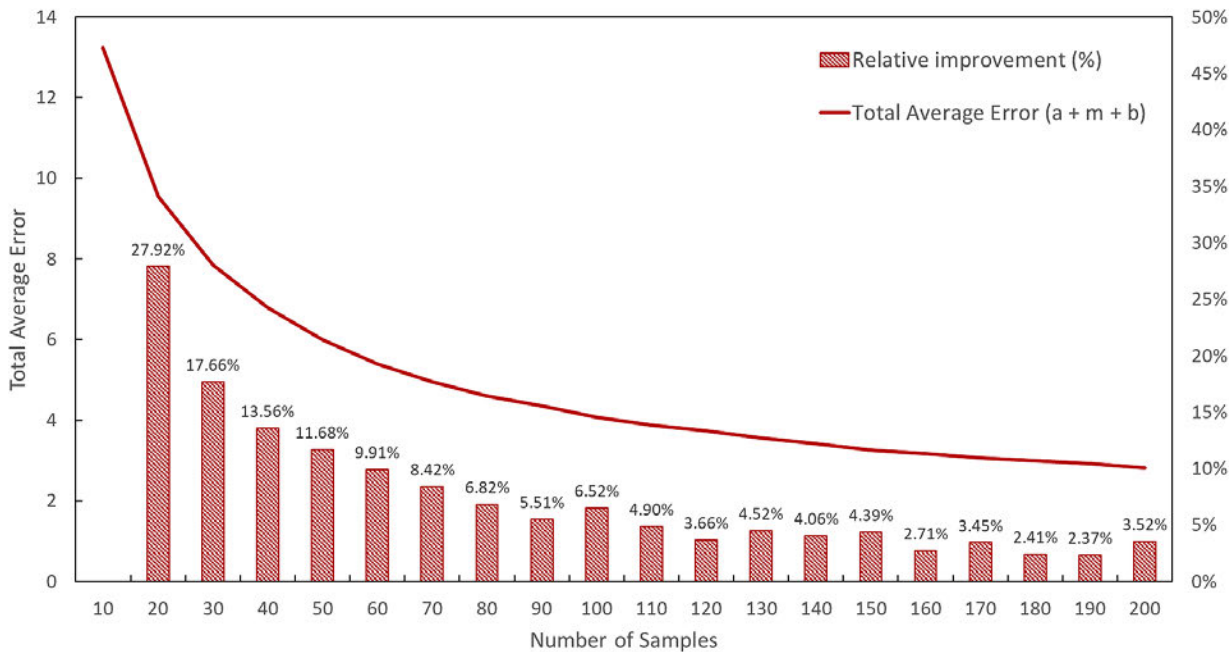


Figure 63: Total average error of computational structure relative to sample size

Having finalized the probabilistic cost estimation model, an Application Programming Interface (API) subroutine was developed with the xlwings python package to facilitate the interaction of the cost estimating system with an excel spreadsheet containing the life cycle cost financial model (described in Chapter 7.2). This allows users to easily edit the financial model used for the probabilistic LCCA in a familiar and easy-to-use environment. Together with a subroutine developed to execute the Monte Carlo simulation, the autonomous cost estimating system and the excel spreadsheet with the financial model will be employed for **step three of the feasibility framework** (Performance Evaluation) to perform a Probabilistic Life Cycle Cost Assessment (LCC/NPV/IRR) of the four UWHS configurations.

7.0 Performance Evaluation

This chapter details the **third step of the framework** (Performance Evaluation), and details the limitations and assumptions surrounding the assessment of Environmental Benefit for the four UWHS configurations. Additionally, the assumptions and results of the Life Cycle Cost (LCC), Net Present Value (NPV), and Internal Rate of Return (IRR) computations are also reviewed.

7.1 Environmental/ Economical Benefit

By using the integrated valuation methodology, the annual retention of runoff for the bioretention basin was approximated to have a volume of 14,660.72m³ with an avoided treatment cost of approximately 439.82 SGD using the rates provided by (Wise et al., 2010).

Assuming the same conditions as a preexisting UWHS project, water consumption for irrigation was approximated to be 2.985m³ daily for a vegetated land area of 0.1 ha. Additionally, water consumption for block/outdoor washing was assumed to be 3m³ monthly. As a result, the system was approximated to save 1079.50m³ of rainwater annually and avoided/ saved 2957.83 SGD in water usage costs when calculated using the non-domestic potable water price published by PUB in 2022 (PUB, n.d.). It should be noted that water savings were calculated using the unprocessed daily rainfall data summarized in Chapter 3.3.2.

For air quality contributions, NO₂ uptake rates were assumed to be similar to vegetated roofs at 0.27kg per square meter as reported by Clark et al (2008) and as a result, total NO₂ removed annually was approximated to be 138.97 Kg, 185.30 Kg, and 231.62 Kg for 3%, 4% and 5% fraction Bioretention basin area respectively. This resulted to an avoided annual cost savings of 1027.00, 1369.33, and 1711.69 SGD respectively.

Although these metrics provide an indication/ gauge of the environmental benefits and cost savings that can be expected from the implementation of a bioretention basin, they are unable to holistically evaluate the bioretention basin due to insufficient data in the space of energy savings from mitigation of urban heat island effects, flood risk damage, hydrological improvements & associated runoff treatment costs (Table 13), recreational value, climate related metrics comprising of annual direct carbon sequesterization potential, CO₂ uptake and air quality benefits in terms of SO₂ removal, O₃ removal, PM_{2.5} Removal and PM₁₀ removal. Additionally, the derivation of cost savings obtained from both Wang et al (2016) and Clark et al (2008) were specific to regions outside of Singapore. As a result, further research should be conducted to quantify and account for the environmental benefits of the bioretention basin if a prudent estimate is desired. Nevertheless, the environmental benefits in the form of cost savings presented in this chapter serves as an indication to the expected benefits of implementing a bioretention basin. In the same manner, it is important to note that the annual rain water savings obtained from the assumption above may only used as a rough indication to the potential economic benefits of the UWHS.

7.2 Life Cycle Cost Assessment

The life cycle cost (LCC) assessment is an instrument for determining the economic costs of a product over its entire lifecycle (ISO, 2017). In the field of evaluating and selecting economical investments/entreprises, LCC remains as one of the most popular tools in the field due to its role in comparing the costs of different products and projects. Consequently, it makes it possible to select the best investments to undertake based on their corresponding cost performance (Slys et al., 2012). When computing the LCC of a project, costs associated to its raw materials, construction, operation, maintenance and end of life is usually considered (Vineyard et al., 2015).

In this study, the capital costs, together with operation and maintenance (O&M) cost were used as the basis for comparison between the four configurations S1, S2, S3 and S4 detailed in Chapter 5.8. Given that the focus of this study is aimed at investigating the feasibility of implementing the UWHS in existing HDB precincts, the design life of the system was assumed to be 50 years, half the st. The construction was assumed to be completed in year 0 while the operation and maintenance (O&M) cost was assumed to occur from Year 1 to Year 50. Since there exists no formal reference for the capital costs of the UWHS configurations proposed, cost values were approximated [REDACTED] and modelled using the triangular distribution (*Table 20*).

Table 20: Modelled Cost Distribution

Detention Tank (\$/m ³) incl. UWHS		Bioretention Basin (\$/m ²)	
Depth	Cost (a,m,b)	Area	Cost (a,m,b)
2 - 2.5m	700, 710, 750	< 50m ²	100, 110, 150
2.5 - 3m	700, 715, 750	< 100m ²	100, 115, 150
3 - 3.5m	700, 720, 750	< 200m ²	100, 120, 150
3.5 - 4m	700, 725, 750	< 400m ²	100, 125, 150
4 - 4.5m	700, 730, 750	> 400m ²	100, 130, 150

The corresponding annual O&M costs were assumed to be a fixed proportion (*p*) of costs relative to the capital cost, i.e., 0.93% for the Bioretention Basin (Wang et al., 2016) and 0.55% for the Detention Tank + UWHS.

The following formulas were then used to compute the LCC of the four configurations (Hou et al., 2022) :

$$LCC = C_{capital} + \sum_{t=1}^n PV_{O\&M} \quad (55)$$

$$PV_{O\&M(t)} = \frac{FV_{O\&M(t)}}{(1 + d + i)^t} \quad (56)$$

$$FV_{O\&M(t)} = C_{capital} \times p \times (1 + i)^t \quad (57)$$

Where, $C_{capital}$ is the associated capital cost of the infrastructure, $PV_{O\&M(t)}$ is the present value of the O&M costs in year t , and n is the total number of years defined as the lifecycle of the infrastructure. $FV_{O\&M(t)}$ represents the future value of the O&M cost, with a discount rate d of 1% applied, an inflation rate i of 2% applied and p representing the proportion factor used to calculate annual O&M costs.

Additionally, the Net Present Value (NPV) and Internal Rate of Return (IRR) are computed using the following equations (Wang et al., 2016):

$$NPV = \sum_{t=1}^n \frac{C_t}{(1 + d + i)^t} - C_{capital} \quad (58)$$

$$\sum_{t=1}^n \frac{C_t}{(1 + IRR)^t} - C_{capital} = 0 \quad (59)$$

Where C_t is the net cash flow (i.e., annual savings – O&M costs).

These equations were then used to populate the predeveloped excel spreadsheet to form a simple financial model. The probabilistic cost estimation model together with the developed Monte Carlo simulation subroutine (Chapter 6.0) were used to simulate the probability distribution of LCC, NPV and IRR for all 4 UWHS configurations. For the purpose of this study, 5000 iterations was performed using the Monte Carlo subroutine.

The detailed probability distribution of LCC, NPV and IRR for configurations S1, S2, S3 and S4 are attached in Appendix 10.7.

These parameters alongside the cost savings, capital and O&M costs of the UWHS configurations are summarized in *Table 21*.

Table 21: Life Cycle Cost (LCC), Net Present Value (NPV) and Internal Rate of Return (IRR) results

Parameter	S1 (Mean)	S2 (Mean)	S3 (Mean)	S4 (Mean)
Capital Costs (SG\$)	432,194	443,773	448,673	393,690
Annual O&M Costs (SG\$)	2,623	2,770	2,878	2,165
Life Cycle Costs (LCC) (SG\$)	535,487	552,819	561,976	478,949
Annual Savings ^a (SG\$)	4,425	4,767	5,109	2,958
Net Present Value (SG\$)	-385,847	-392,375	-391,249	-373,299
Internal Rate of Return	-5.00%	-4.79%	-4.52%	-6.87%

(Mean): Mean Value computed from the resultant dataset of 5000 iterations from Monte Carlo Simulation.

^aAnnual Savings (SG\$) computed using values in Chapter 7.1

From the table, capital costs for configuration S1 – S3 (with Bioretention Basin) were relatively more expensive when compared to that of configuration S4. This trend continues when

comparing the annual O&M cost between the UWHS configurations. As a result, the computed LCC of configuration S4 was marginally lesser than the values observed for configuration S1 – S3.

When comparing annual cost savings however, the use of valuation methodologies associated to environmental benefits resulted to configurations S1 - S3 generating a higher savings amount as compared to configuration S4. Consequently, this resulted to configurations S1 – S3 producing a larger IRR when compared to S4 signalling that configurations S1 - S3 was more profitable than S4. Nevertheless, due to the short lifecycle of the project, S4 returned a higher NPV when compared to configurations S1 - S3.

Since a positive NPV and IRR means that the monetary benefits of the project exceeds the cost of implementation and its operations/maintainance, it can be shown that the UWHS configurations coupled with the current assumptions (cost savings, etc) is an unprofitable investment. Depending on acceptable level of conservativeness/ exposure to financial risk, the probability distribution of LCC, NPV and IRR values are also available in Appendix 10.7 which allows the user to extract LCC, NPV and IRR values based on the desired confidence interval (90%, 95%, 99%, etc).

8.0 Conclusions & Recommendations for future work

8.1 Conclusion

This study consisted in the modelling of the rainfall-runoff relationships in the Jurong East urban catchment in Singapore, to qualitatively and quantitatively ascertain the efficacy/feasibility of four UWHS configurations when implemented in a pre-existing HDB urban catchment. This included, assessing the suitability of landscape and hydrological conditions of the site, designing/hydrologically modelling the UWHS, and verifying that a reasonable hydrological model could be constructed using only a small amount of available data. The framework concludes with the development and application of an automated cost estimating system with a monte carlo subroutine used to support the probabilistic life cycle cost assessment of all four UWHS configurations.

The key findings/ conclusions from the study are summarized in detail below:

1. As climate change continues to progressively exacerbate the unpredictable & varied nature of rainfall and its extremities during the wet (Flood) and dry (Drought) seasons, the need for suitable stormwater management strategies that serves a purpose during droughts, low intensity, and high intensity storm events will continue to grow in importance. The four step stormwater management feasibility framework then offers an approach to identify and integrate the hydrological performance of the stormwater management infrastructure with the qualitative communal aspects of its implementation during the planning phase.
2. For the hydrological modelling of any catchment, large amounts of data/ input parameters are usually required. In this study, it was incredibly difficult to obtain an accurate DEM of the site. As a result, the SRTM DEM (30 x 30m) was used after undergoing hydrological treatment and interpolation. To identify the best combination of hydrological treatment and DEM interpolation, the results obtained from 2 hydrological treatment algorithms and 3 interpolation methodologies were evaluated. The study found that the Fill Sinks (Wang & Liu, 2006) Algorithm coupled with the Bilinear interpolation methodology produced the most reasonable resultant DEM.
3. To model and ascertain the hydrological performance of the UWHS, the study involved verifying the possibility of building a catchment model using only the few sources of free and available data. This has since been partly confirmed since the model fitted the likely lag time, and maximum discharge flow rate of the catchment with reference to the Code of practice on Surface Water Drainage by PUB. Additionally, through a sensitivity study of the various contributing model parameters, extracted parameters with high uncertainty (e.g: Slope%, Mannings N for Overland Flow, etc) were found to typically fall within the low end of the sensitivity ranking results further improving confidence in the final model output.

4. An autonomous cost estimation system using the method of least-squares fit and the triangular probability distribution was developed to model historical UWHS construction costs. Two optimization algorithms namely the Levenberg-Marquardt (LM) and the Trust Region Reflective (TRR) algorithm were investigated for its efficacy in minimizing the differences in squares between the CDF derived from the historical data points and the theoretical best fit curve. Through the results from the trial, the study found that the LM algorithm was most effective in situations where the dataset distribution exhibit characteristics similar to a left skewed triangular distribution. In sharp contrast, the TRR algorithm was found to perform incrementally better in cases where the distribution exhibit characteristics similar to a right skewed triangular distribution. Due to the aforementioned findings of the LM and TRR algorithm, the next phase of the investigation involved studying the optimal skewness/ “trigger” point at which to employ either the LM or TRR algorithm. By utilizing the skewness equation derived by Weisstein (2001) to measure the underlying skewness of the assumed historical cost dataset, the study found that the “trigger” point of -0.3 produced the most accurate results.

5. To assess the economic feasibility of the UWHS systems, a financial model consisting of the Life Cycle Cost (LCC), Net Present Value (NPV), and Internal Rate of Return (IRR) was developed and subsequently linked to the autonomous cost estimation system through a Monte Carlo sub-routine. This allowed the user to generate a probability distribution for each of the metrics used in the financial model. Nevertheless, with the assumptions used in this study, all four configurations of the UWHS were identified to be unprofitable investments with a negative NPV and IRR. The framework can thus be viewed to have successfully achieve its initial objective of providing the steps required to evaluate the feasibility of implementing the UWHS for various sites.

As mentioned in Chapter 7.1, the factors contributing to the expected cost savings in this study incorporates a sampling of economic benefits based on the available literature found during the course of this study. Updating and extending the number and type of economic benefits reviewed in this framework would be a reasonable approach to bring a more holistic assessment of benefits into infrastructure investment cost comparisons as well as to integrate its associated economic benefits into the existing life cycle cost assessment.

Alternatively, a hydrological/ treatment cost-effectiveness assessment approach may be developed to investigate the relationship between hydrological & treatment performance (Chapter 5.8) relative to the LCC of the systems.

Where the benefit to cost assessment metric may then be calculated with:

$$\left(\frac{B}{C}\right)_i = \frac{B_{H(i)} + B_{T(i)}}{LCC_{(i)}} \quad (60)$$

Where $\left(\frac{B}{C}\right)_i$ is the cost effectiveness ratio of configuration i , $B_{H(i)}$ is the average value of the hydrological performance indices, $B_{T(i)}$ is the average value of the treatment performance indices, and $LCC_{(i)}$ is the probability distribution of computed LCC values for configuration i .

This approach however is only able to compare the cost effectiveness between the different configurations and is unable to directly distinguish if the configuration makes economic sense and the user would have to use his judgement to make a decision. As a result, further investigation of the approach was not performed in this study.

8.2 Uncertainties and Recommendations for future work

The uncertainty and limitations of methods were discussed alongside the work in their respective sections. From the study, it is clear that the model would have been easier to set up and calibrate with more accurate/precise data. Of the uncertainties in this study, the first encountered were linked to the creation of a DEM for the study area. Although the processed and resampled DEM depicted hydrologically sensible values after the process, it is evident that there exist errors in its creation. For example, the spatial resolution of the SRTM DEM was identified to be 30m x 30m, and may have inevitably averaged/accounted for the elevation of buildings and trees in the area. As a result, utilizing a paid service to acquire a LIDAR DEM would have been more desirable for the purpose of this study. The determination of SWMM parameters is also afflicted with uncertainties, particularly for the width parameter of each subcatchment and the Curve number used for infiltration. Although these parameters were either partly validated through the rational method, or where applicable, replaced with a more conservative value, performing a model calibration using actual instrumentation data (Hyetograph and Hydrograph) of the site would increase the level of confidence in the output of the catchment model.

Uncertainties also exists in the rates and assumptions made for the financial evaluation of the UWHS configurations. Due to the lack of historical cost data at the time of this study, the capital costs of the systems were approximated by [REDACTED]

[REDACTED] and modelled using the triangular distribution. As a result, the financial costs of the system may have been subjected to personal bias of the informants providing the cost estimations for this study. Of particular concern, the derivation of costs savings associated to the environmental benefit of the system was also observed to originate from areas outside of Singapore leading to a high degree of uncertainty associated to its values.

Nevertheless, since this paper focuses on developing a feasibility assessment tailored for the conceptualization phase of a project, some degree of uncertainty is acceptable provided that sufficient effort has been made to be conservative in the estimates.

There are some improvements which can be implemented to work done thus far to produce a more comprehensive and holistic feasibility assessment framework or to address a particular obstacle faced during the study. Some of the recommendations for future work includes:

1. Using an Artificial Neural Network (ANN) to generate an accurate high resolution DEM of the site using the SRTM DEM in conjunction with satellite imagery of the site.
2. Although the study only investigates hydrological and treatment performance of the UWHS configurations when subjected to a 10 year storm event due to the lack of time, future work may be done in assessing the hydrological and treatment performance of the UWHS systems for storm events of various intensities. When integrated with the work done thus far, this evaluation component allows for a more holistic evaluation of the UWHS configurations and may support further development into selecting the configurations based on its cost effectiveness. (Low Frequency High Intensity vs High Frequency Low Intensity storm events.) Appendix 10.8 illustrates these trends in hydrological and treatment performance of the UWHS configurations (2, 3, 5, 10yr ARI storm events).
3. Further work can be done in updating and extending the number and type of economic benefits reviewed in this study, to bring a more holistic assessment of benefits into infrastructure investment cost comparisons as well as to integrate the economic benefits into the existing life cycle cost assessment. This consists of additional modelling and development of consistent methods for aggregating site practices and impacts into cumulative effects/ cost savings on the drainage network, the water network, the metropolitan network or the entire region. It may also be useful to distinguish these benefits based on the stakeholder interests. (e.g. categorize the benefits based on the stakeholder's interest: water savings for property owner, sequestered carbon for the nation of Singapore, etc.)
4. To improve the accuracy in water cost savings estimates, an autonomous water balance model based off a large dataset of historical rainfall data can be developed to generate a probabilistic range of water savings which can then be incorporated to the Monte Carlo Sub-Routine developed in this study. Technically, any other parameters that would benefit from being probabilistic expressed can be incorporated either through the Monte Carlo Sub-Routine, or through the preexisting formulas in Excel.
5. Although this paper recommends a sample size of 100 for the cost estimation system, further investigation to validate this number was not performed due to the constraint of time. As a result, further work may be done to investigate the effects of increasing range/ spread of the dataset relative to number of samples required to achieve a reasonably accurate estimate from the cost estimation system.

This Capstone Project has made it possible for me to learn more about engineering through the development of models, simulation packages and overall feasibility assessment framework. The work performed in relation to this project has consequently provided me the opportunity to perform self-directed learning, and explore as well as discover essential skills and competencies contributing to the engineering profession outside of the conventional classroom setting. As a result, this capstone project has helped me gained an appreciation for the vast field of engineering as well as improve my confidence and adaptability in undertaking engineering challenges in the future.

9.0 References

1. Abraham, S., & Punniyamoorthy, M. (2021). A fuzzy approach using asymmetrical triangular distribution in a two-person zero-sum game for a multi-criteria decision-making problem. *Quantum Machine Intelligence*, 3(1), 1-24.
2. AbouRizk, S. M., Halpin, D. W., & Wilson, J. R. (1994). Fitting beta distributions based on sample data. *Journal of Construction Engineering and Management*, 120(2), 288-305.
3. Ahmad, I. (1992). Contingency allocation: a computer-aided approach. *AACE International Transactions*, 1, F-5.
4. Akan, O. A. (1993). *Urban stormwater hydrology: a guide to engineering calculations*. Crc Press.
5. Akram, F., Rasul, M. G., Khan, M. M. K., & Amir, M. S. I. I. (2014). A review on stormwater harvesting and reuse. *International Journal of Environmental, Earth Science and Engineering*, 8(3), 178-187.
6. American Society of Civil Engineers. (1992). *Design and construction of urban stormwater management systems*. American Society of Civil Engineers and Water Environment Federation.
7. Back, W. E., Boles, W. W., & Fry, G. T. (2000). Defining triangular probability distributions from historical cost data. *Journal of Construction Engineering and Management*, 126(1), 29-37.
8. BCA. (2011). *BCA Awards 2011. Building and Construction Authority Green Mark*, 25. Bca.gov.sg. <https://www.bca.gov.sg/greenmark/others/gm2011.pdf>
9. BCA. (2018). *BCA Awards 2018. Building and Construction Authority Green Mark*, 85. Bca.gov.sg. <https://www.bca.gov.sg/GreenMark/others/gm2018.pdf>
10. Bedient, P. B., Huber, W. C., & Vieux, B. E. (2013). *Hydrology and Floodplain Analysis*. Prentice Hall.
11. Berghen, F. V. (2004). Levenberg-Marquardt algorithms vs trust region algorithms. *IRIDIA, Université Libre de Bruxelles*, 1.

12. Burns, M. J., Fletcher, T. D., Duncan, H. P., Hatt, B. E., Ladson, A. R., & Walsh, C. J. (2015). The performance of rainwater tanks for stormwater retention and water supply at the household scale: an empirical study. *Hydrological Processes*, 29(1), 152-160.
13. Butler, D., & Davies, J. W. (2004). *Urban drainage*. Spon.
14. Campisano, A., Butler, D., Ward, S., Burns, M. J., Friedler, E., DeBusk, K., ... & Han, M. (2017). Urban rainwater harvesting systems: Research, implementation and future perspectives. *Water research*, 115, 195-209.
15. Cantone, J. (2010). *Improved understanding and prediction of the hydrologic response of highly urbanized catchments through development of the Illinois Urban Hydrologic Model (Doctoral dissertation)*. <http://hdl.handle.net/2142/16073>
16. Chan, E. S., Balmforth, D., Kan, Y., Koike, T., Lampe, L., Lim, K. K., & Yong, K. K. (2012). Report on key conclusions and recommendations of the expert panel on drainage design and flood protection measures. *Singapore's National Water Agency: Singapore*.
17. Check, L. M. (1997). Drainage planning and control in the urban environment the Singapore experience. *Environmental Monitoring and Assessment*, 44(1), 183-197.
18. Chen, W., Huang, G., & Zhang, H. (2017). Urban stormwater inundation simulation based on SWMM and diffusive overland-flow model. *Water science and technology*, 76(12), 3392-3403.
19. Choi, K. S., & Ball, J. E. (2002). Parameter estimation for urban runoff modelling. *Urban water*, 4(1), 31-41.
20. Chow, V. T., Maidment, D. R., & Mays, L. W. (1988). *Applied Hydrology*, McGraw-Hill Book Company, New York.
21. Christian Amos, C., Rahman, A., & Mwangi Gathenya, J. (2016). Economic analysis and feasibility of rainwater harvesting systems in urban and peri-urban environments: A review of the global situation with a special focus on Australia and Kenya. *Water*, 8(4), 149.
22. Clark, C., Adriaens, P., & Talbot, F. B. (2008). Green roof valuation: a probabilistic economic analysis of environmental benefits. *Environmental science & technology*, 42(6), 2155-2161.

23. Coffman, L. (2000). Low-impact development design strategies, an integrated design approach. Prince George's Cty. *Md. Dep. Environ. Resour. Programs Plan. Div.*
24. Conrad, O. (2020). *SAGA-GIS Tool Library Documentation (v7.8.2)*. Sourceforge.io. https://saga-gis.sourceforge.io/saga_tool_doc/7.8.2/ta_preprocessor_7.html
25. County of San Diego, Department of Planning and Land Use. (2008). *Impervious Surface Coefficients for General Land Use Categories for Application within San Diego County*.
26. Courty, L. G., Soriano-Monzalvo, J. C., & Pedrozo-Acuña, A. (2019). Evaluation of open-access global digital elevation models (AW3D30, SRTM, and ASTER) for flood modelling purposes. *Journal of Flood Risk Management*, 12, e12550.
27. Cronshey, R. (1986). *Urban hydrology for small watersheds* (No. 55). US Department of Agriculture, Soil Conservation Service, Engineering Division.
28. Curran, M. W. (1989). Range estimating: Contingencies with confidence. *AACE International Transactions*, B-7.
29. Davis, A. P., Hunt, W. F., Traver, R. G., & Clar, M. (2009). Bioretention technology: Overview of current practice and future needs. *Journal of environmental engineering*, 135(3), 109-117.
30. Davis, A. P., Traver, R. G., Hunt, W. F., Lee, R., Brown, R. A., & Olszewski, J. M. (2012). Hydrologic performance of bioretention storm-water control measures. *Journal of Hydrologic Engineering*, 17(5), 604-614.
31. De Sousa, M. R., Montalto, F. A., & Spatari, S. (2012). Using life cycle assessment to evaluate green and grey combined sewer overflow control strategies. *Journal of Industrial Ecology*, 16(6), 901-913.
32. DeBusk, K. M., Hunt, W. F., & Wright, J. D. (2013). Characterizing rainwater harvesting performance and demonstrating stormwater management benefits in the humid southeast USA. *JAWRA Journal of the American Water Resources Association*, 49(6), 1398-1411.
33. Department of Statistics, Singapore. (n.d.). *Singapore Population*. Singstat.gov.sg. <https://www.singstat.gov.sg/modules/infographics/population>
34. Department of Statistics, Singapore. (n.d.). *Changi Climate Station*. Singstat.gov.sg. <https://data.gov.sg/search?q=Changi+Climate+Station>

35. Despins, C., Farahbakhsh, K., & Leidl, C. (2009). Assessment of rainwater quality from rainwater harvesting systems in Ontario, Canada. *Journal of Water Supply: Research and Technology—AQUA*, 58(2), 117-134.
36. DiGiano, F. A., Adrian, D. D., & Mangarella, P. A. (Eds.). (1977). *Short Course Proceedings: Applications of Stormwater Management Models, 1976* (Vol. 1). Environmental Protection Agency, Office of Research and Development, Municipal Environmental Research Laboratory.
37. Dooge, J. C. (1957). The rational method for estimating flood peaks. *Engineering*, 184(1), 311-313.
38. Duncan, H. (1999). *Urban stormwater quality: a statistical overview*. CRC for Catchment Hydrology.
39. Earth Resources Observation and Science Center, EROS. (2018, July 30). *USGS EROS Archive - Digital Elevation - Shuttle Radar Topography Mission (SRTM) 1 Arc-Second Global* | U.S. Geological Survey. Usgs.gov.
https://www.usgs.gov/centers/eros/science/usgs-eros-archive-digital-elevation-shuttle-radar-topography-mission-srtm-1?qt-science_center_objects=0#overview
40. Environmental Systems Research Institute, ESRI. (2009, April 25). *ArcGIS Desktop 9.3 Help*. Esri.com.
<http://webhelp.esri.com/arcgisdesktop/9.3/index.cfm?TopicName=welcome>.
41. Farr, T. G., Rosen, P. A., Caro, E., Crippen, R., Duren, R., Hensley, S., ... & Alsdorf, D. (2007). The shuttle radar topography mission. *Reviews of geophysics*, 45(2).
42. Fletcher, T. D., Shuster, W., Hunt, W. F., Ashley, R., Butler, D., Arthur, S., ... & Viklander, M. (2015). SUDS, LID, BMPs, WSUD and more—The evolution and application of terminology surrounding urban drainage. *Urban water journal*, 12(7), 525-542.
43. Fuller, S. K., & Petersen, S. R. (1996). Life cycle costing manual. *NIST handbook*, 135.
44. Gesch, D., Oimoen, M., Danielson, J., & Meyer, D. (2016). Validation of the ASTER global digital elevation model version 3 over the conterminous United States. *The International Archives of Photogrammetry, Remote Sensing and Spatial Information Sciences*, 41, 143.
45. Gilbreath, A., McKee, L., Shimabuku, I., Lin, D., Werbowski, L. M., Zhu, X., ... & Rochman, C. (2019). Multiyear water quality performance and mass accumulation of PCBs,

mercury, methylmercury, copper, and microplastics in a bioretention rain garden. *Journal of Sustainable Water in the Built Environment*, 5(4), 04019004.

46. Gironás, J., Roesner, L. A., & Davis, J. (2009). *Storm Water Management Model Applications Manual*. United States Environmental Protection Agency. EPA/600/R-09/077.
47. Goh, X. P., Radhakrishnan, M., Zevenbergen, C., & Pathirana, A. (2017). Effectiveness of runoff control legislation and Active, Beautiful, Clean (ABC) Waters design features in Singapore. *Water*, 9(8), 627.
48. Guo, J. C. (2003). *Urban storm water design*. Water Resources Publication.
49. Hou, Q., Cheng, Y., Yuan, Y., & Wang, M. (2022). Assessing Hydrological Cost-Effectiveness of Stormwater Multi-Level Control Strategies in Mountain Park under the Concept of Sponge City. *Water*, 14(10), 1524.
50. Hua, J., Liang, Z., & Yu, Z. (2003). A modified rational formula for flood design in small basins 1. *JAWRA Journal of the American Water Resources Association*, 39(5), 1017-1025.
51. Huber, W. C. (1986). Deterministic modeling of urban runoff quality. In *Urban runoff pollution* (pp. 167-242). Springer, Berlin, Heidelberg.
52. Huff, F. A. (1967). Time distribution of rainfall in heavy storms. *Water resources research*, 3(4), 1007-1019.
53. INLIS. (2022). Sla.gov.sg.
<https://app1.sla.gov.sg/INLIS/#/BCA/BH/Detail>
54. International Organization for Standardization. (2017). *Buildings and constructed assets - Service life planning - Part 5: Life-cycle costing* (ISO Standard No. 15686-5:2017). Iso.org.
<https://www.iso.org/standard/61148.html>
55. Irvine, K., Chua, L., & Eikass, H. S. (2014). The four national taps of Singapore: A holistic approach to water resources management from drainage to drinking water. *Journal of water management modeling*, 1-11.
56. Javaheri, H., & Liong, S. Y. (2000). On Automatic Calibration of the SWMM Model. *Journal of Water Management Modeling*.

57. Jin, F. (2020). CVE1231 Engineering Geology and Soil Mechanics. *Topic 5 Engineering Geology & Singapore Geology - Engineering Geology & Singapore Geology_updated*. Singapore Institute of Technology: Engineering.
58. Jones, M. P., & Hunt, W. F. (2010). Performance of rainwater harvesting systems in the southeastern United States. *Resources, Conservation and Recycling*, 54(10), 623-629.
59. Jun, C., Qin, X., & Lu, W. (2018, September). Temporal pattern analysis of rainstorm events for supporting rainfall design in a tropical city. In *International Conference on Urban Drainage Modelling* (pp. 380-384). Springer, Cham.
60. Kang, M. S., Goo, J. H., Song, I., Chun, J. A., Her, Y. G., Hwang, S. W., & Park, S. W. (2013). Estimating design floods based on the critical storm duration for small watersheds. *Journal of Hydro-environment Research*, 7(3), 209-218.
61. Keys, R. (1981). Cubic convolution interpolation for digital image processing. *IEEE transactions on acoustics, speech, and signal processing*, 29(6), 1153-1160.
62. Kim, H., Seagren, E. A., & Davis, A. P. (2003). Engineered bioretention for removal of nitrate from stormwater runoff. *Water Environment Research*, 75(4), 355-367.
63. Kleidorfer, M. (2010). *Uncertain calibration of urban drainage models: a scientific approach to solve practical problems*. Innsbruck University Press.
64. Knoke, J. R., & Spittler, J. R. (1991). Direct range estimating for change orders. *AACE International Transactions*, M3-1.
65. Kollo, M., & Laanearu, J. (2017). An optimal solution of thermal energy usage in the integrated system of stormwater collection and domestic-water heating. *Urban Water Journal*, 14(2), 212-222.
66. Kratky, H., Li, Z., Chen, Y., Wang, C., Li, X., & Yu, T. (2017). A critical literature review of bioretention research for stormwater management in cold climate and future research recommendations. *Frontiers of Environmental Science & Engineering*, 11(4), 1-15.
67. Kumar, M. (1988). World geodetic system 1984: A modern and accurate global reference frame. *Marine Geodesy*, 12(2), 117-126.
68. Kurt Menke, G. I. S. P., Smith Jr, R., Pirelli, L., & John Van Hoesen, G. I. S. P. (2016). *Mastering QGIS*. Packt Publishing Ltd.

69. LeFevre, G. H., Paus, K. H., Natarajan, P., Gulliver, J. S., Novak, P. J., & Hozalski, R. M. (2015). Review of dissolved pollutants in urban storm water and their removal and fate in bioretention cells. *Journal of Environmental Engineering*, 141(1), 04014050.
70. Lim, H. S. (2003). Variations in the water quality of a small urban tropical catchment: implications for load estimation and water quality monitoring. In *The interactions between sediments and water* (pp. 57-63). Springer, Dordrecht.
71. Lindsay, J. (2012). *Breach depressions*. Github.io.
<https://jblindsay.github.io/ghrg/Whitebox/Help/BreachDepressions.html>
72. Mason, B., & Knight, R. (2001). Sensitive habitat inventory and mapping. Community Mapping Network, Vancouver. *British Columbia, Canada*.
73. McCuen, R. H. (1998). *Hydrologic Analysis and Design* (2nd ed.). Prentice Hall College Div.
74. Meteorological Service Singapore. (2020). *Climate of Singapore*. Weather.gov.sg.
<http://www.weather.gov.sg/climate-climate-of-singapore>
75. Meteorological Service Singapore. (2020). *Historical Daily Records (Ulu Pandan, 2020)* [Data set]. <http://www.weather.gov.sg/climate-historical-daily/>
76. Min, S. K., Zhang, X., Zwiers, F. W., & Hegerl, G. C. (2011). Human contribution to more-intense precipitation extremes. *Nature*, 470(7334), 378-381
77. Mitchell, D. P., & Netravali, A. N. (1988). Reconstruction filters in computer-graphics. *ACM Siggraph Computer Graphics*, 22(4), 221-228.
78. Mlakar, P. F., & Bryant, L. M. (1990). Direct range cost estimating. *AACE International Transactions*, K-4.
79. Mujumdar, P. P. (2001). Flood wave propagation. *Resonance*, 6(5), 66-73.
80. Neo, T. H., Xu, D., Fowdar, H., McCarthy, D. T., Chen, E. Y., Lee, T. M., ... & Hu, J. (2022). Evaluation of Active, Beautiful, Clean Waters Design Features in Tropical Urban Cities: A Case Study in Singapore. *Water*, 14(3), 468.

81. NRCS, U. (2004). National Engineering Handbook: Part 630—Hydrology. Chapter 9: Hydrologic Soil-Cover Complexes. *United States Department of Agriculture-Natural Resources Conservation Service*.
82. NRCS, U. (2004). National Engineering Handbook—Part 630 Hydrology, Chapter 10: Estimation of Direct Runoff from Storm Rainfall. *United States Department of Agriculture-Natural Resources Conservation Service*.
83. NRCS, U. (2010). National Engineering Handbook—Part 630 Hydrology, Chapter 15: Time of concentration. *United States Department of Agriculture-Natural Resources Conservation Service*.
84. Park, M., Chung, G., Yoo, C., & Kim, J. H. (2012). Optimal design of stormwater detention basin using the genetic algorithm. *KSCE Journal of Civil Engineering*, 16(4), 660-666.
85. Paus, K. H., & Braskerud, B. C. (2014). Suggestions for designing and constructing bioretention cells for a nordic climate. *Journal of Water Management and Research*, 3, 139-150.
86. Philp, M., McMahon, J., Heyenga, S., Marinoni, O., Jenkins, G., Maheepala, S., & Greenway, M. (2008). Review of stormwater harvesting practices. *Urban Water Security Research Alliance*.
87. Pitts, J. (1984). A review of geology and engineering geology in Singapore. *Quarterly Journal of Engineering Geology*, 17(2), 93-101.
88. Pitt, R., Lilburn, M., Nix, S., Durrans, S. R., Burian, S., Voorhees, J., & Martinson, J. (1999). Guidance manual for integrated wet weather flow (WWF) collection and treatment systems for newly urbanized areas (New WWF Systems). *Current and Future Design Practices*.
89. Public Utilities Board. (2014). *Active Beautiful Clean Waters Design Guidelines (Fourth Edition)*. Pub.gov.sg.
https://www.pub.gov.sg/Documents/ABC_Waters_Design_Guidelines.pdf
90. Public Utilities Board. (2018). *Code of Practice on Surface Water Drainage (Seventh Edition-December 2018)*. Pub.gov.sg.
https://www.pub.gov.sg/Documents/PUB_COP_7th_Edition.pdf

91. Public Utilities Board. (2018). *Condensed Booklet on Engineering Procedures for ABC Waters Design Features (2018 Edition)*. Pub.gov.sg.
https://www.pub.gov.sg/Documents/Condensed_Booklet_of_Engin_Procedures.pdf
92. Public Utilities Board. (2021). *On-site Stormwater Detention Tank Systems Technical Guide (Revision 1: May 2021)*. Pub.gov.sg.
<https://www.pub.gov.sg/Documents/detentionTank.pdf>
93. Public Utilities Board. (2021, September 6). [UPDATE] Flash floods at the following locations have subsided [Image attached] [Status update]. Facebook.
<https://www.facebook.com/photo.php?fbid=149261420711753&set=a.146148701023025&type=3>
94. Public Utilities Board. (n.d.). *Drainage*. PUB, Singapore's National Water Agency. Retrieved Jan 15, 2022, from <https://www.pub.gov.sg/drainage>
95. PUB. (n.d.). *Water Price*. PUB, Singapore's National Water Agency. Retrieved July 15, 2022, from <https://www.pub.gov.sg/watersupply/waterprice>
96. Public Works Department Singapore. (1976). *Geology of the Republic of Singapore*. Public Works Department (Singapore).
97. Rahardjo, H., Aung, K. K., Leong, E. C., & Rezaur, R. B. (2004). Characteristics of residual soils in Singapore as formed by weathering. *Engineering Geology*, 73(1-2), 157-169.
98. Rice, E. W., Baird, R. B., Eaton, A. D., & Clesceri, L. S. (2012). APHA (American Public Health Association): Standard method for the examination of water and wastewater. *Washington DC (US): AWWA (American Water Works Association) and WEF (Water Environment Federation)*.
99. Rieger, W. (1998). A phenomenon-based approach to upslope contributing area and depressions in DEMs. *Hydrological Processes*, 12(6), 857-872.
100. Rodriguez, E., Morris, C. S., & Belz, J. E. (2006). A global assessment of the SRTM performance. *Photogrammetric Engineering & Remote Sensing*, 72(3), 249-260.
101. Romnée, A., Evrard, A., & Trachte, S. (2015). Methodology for a stormwater sensitive urban watershed design. *Journal of Hydrology*, 530, 87-102.
102. Ross, C.W., L. Prihodko, J.Y. Anchang, S.S. Kumar, W. Ji, and N.P. Hanan. 2018. Global Hydrologic Soil Groups (HYSOGs250m) for Curve Number-Based Runoff Modeling. ORNL

Distributed Active Archive Center.

<https://doi.org/10.3334/ORNLDAAC/1566>

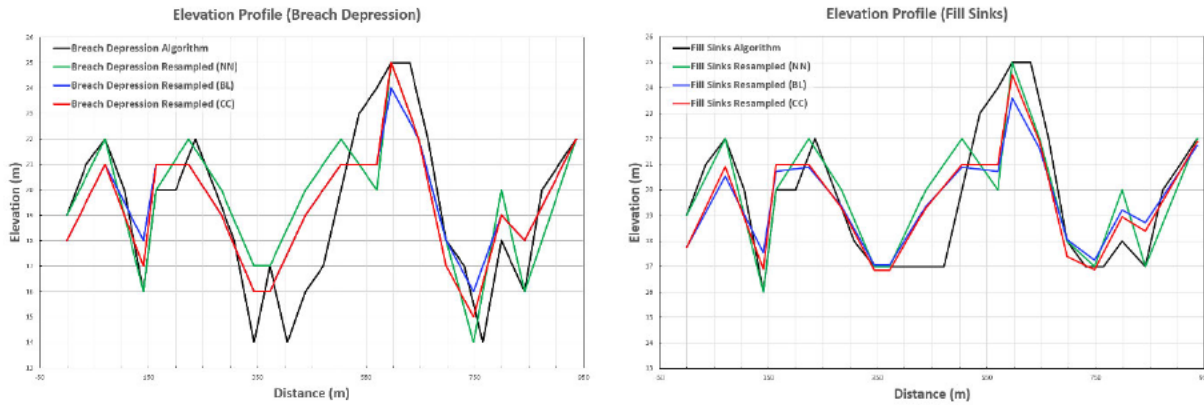
103. Rossman, L. A., & Supply, W. (2006). *Storm water management model, quality assurance report: dynamic wave flow routing*. US Environmental Protection Agency, Office of Research and Development, National Research Management Research Laboratory.
104. Rossman, L. A. (2015). Storm water management model user's manual version 5.1 (EPA/600/R-14/413b). *US EPA National Risk Management Research Laboratory, Cincinnati, Ohio, USA*.
105. Rossman, L. A., & Huber, W. C. (2016). Storm Water Management Model Reference Manual Volume I—Hydrology (revised)(EPA/600/R-15/162A). *US Environmental Protection Agency (EPA)*.
106. Rossman, L. A., & Huber, W. C. (2016). Storm Water Management Model Reference Manual Volume III—Water Quality. US EPA, Office of Research and Development, NRMRL. *Water Supply and Water Resources Division. EPA/600/R-16/093*.
107. Rossman, L. (2017). *Storm Water Management Model Reference Manual Volume II—Hydraulics*. US Environmental Protection Agency, Washington, DC. EPA/600/R-17/111.
108. Rowland, W. P., & Curran, K. M. (1991). Range estimating in value engineering. *AACE International Transactions*, G3-1.
109. Sartor, J. D., & Boyd, G. B. (1972). *Water pollution aspects of street surface contaminants* (Vol. 2). US Government Printing Office.
110. Sien, C. L., & Fook, F.S. (1991). The Biophysical Environment of Singapore: Climate and Weather. *The Biophysical Environment of Singapore*, 13-36.
111. Singapore Land Authority. (2021, November 9). *Total Land Area of Singapore*. [Dataset] <https://data.gov.sg/dataset/total-land-area-of-singapore>
112. Singh, V. P., & Woolhiser, D. A. (2002). Mathematical modeling of watershed hydrology. *Journal of hydrologic engineering*, 7(4), 270-292.
113. Sly, D., Stec, A., & Zelenakova, M. (2012). A LCC analysis of rainwater management variants. *Ecological Chemistry and Engineering*, 19(3), 359.

114. Song, H., Qin, T., Wang, J., & Wong, T. H. (2019). Characteristics of stormwater quality in Singapore catchments in 9 different types of land use. *Water*, 11(5), 1089.
115. Smith, A. A. (2022). *Hydrological Theory*. Miduss.com.
<http://www.miduss.com/theory-Calculating-Runoff-SWMM-RUNOFF-Algorithm.htm>
116. Smith, A. A. (2022). *Representation of the SWMM/RUNOFF algorithm [Online Image]*. Miduss.com.
<http://www.miduss.com/theory-Calculating-Runoff-SWMM-RUNOFF-Algorithm.htm>
117. Smith, A. A. (2022). *Huff's four storm distributions [Online Image]*. Miduss.com.
<http://www.alanasmith.com/theory-Derivation-Huff-Storm.htm>
118. Smyth, K., Drake, J., Li, Y., Rochman, C., Van Seters, T., & Passeport, E. (2021). Bioretention cells remove microplastics from urban stormwater. *Water Research*, 191, 116785.
119. Straub, T. D., Melching, C. S., & Kocher, K. E. (2000). *Equations for estimating Clark unit-hydrograph parameters for small rural watersheds in Illinois* (No. 4184). US Department of the Interior, US Geological Survey.
120. Sun, N., Hall, M., Hong, B., & Zhang, L. (2014). Impact of SWMM catchment discretization: Case study in Syracuse, New York. *Journal of Hydrologic Engineering*, 19(1), 223-234.
121. Thomé, A. C., Santos, P. G., & Fisch, A. G. (2019). Using rainwater in cooling towers: Design and performance analysis for a petrochemical company. *Journal of Cleaner Production*, 224, 275-283.
122. USGS (U.S Geological Survey). (2019, May 23). *What is Hydrology?* Usgs.gov.
<https://www.usgs.gov/special-topics/water-science-school/science/what-hydrology>
123. Vineyard, D., Ingwersen, W. W., Hawkins, T. R., Xue, X., Demeke, B., & Shuster, W. (2015). Comparing green and grey infrastructure using life cycle cost and environmental impact: A rain garden case study in Cincinnati, OH. *JAWRA Journal of the American Water Resources Association*, 51(5), 1342-1360.
124. Walsh, C. J., Fletcher, T. D., & Ladson, A. R. (2005). Stream restoration in urban catchments through redesigning stormwater systems: Looking to the catchment to save the stream. *Journal of the North American Benthological Society*, 24(3), 690-705.

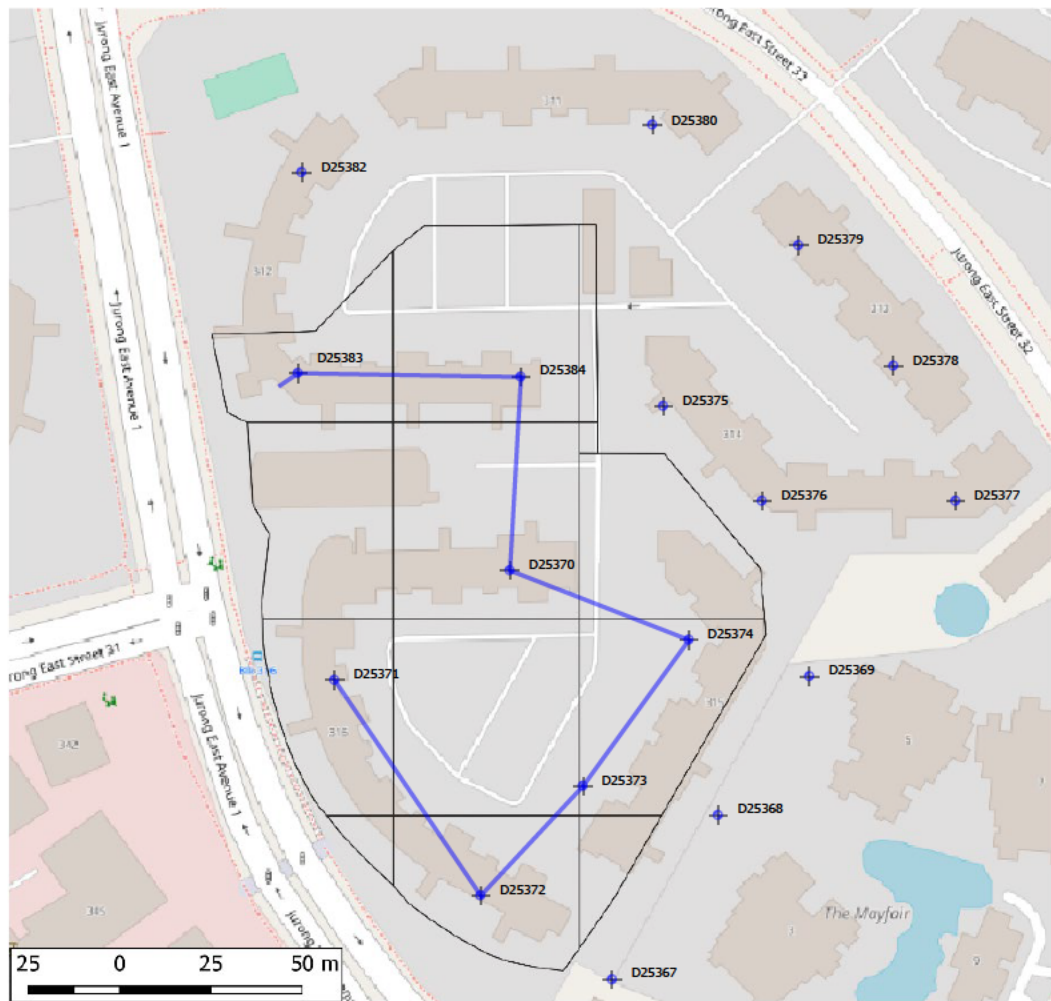
125. Wang, L., & Liu, H. (2006). An efficient method for identifying and filling surface depressions in digital elevation models for hydrologic analysis and modelling. *International Journal of Geographical Information Science*, 20(2), 193-213.
126. Wang, M., Zhang, D. Q., Wang, Y., Su, J., Dong, J. W., & Tan, S. K. (2016). Comparison of Stormwater Management in the Community Park between China and Singapore: A Case Study of Hillside Eco Park and Crescent and Pioneer Hall. In *International Low Impact Development Conference China 2016: LID Applications in Sponge City Projects* (pp. 289-303). Reston, VA: American Society of Civil Engineers.
127. Washburn, B., Yancey, K., & Mendoza, J. (2010). User's guide for the California impervious surface coefficients. *California Environmental Protection Agency*.
128. Weisstein, E. W. (2001). Triangular distribution. Mathworld.wolfram.com
<https://mathworld.wolfram.com/TriangularDistribution.html>
129. Wing Chau, K. (1995). The validity of the triangular distribution assumption in Monte Carlo simulation of construction costs: empirical evidence from Hong Kong. *Construction Management and Economics*, 13(1), 15-21.
130. Wise, S., Braden, J., Ghalayini, D., Grant, J., Kloss, C., MacMullan, E., ... & Yu, C. (2010). Integrating valuation methods to recognize green infrastructure's multiple benefits. In *Low impact development 2010: Redefining water in the city* (pp. 1123-1143).
131. Wong, T. S., & Zhou, M. C. (2002). Re-Evaluation of Manning's Roughness Coefficient for Runoff over Concrete Surface. In *Global Solutions for Urban Drainage* (pp. 1-8).
132. Wu, S., Li, J., & Huang, G. H. (2008). A study on DEM-derived primary topographic attributes for hydrologic applications: Sensitivity to elevation data resolution. *Applied Geography*, 28(3), 210-223.
133. Yen, B. C., & Chow, V. T. (1980). Design hyetographs for small drainage structures. *Journal of the Hydraulics Division*, 106(6), 1055-1076.
134. Zhang, D., Gersberg, R. M., Ng, W. J., & Tan, S. K. (2017). Conventional and decentralized urban stormwater management: A comparison through case studies of Singapore and Berlin, Germany. *Urban Water Journal*, 14(2), 113-124.

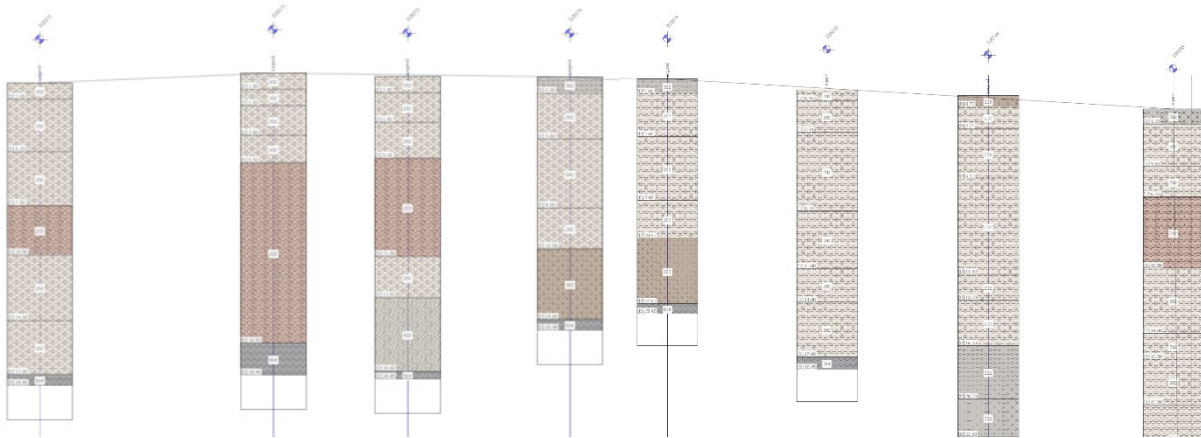
10.0 Appendix

10.1 Elevation Profiles for Hydrologically Conditioned DEMs



10.2 Borehole Data for Site





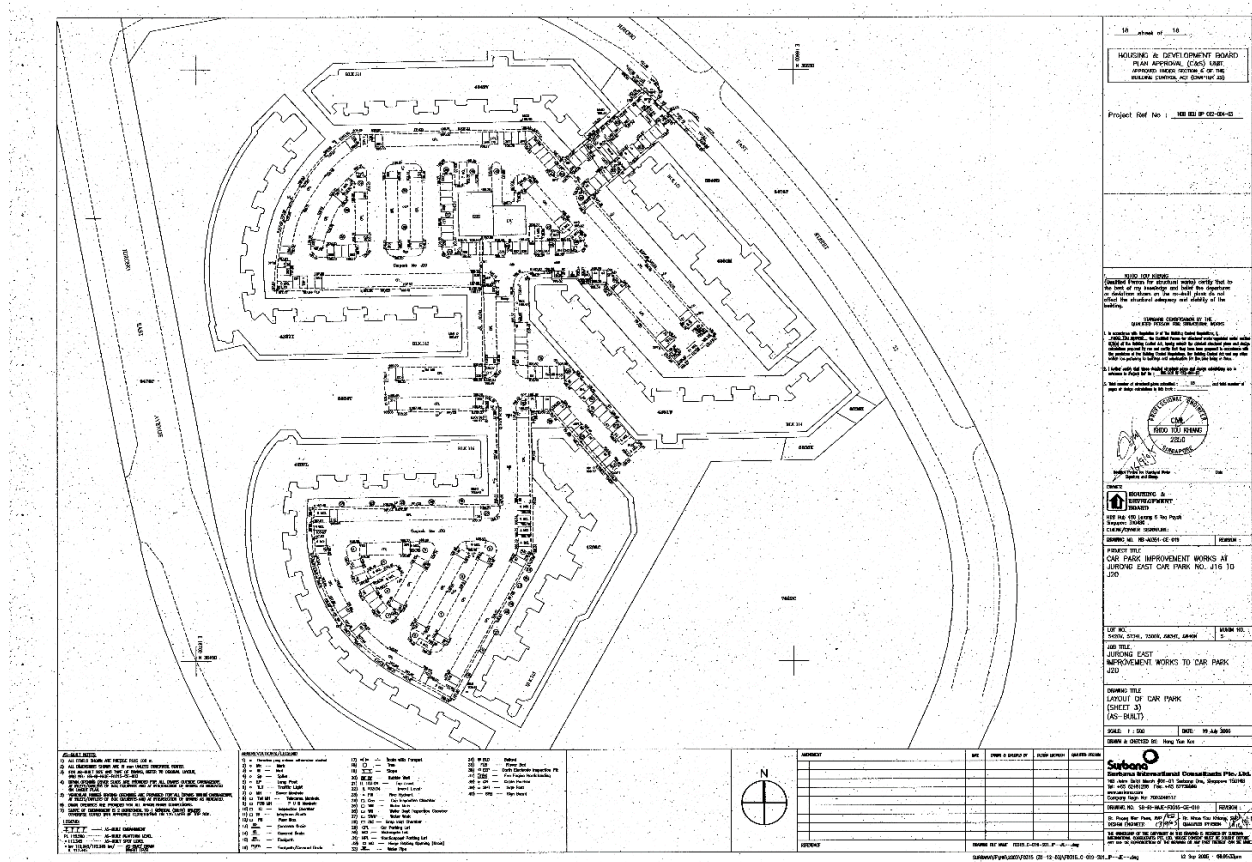
Soil Code	Soil Type
202	Silty Clay
222	Peaty Clay with Organic Material
303	Clayey Sandy Silt
403	Clayey Silty Sand
814	Decomposed Shal

10.3 Subcatchment Parameters

Identifier	Area (ha)	Pervious (ha)	Impervious (ha)	Impervious (%)	Slope(%)	Curve Number
PD1-1	0.02175	0.00314	0.01861	85.55556	3.94412	80
PD1-2	0.11818	0.01271	0.10547	89.24892	3.94412	80
PD2-1	0.13641	0.01785	0.11857	86.91621	6.44128	80
PD2-2	0.01026	0.00000	0.01026	100.00000	7.43814	80
PD2-3	0.12829	0.02557	0.10272	80.06974	6.44128	80
PD3-1	0.00778	0.00061	0.00717	92.18956	6.44128	80
PD3-2	0.01573	0.00029	0.01544	98.16140	7.43814	80
PD4-1	0.17220	0.02592	0.14627	84.94478	5.35176	80
PD4-2	0.00494	0.00000	0.00494	100.00000	6.50837	80
PD5-1	0.07666	0.00732	0.06934	90.44545	6.50837	80
PD6-1	0.10250	0.01417	0.08833	86.17901	5.35176	80
PD6-2	0.05949	0.00577	0.05372	90.30710	0.92977	80
PD6-3	0.00118	0.00000	0.00118	100.00000	0.00000	80
PD6-4	0.00035	0.00000	0.00035	100.00000	3.71907	80
PD6-5	0.03302	0.00252	0.03050	92.36383	1.92290	80
PD7-1	0.08552	0.00909	0.07643	89.37054	6.50837	80
PD8-1	0.13151	0.02434	0.10718	81.49424	0.92977	80
PD8-2	0.16155	0.01771	0.14384	89.03505	3.71907	80
PD8-3	0.02499	0.00036	0.02463	98.54228	1.92290	80
PD9-1	0.16078	0.04345	0.11733	72.97364	4.73922	80

PD9-2	0.01844	0.00532	0.01312	71.15060	2.93747	80
PD10-1	0.01873	0.00449	0.01424	76.01542	4.73922	80
PD10-2	0.04247	0.00780	0.03468	81.64225	5.57860	80
PD11-1	0.20251	0.01517	0.18734	92.50781	0.00000	80
PD11-2	0.08400	0.01752	0.06648	79.13907	0.92977	80
PD12-1	0.02007	0.00000	0.02007	100.00000	6.50837	80
PD13-1	0.14083	0.02892	0.11191	79.46263	1.92290	80

10.4 Drainage Plan for Study Area



10.5 Width Computations for Study Area

Identifier	Width (m)		Manning's Coefficient	
	Method 2	Method 1	Pervious areas	Impervious areas
PD1-1	21.59	7.60	0.012	0.24
PD1-2	21.59	44.2	0.012	0.24
PD2-1	47.76	50.04	0.012	0.24
PD2-2	N.A	4.00	0.012	0.24
PD2-3	74.57	94.47	0.012	0.24
PD3-1	26.5	19.94	0.012	0.24
PD3-2	N.A	13.59	0.012	0.24
PD4-1	84.94	66.54	0.012	0.24
PD4-2	N.A	6.32	0.012	0.24
PD5-1	73.86	51.11	0.012	0.24
PD6-1	74.52	66.40	0.012	0.24
PD6-2	N.A	24.43	0.012	0.24
PD6-3	N.A	1.37	0.012	0.24
PD6-4	N.A	0.58	0.012	0.24
PD6-5	9.72	13.56	0.012	0.24
PD7-1	61.87	28.51	0.012	0.24
PD8-1	38.49	42.42	0.012	0.24
PD8-2	45.74	64.62	0.012	0.24
PD8-3	10.35	10.30	0.012	0.24
PD9-1	48.1	45.04	0.012	0.24
PD9-2	N.A	6.68	0.012	0.24
PD10-1	13.22	11.72	0.012	0.24
PD10-2	N.A	15.43	0.012	0.24
PD11-1	52.01	54.73	0.012	0.24
PD11-2	24.69	31.22	0.012	0.24
PD12-1	53.24	36.17	0.012	0.24
PD13-1	73.72	75.50	0.012	0.24

Notes:

1. Method 1 = Overland flow length method
2. Method 2 = Skew Factor Method
3. Width Parameter was selected based on judgement and how realistic the computed value was in relation to the delineated subcatchment.

10.6 SCS Curve Numbers¹

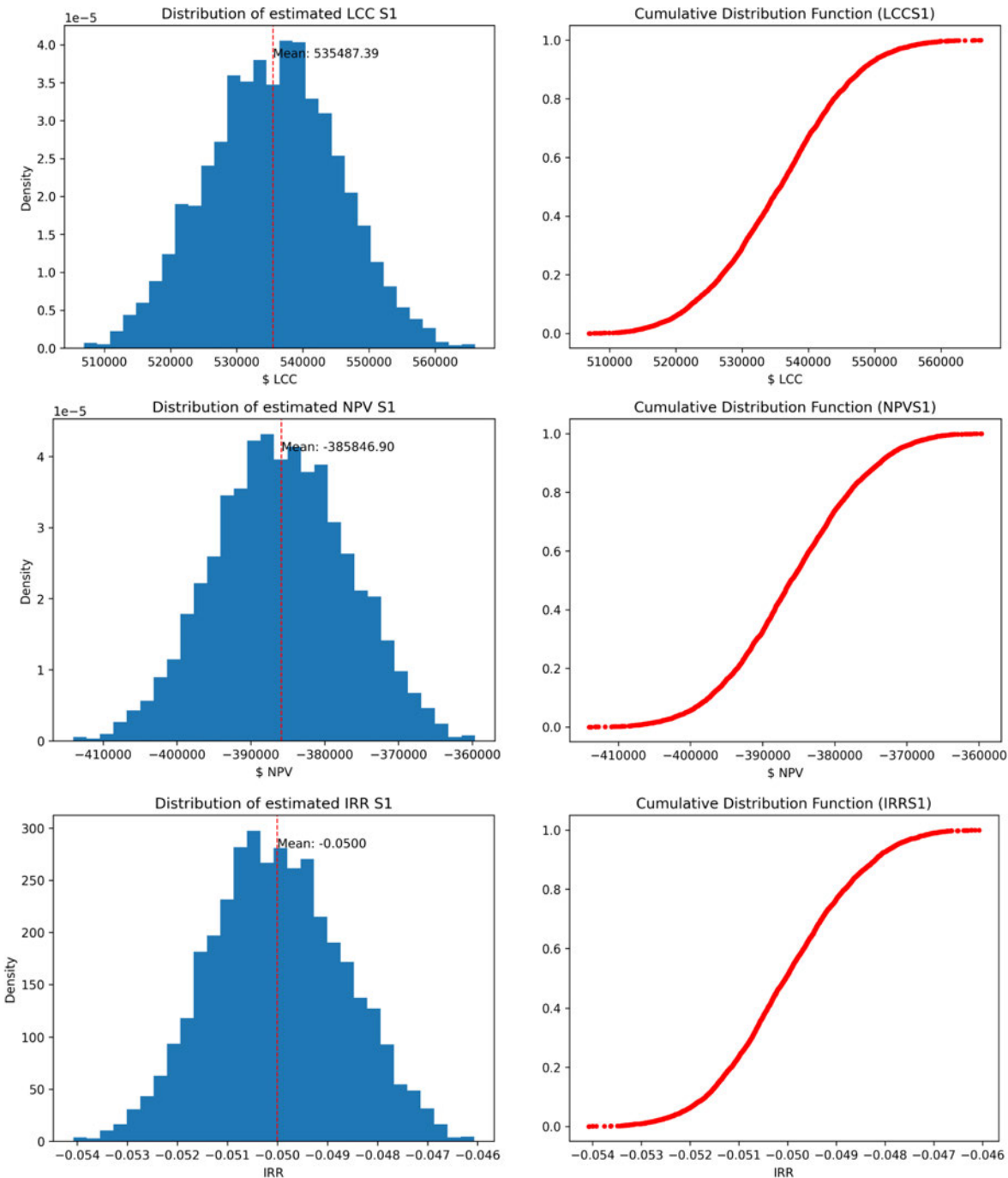
Land Use Description	Hydrologic Soil Group			
	A	B	C	D
Cultivated Land				
Without conservation treatment	72	81	88	91
With conservation treatment	62	71	78	81
Pasture or Rangeland				
Poor Condition	68	79	86	89
Good Condition	39	61	74	80
Meadow				
Good Condition	30	58	71	78
Wood or forest land				
Thin stand, poor cover, no mulch	45	66	77	83
Good Cover ²	25	55	70	77
Open spaces, lawns, parks, golf courses, cemeteries,etc.				
Good condition: grass cover on 75% or more of the area	39	61	74	80
Fair condition: grass cover on 50-75% of the area	49	69	79	84
Commercial and business areas (85% impervious)	89	92	94	95
Industrial districts (72% impervious)	81	88	91	93

Notes:

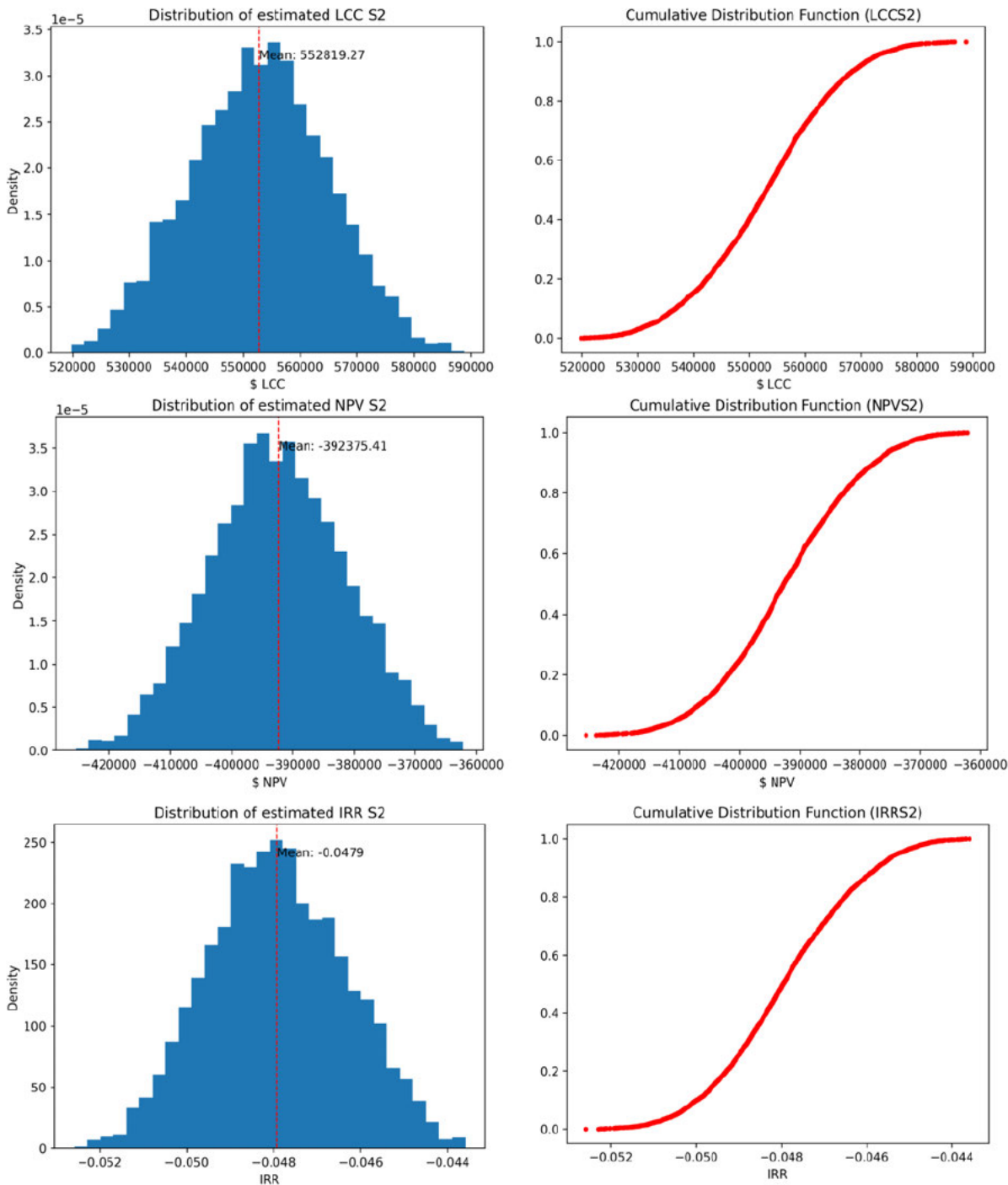
1. Antecedent moisture condition II
2. Good cover is protected from grazing, litter, and brush cover soil.

10.7 Probability Distribution of LCC, NPV, IRR

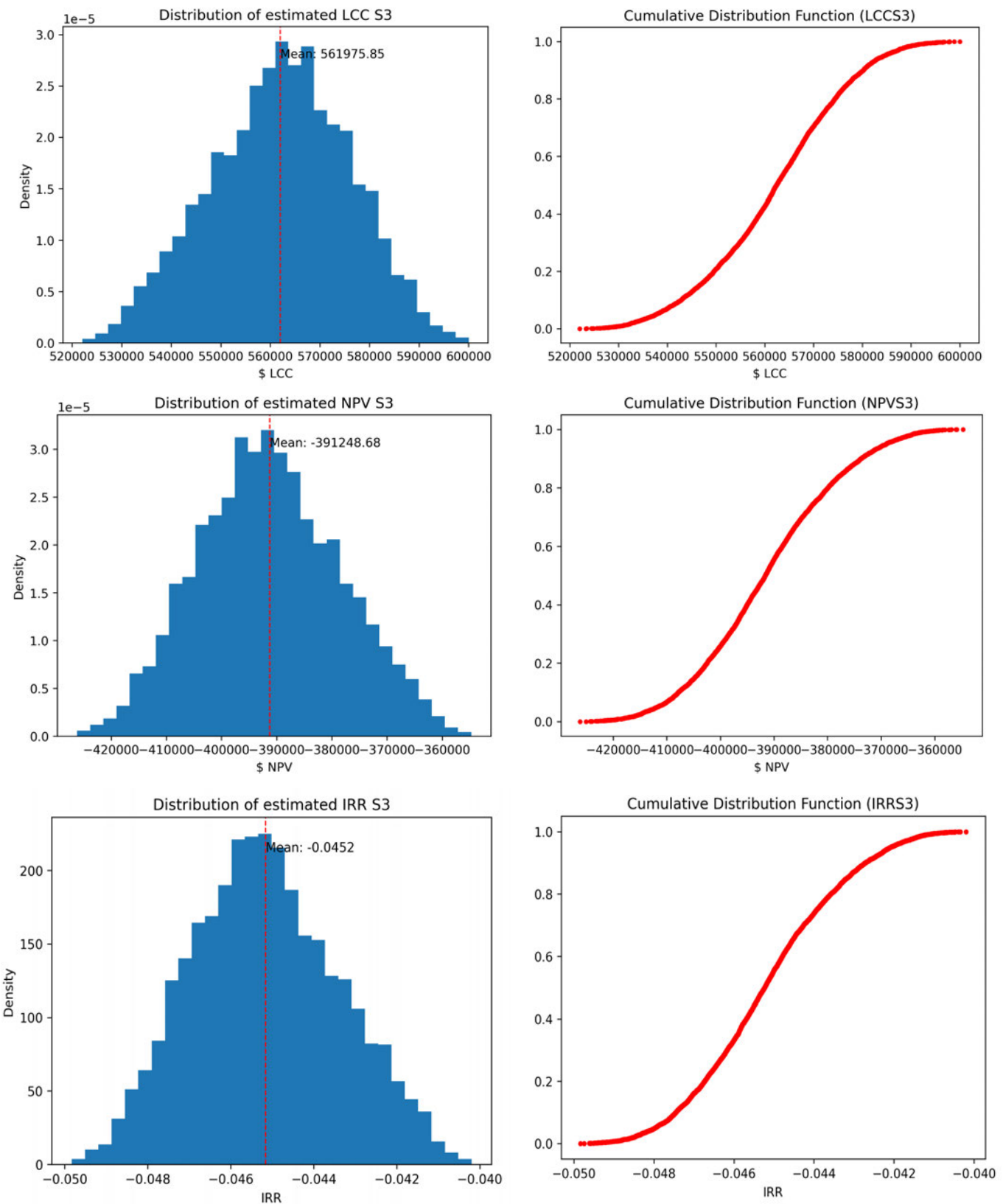
UWHS Configuration: S1



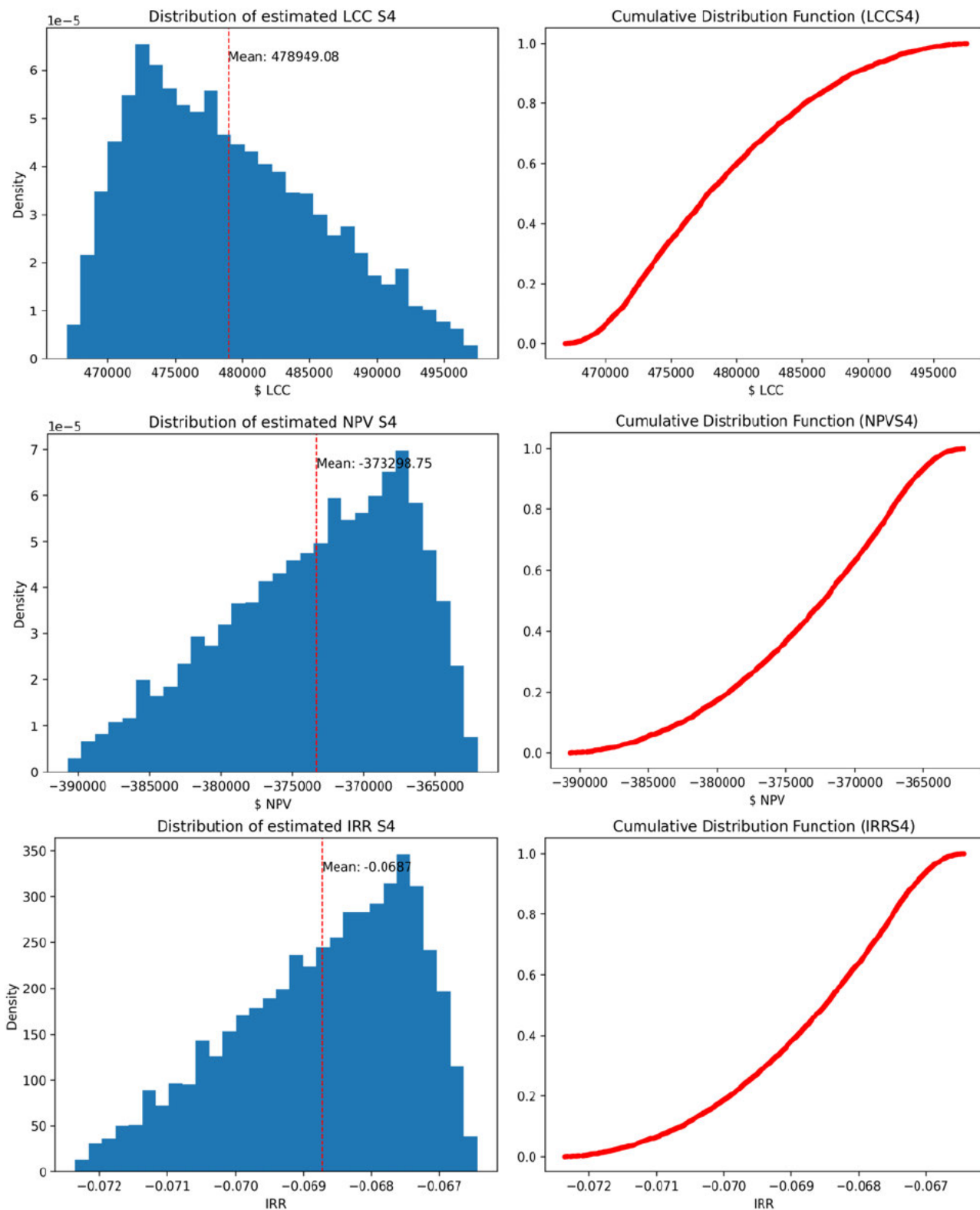
UWHS Configuration: S2



UWHS Configuration: S3

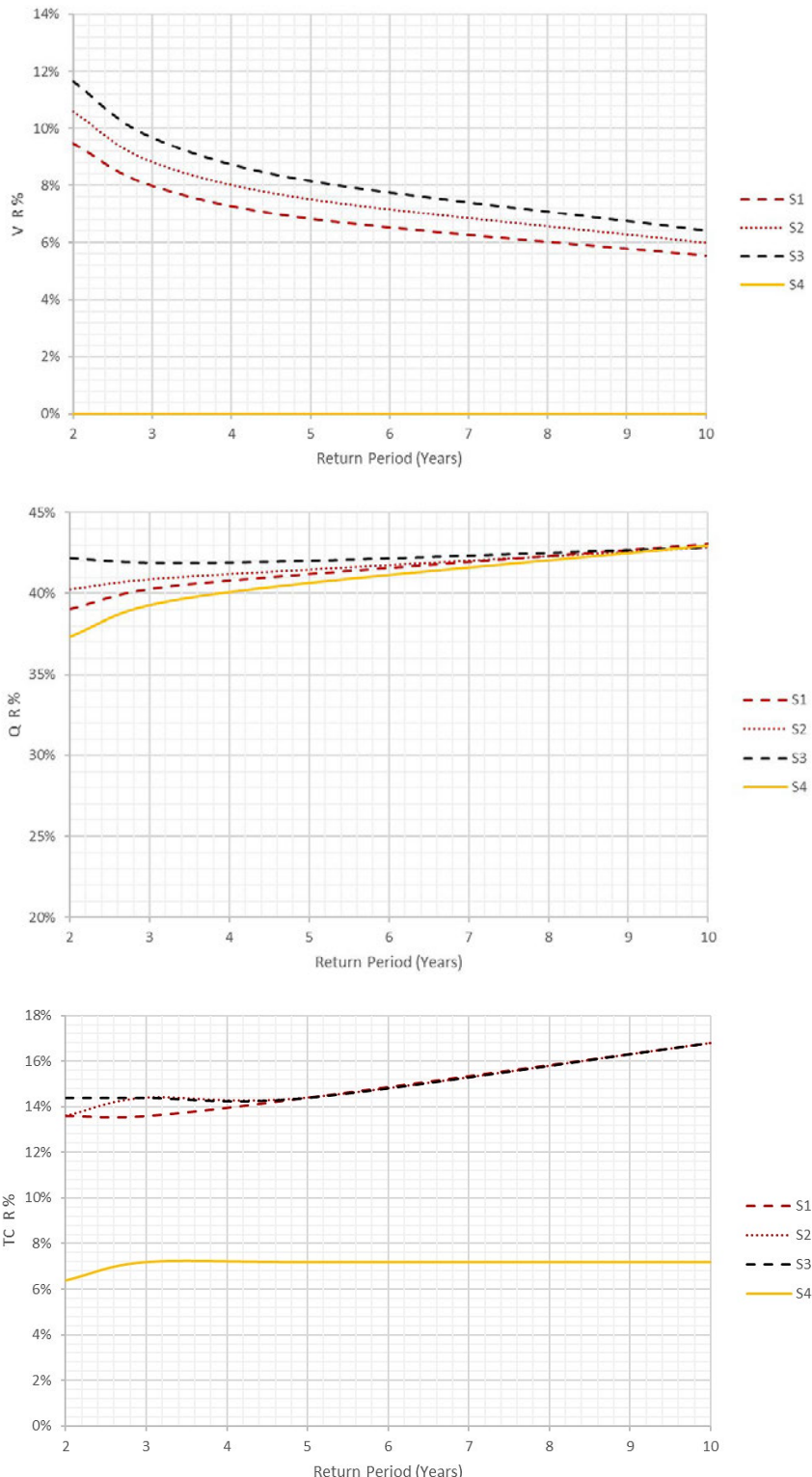


UWHS Configuration: S4



10.8 Hydrological and Treatment Performance of UWHS Configurations (2, 3, 5, 10 yr ARI storm events)

Hydrological Performance Trends



Treatment Performance Trends

